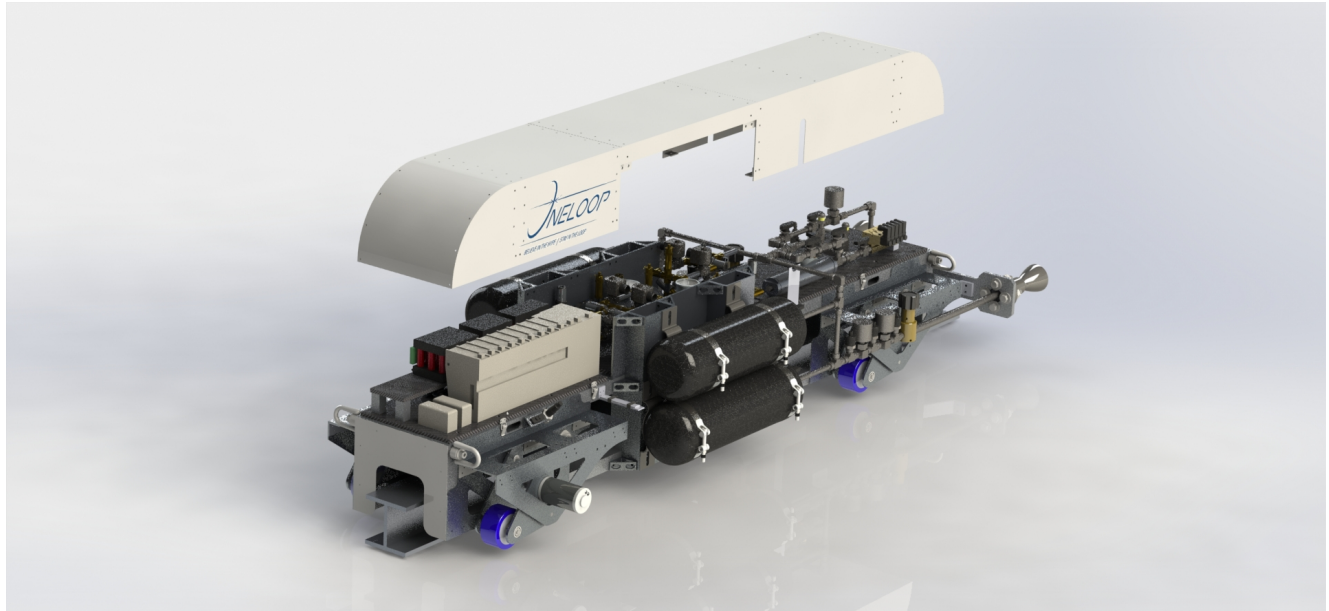


Final Design Report: OneLoop 2019

The Hyperloop Pod Team at UC Davis

January 26, 2019



Acknowledgements

OneLoop's work would not have been possible without guidance and support from our advisors and sponsors. These individuals and companies have continually shown their belief in our team and their desire to see us rise to the top of the competition. With that being said, we are extremely grateful to...

Professor C.P "Case" van Dam

Professor Thomas Gordon

Professor Stephen K. Robinson

Professor Valeria La Saponara

Professor Francis Assadian

Professor Bahram Ravani

Professor Michael Meyers and the Meyers Research Group

Dr. Zachary Sabato

Michael Gaunt of Hyperloop One

Bruno Matsui of SpinLaunch

Kevin Pedersen of NASA MSFC

Christopher Burnside of NASA MSFC

Rad Sommer of II-VI Photonics

Daret Kehlet

Rockwell Technologies

Rexel

Aqua Environment

The CITRIS and Banatao Institute of Tech for Social Good

Keysight Technologies

TC Metals

Ubiquiti Networks

Bourns

ANSYS

WC Branham

UC Davis ESDC

National Technical Systems

Lastly, OneLoop is happy to call the Chevron Lab at UC Davis our home, and the UC Davis Engineering Student Design Center (ESDC) our workspace. We would especially like to thank Mike Akahori, Shawn Malone, Sherry Batin, and David Kehlet of the ESDC for continually assisting the team with manufacturing related advice along with instilling a safety cognizant mindset in us.

Contents

1 Team Description	1
2 Pod Overview	2
2.1 Top Level Design Summary	2
2.2 Payload Capability	2
2.3 Pod Materials and Components	2
2.4 Pod Velocity Profile	12
2.5 Cost Breakdown and Funding	13
2.5.1 Current Funds	13
2.5.2 Plans for Future Funding	14
2.6 Production Schedule and Pod Readiness	15
2.6.1 Pod Readiness	15
3 Subsystem Design	16
3.1 Power System	16
3.1.1 Technical Description	16
3.1.2 Design Rationale	16
3.1.3 Design	16
3.1.4 Fuses	18
3.2 Chassis/Mounting	19
3.2.1 Technical Description	19
3.2.2 Design Rationale	19
3.2.3 Design	21
3.2.4 Structural Analysis	23
3.3 Aerodynamic Shell	29
3.3.1 Technical Description	29
3.3.2 Design Rationale	29
3.3.3 Design	30
3.3.4 Analysis	30
3.4 Lateral Stability System	31
3.4.1 Technical Description	31
3.4.2 Design Rationale	32
3.4.3 Safety	32
3.4.4 Analysis	33
3.5 Suspension System	34
3.5.1 Technical Description	34
3.5.2 Design Rationale	36
3.5.3 Design	36
3.5.4 Analysis	37
3.6 Propulsion System	39
3.6.1 Technical Description	39
3.6.2 Design Rationale	43
3.6.3 Design	44
3.7 Catalyst Bed	57
3.7.1 Technical Description	57
3.7.2 Design Rationale	57
3.7.3 Analysis	58
3.8 Braking System	58
3.8.1 Technical Description	58
3.8.2 Design Rationale	60
3.8.3 Analysis	60
3.9 Controls System	63
3.9.1 Overview	63

3.9.2	Technical Description	64
3.9.3	Controller Program Loop	64
3.9.4	State Diagram	65
3.9.5	Pod Navigation	68
3.9.6	State Transitions	68
3.9.7	Implementation of Pod-Stop Command	70
3.9.8	Pod Subroutines	71
3.9.9	Electronic System Overview	71
3.9.10	Sensor States	76
3.9.11	GUI	77
4	Pod Thermal Profile	77
4.1	Introduction	77
4.2	Heat Transfer Due to Propulsion Systems	78
4.2.1	Model & Analysis	78
4.2.2	Results	78
4.2.3	Discussion	79
4.3	Heat Transfer Due to Wheel Friction	79
4.3.1	Model and Analysis	79
4.3.2	Results	80
4.3.3	Discussion	80
4.4	Conclusions	81
5	Predicted Vibration Environment	81
6	Safety	81
6.1	Subsystem Safety	81
6.1.1	Power Safety	81
6.1.2	Propulsion Safety	82
6.1.3	Braking Safety	86
6.2	Additional Safety Features	86
6.2.1	Inhibits on Braking During Acceleration	86
6.2.2	Mechanisms to Mitigate Complete Loss of Power	86
6.2.3	Single Points of Failure and Pod Failure Analysis	87
6.2.4	Recovery Plan if Pod Becomes Immovable within Tube	88
6.3	Stored Energy	88
6.4	Hazardous Materials	89
6.5	Vacuum Compatibility Analysis	92
7	Testing	93
7.1	Subsystem Testing	93
7.1.1	Power Testing	93
7.1.2	Structures Testing	93
7.1.3	Stability Testing	98
7.1.4	Suspension Testing	98
7.1.5	Propulsion Testing	101
7.1.6	Braking Testing	108
7.1.7	Controls Testing	109
7.2	Full Pod Testing	110
8	Loading and Unloading Plan	111

9 Comments on Scalability	115
9.1 Least Scalable	115
9.1.1 Suspension and Stability	115
9.1.2 Chassis	115
9.1.3 Power	116
9.2 Somewhat Scalable	116
9.2.1 Propulsion	116
9.2.2 Braking	116
9.3 Most Scalable	117
9.3.1 Controls	117
9.4 Conclusion	117

1 Team Description



Figure 1: OneLoop Hyperloop Pod Team

The 2019 OneLoop Team is comprised of 62 UC Davis students across both engineering and non-engineering disciplines. 61 of our members are undergraduate students, along with one graduate student. OneLoop has one mission:

- Become the fastest US-based pod to race in the competition, having passed safety inspections and obtained permission to race.

Leadership

Faculty Advisor:	Chief Engineer:	Business:	Simulations:	Treasurer:
C.P "Case" Van Dam	Austin Gonzalez	Samarth Sandeep	Miranda Bell	Zack Chua
Propulsion:	Structures:	Suspension:	Braking:	Controls:
Daniel Nasr-Church	Simon Chang	Jeremy Ondarts	Jonathan Summer	Kareem K Mohammed
William Mazotti	Tomoya Otsuka	Kevin Li	Sam Menigoz	Naveed Oroumchian

Members

Aaron Leo	Christophe Hiltebrandt	Kenley Hendrawan	Patricia Paje
Aaron Bass	Dara Sobati	Lauren Seto	Pranit Narayanaswamy
Aidan Fox-Terney	Delahny Deivendran	Madhusha Goonesekera	Rajdeep Singh
Alice Liu	Eric Guo	Max Fors	Riley Schreiner
Amin Haghghi	Erica Lee	Megan Lo	Sach Samala
Avarinth Raghaven	Frankle Chrisyanto	Michael Cox	Soumil Shekdar
Brandon Dela Cruz	Gabriel Ketron	Michael Li	Sri Kumar
Brandon Lau	Isabelle Asistin	Michael Sanders	Talal Sohail
Bruce Meng	Jack Zhou	Michael Xiao	Timothy Hulse
Cameron Shinn	Jackson Liao	Minkook Park	Torin Keenan
Carl Hutchison	Jason Ciola	Mynor Andres Juan	Wenqing Wang
Chaitanya Gupta	John Long	Parin Rau	Yash Dani

2 Pod Overview

2.1 Top Level Design Summary

This year, OneLoop presents a robust pod capable of reaching 100 mph that was designed with safety as a top priority. OSHA, ASME, and other safety standards are adhered to with regards to pod design, testing, and operation whenever relevant. Furthermore, this year's propulsion system is a modified cold gas thruster concept, which was chosen primarily to reduce the pod's high voltage requirements and increase electrical safety. Also, our business team improved pod safety by securing a sponsorship with Rockwell Automation, which resulted in the donation of a SIL-2 Safety Controller with a mean time between failure (MTBF) of over 100,000 hours. Rockwell has even offered to assist our team in the implementation of our control algorithm to ensure that we take advantage of the controller's safety features. Lastly, safety is emphasized in our pod testing plan, which includes professional thermo-vacuum environment testing conducted by NTS to achieve vacuum-safe certification prior to attending the competition.

The 2019 pod is comprised of six subsystems, which are briefly detailed below. The pod weighs 350 lbs at the start of the run, which decreases to 332 lbs by the time it reaches the end of the tube due to propellant depletion.

Subsystems Overview

- *Power:* Two 24V power packs (one primary and one backup) and one 12V secondary pack for operating the pod wheels. All three packs are comprised of cylindrical Li-ion cells.
- *Structures:* An inverted, U-shaped chassis for mounting modularity, Kevlar-honeycomb composite mounting platforms, an aerodynamic shell to reduce any potential drag, and all pod mounting surfaces.
- *Suspension and Stability:* Four single pivot linkage suspension systems and two lateral stability systems to facilitate a smooth run.
- *Propulsion:* Two catalytic tri-gas thrusters that expel pressure-regulated and chemically-heated Nitrogen gas, resulting in 60 lbf (267 N) thrust per nozzle.
- *Braking:* Two independent pneumatically-actuated caliper friction brake systems.
- *Controls:* A Safety Controller PLC that oversees the Propulsion and Braking systems as well as system telemetry.

After accounting for sponsorships, the total pod cost is \$18,696, of which \$17,128 has already been secured.

2.2 Payload Capability

The payload capacity of the pod is 1100lbs. This capacity assumes that the pod is stationary, with only weight loads applied on it. Weight capacity is limited by the structural integrity of the four suspension systems, each designed to carry 375lbs under both bump and weight loads as analyzed in Section 3.5.3. Note that the chassis itself can hold 3507lbs of weight before failure as shown in Section 3.2.4, so the chassis structure does not limit the payload capacity.

2.3 Pod Materials and Components

On all Bills of Materials, the line "Seller Multiplier" expresses the percent the supplier is charging. If a seller multiplier is .25, then the product is being sold at 25%, resulting in a 75% discount. Products with a star * in the description have already been acquired, and their cost initial cost is not counted toward overall cost.

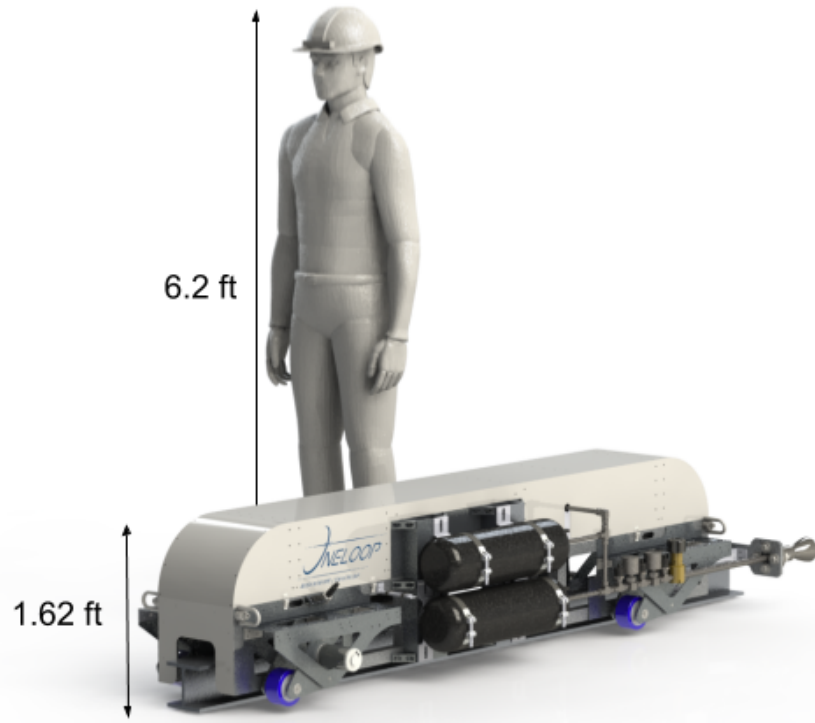


Figure 2: Pod with Human for Scale

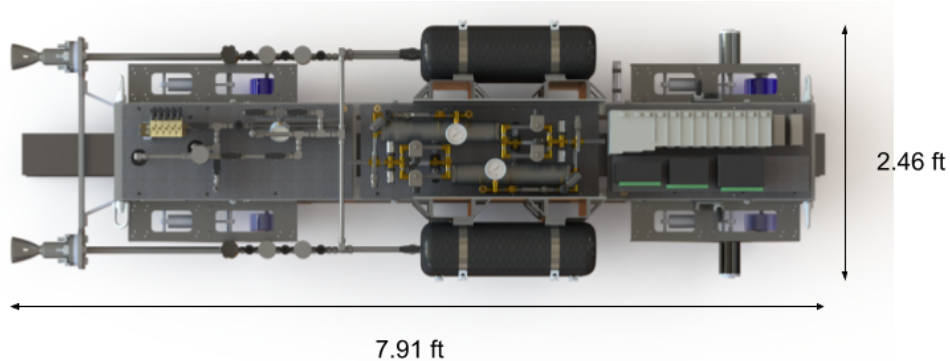


Figure 3: Pod Dimension: Length and Width

Table 1: Power Bill of Materials

Product ID	Description	Qty	List Price/unit	Seller Multiplier	Total Cost	Provider
LG HE2 Cell	Battery	100	\$3.50	1	\$350.00	LG
PCM-L07 S15CM	Main BMS	1	\$118.00	1	\$118.00	Battery Space
PCM-L04S60-COM485	Secondary BMS	1	\$122.00	1	\$122.00	Battery Space
BMS 2430	Passive BMS	1	\$31.99	1	\$31.99	Vruzend
VRUZEND K30	Wire clamps, cable tie straps	1	\$33.99	1	\$33.99	Vruzend

Table 1: Power Bill of Materials

Product ID	Description	Qty	List Price/ unit	Seller Multiplier	Total Cost	Provider
charger4s	4s Lithium-ion Battery Charger	1	\$19.99	1	\$19.99	Vruzend
charger243	24V Lithium-ion Battery Charger	1	\$27.99	1	\$27.99	Vruzend
3-02-1201-G	Angel Eye LED Light Metal Toggle Switch	3	\$6.99	1	\$20.97	Amazon
CXR120	EMR Relay	1	\$10.39	1	\$10.39	Amazon
Total Cost:						\$735.32

Table 2: Chassis Bill of Materials

Product ID	Description	Qty	List Price/ unit	Seller Multiplier	Total Cost	Provider
	Square Tubing (1.5" x1.5" x1/8")	2	\$400.00	1	\$800.00	Welder
89015 K28	Aluminum Angle Beams (12" x24" x1/8")	2	\$47.11	1	\$94.22	McMaster-Carr
97525 A425	Rivet (1/4"-20) for (0.1880"-0.25")	8	\$8.53/250pack	1	\$8.53	McMaster-Carr
C3527 5190	C Channel (5" x2.75" x 190" web), 1'4"	4	\$59.28	1	\$237.12	MetalsDepot
47065 T736	Silver Gusset Bracket 2"	24	\$9.99	1	\$239.76	McMaster-Carr
95105 a143	Rivet Nut (1/4"-20) for (027"-.165")	96	\$9.08/25pack	1	\$36.32	McMaster-Carr
91251 A541	Socket Head Screw (1/4"-20x7/8")	96	\$8.41/50pack	1	\$16.82	McMaster-Carr
HRVMS 2 R 159-167 / 165 ST	Tank Clamps	8	\$25.00	1	\$200.00	Hydac
95105 A191	Rivet Nut (M10-1.5) for (0.7-3.8 mm)	16	\$5.04/10pack	1	\$10.08	McMaster-Carr
	Lockable Hex Bolt (M10-1.5x16mm)	24	\$7.33/10pack	1	\$14.66	drilledheadbolts.com
93475 A280	M10 Steel Washers	16	\$6.10/50pack	1	\$6.10	McMaster-Carr
2994 T63	Forged Steel Hoisting Hook	4	\$55.19	1	\$220.76	McMaster-Carr
95105 A159	Rivet Nut (3/8"-16) for (0.27"-0.15")	4	\$6.61/10pack	1	\$6.61	McMaster-Carr
60689	Ratcheting Tie Down (3300 lbs)	4	\$14.99	1	\$59.96	Harbor Freight
8AUJ9	Adj. Spreader (500lb) (48" Max, 12" Min, 7" Headro.)	1	\$410.88	1	\$410.88	Grainger

Table 2: Chassis Bill of Materials

Product ID	Description	Qty	List Price/ unit	Seller Multiplier	Total Cost	Provider
1250	Nozzle Mount (28"x4.5"x 0.5" Aluminum Plate)	1	\$68.04	1	\$68.04	onlinemetals.com
97525 A435	Rivet (1/8") for (0.3130"-0.375")	8	\$10.83/100pack	1	\$10.83	McMaster-Carr
91255 A544	Button Head Hex Screw (1/4"-20, 1-1/4")	4	\$16.22/25pack	1	\$16.22	McMaster-Carr
97135 A210	Locknut (1/4")	4	\$3.56/25pack	1	\$3.56	McMaster-Carr
1248	Nozzle Mount Strut (7.1"x1.5"x0.25" Aluminum Plate)	2	\$2.56	1	\$5.12	onlinemetals.com
8975 K578	Aluminum Stock (1/8"x1"x6")	2	\$0.95	1	\$1.90	McMaster-Carr
156177	Stainless Rivet (1/8") Dia. Grip Range (.188"-.250")	4	\$0.19	1	\$0.76	Fastenal
91169	Steel Machine Screw (M2-0.4x6mm) DIN 7985	4	\$0.10	1	\$0.40	Fastenal
93625 A101	Steel Nylon Inserts Hex locknuts (M2x0.4mm)	4	\$7.32/10pack	1	\$7.32	McMaster-Carr
8975 K215	Aluminum Stock (1/2"x4"x12")	2	\$20.84	1	\$41.68	McMaster-Carr
97525 a442	Rivet (1/8") for (0.5010"-0.625")	16	\$10.16/50pack	1	\$10.16	McMaster-Carr
	Composite Panels	3	\$0.00	0	\$0.00	ESDC
91255 A247	Stainless Hex Drive Screw (10-24, 1")	24	\$9.12/50pack	1	\$9.12	McMaster-Carr
95105 A127	Rivet Nut (10-24) for (.02"x.13")	24	\$6.49/25pack	1	\$6.49	McMaster-Carr
9D0316 -3P	Press-Fit Threaded Insert for Composites	24	\$3.00	1	\$72.00	Marketing Masters
Total Cost:						\$2615.42

Table 3: Aeroshell Bill of Materials

Product ID	Description	Qty	List Price/ unit	Seller Multiplier	Total Cost	Provider
1239	6061 Aluminum Sheet (36"x12"x0.032")	3	\$13.11	1	\$39.33	onlinemetals.com
1239	6061 Aluminum Sheet (12"x12"x0.032")	6	\$5.28	1	\$31.68	onlinemetals.com
1239	6061 Aluminum Sheet (24"x24"x0.032")	1	\$16.38	1	\$16.38	onlinemetals.com

Table 3: Aeroshell Bill of Materials

Product ID	Description	Qty	List Price/ unit	Seller Multiplier	Total Cost	Provider
1239	6061 Aluminum Sheet (12"x24"x0.032")	3	\$10.20	1	\$30.60	onlinemetals.com
1242	6061 Aluminum Sheet (36"x12"x0.065")	1	\$21.17	1	\$21.17	onlinemetals.com
1246	6061 Aluminum Sheet (24"x12"x0.125")	1	\$36.29	1	\$36.29	onlinemetals.com
2313N36	6061 Aluminum Bracket (1"x1/8"x1-1/4")	8	\$6.83	1	\$54.64	McMaster-Carr
8511A23	Support Button (3/8" OD, 1/2" L)	8	\$2.07	1	\$16.56	McMaster-Carr
126180	Rivet (3/16" OD, .062"-.125" Grip Range)	168	\$0.12	1	\$20.16	Fastenal
6082A12	304 Stainless Steel Latch (1-3/4"x7/8")	8	\$6.77	1	\$54.16	McMaster-Carr
Total Cost:						\$320.97

Table 4: Linear Stability Bill of Materials

Product ID	Description	Qty	List Price/ unit	Seller Multiplier	Total Cost	Provider
FR8ZZ	Flanged Bearing*	20	\$3.00	0	\$0.00	AndyMark
97633A200	External Retaining Ring*	20	\$10.13/100pack	0	\$0.00	McMaster-Carr
91251A345	10-32 Socket Head Screw*	40	\$10.69/100pack	0	\$0.00	McMaster-Carr
2292T32	Cut-to-Width Polyurethane Wheel*	1	\$121.80	0	\$0.00	McMaster-Carr
8716k58	Abrasion-Resistant Polyurethane Rubber* Sheet	4	\$31.21	0	\$0.00	McMaster-Carr
1346K19	Rotary Shaft*	8	\$3.30	0	\$0.00	McMaster-Carr
7003	Aluminum Bare Tube*	2	\$5.10	0	\$0.00	www.onlinemetals.com
7936K32	Steel Rod*	2	\$7.07	0	\$0.00	McMaster-Carr
95462A031	Hex-Nut*	16	\$11.22/50pack	0	\$0.00	McMaster-Carr
	Side Plate*	2	\$0.00	0	\$0.00	McMaster-Carr
	Top Plate*	2	\$0.00	0	\$0.00	McMaster-Carr
	Rib*	2	\$0.00	0	\$0.00	McMaster-Carr
9246K475	T6 6061 Aluminum (12"x24"x3/8")*	2	\$145.06	0	\$0.00	McMaster-Carr
Total Cost:						\$0.00

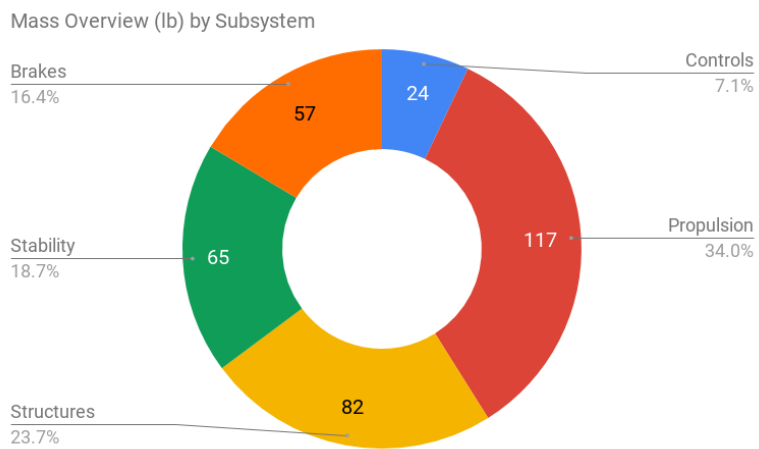


Figure 4: Mass Overview by Subsystem

Table 5: Suspension Bill of Materials

Product ID	Description	Qty	List Price/unit	Seller Multiplier	Total Cost	Provider
60355 K45	Sealed Ball -Bearing (3/8" ID)	16	\$6.88	1	\$110.08	McMaster-Carr
60355 K505	Sealed Ball -Bearings (1/2" ID)	8	\$6.27	1	\$50.16	McMaster-Carr
9246 K11	Aluminum Sheet (1/4"x8"x8")*	8	\$0.00	0	\$0.00	ESDC
89015 K48	Aluminum Sheet (1/8"x24"x24")*	4	\$0.00	0	\$0.00	ESDC
8974 K13	Aluminum Rod (1" OD, 1/2' Long)	4	\$4.59	1	\$18.36	Mcmaster-Carr
1886 K12	1045 Carbon Steel Rod (3/8" OD, 57" Long)	1	\$32.49	1	\$32.49	Speedy Metals
1886 K23	1045 Carbon Steel Rod (1/2" OD, 25" Long)	1	\$11.00	1	\$11.00	Speedy Metals
2737 T174	Roller Chain Sprocket (24 Teeth, 3/4" ID, ANSI 25)	2	\$15.15	1	\$30.30	McMaster-Carr
2737 T102	Roller Chain Sprocket (12 Teeth, 3/8" ID, ANSI 25)	2	\$10.81	1	\$21.62	McMaster-Carr
6261 K171	Roller Chain (2', ANSI 25)	2	\$10.28	1	\$20.56	McMaster-Carr
6261 K108	Roller Chain Connecting Link (ANSI 25)	2	\$1.00	1	\$2.00	McMaster-Carr
	Polyurethane Wheel (Shore 95A, 4" OD, 2" Wide)*	4	\$45.00	0	\$0.00	Sunray-inc

Table 5: Suspension Bill of Materials

Product ID	Description	Qty	List Price/ unit	Seller Multiplier	Total Cost	Provider
PM25R-45F-1003	2.5 in CIM Motor*	2	\$20.00	0	\$0.00	AndyMark
2489 K24	One-Way Locking Needle-Roller Bearing Clutch (1/2" ID)	2	\$11.17	1	\$22.34	McMaster-Carr
1434 K25	Mounted Roller Bearing with Two-Bolt Flange	8	\$18.62	1	\$148.96	McMaster-Carr
642872 717183	DNM DV22AR Mountain Bike Rear Shock	4	\$45.00	1	\$180.00	Rakuten
91251 A460	Steel Socket Head Screw (12-24, 3/4")	16	\$6.30/10pack	1	\$12.60	McMaster-Carr
91251 A150	Steel Socket Head Screw (6-32, 5/8")	128	\$8.88/100pack	1	\$17.76	McMaster-Carr
91251 A148	Socket Head Screw (6-32, 1/2")	64	\$8.66/100pack	1	\$8.66	McMaster-Carr
91251 A539	Steel Socket Head Screw (1/4"-20, 5/8")	8	\$7.74/50pack	1	\$7.74	McMaster-Carr
91831 A025	18-8 Stainless Steel Nylon-Insert Locknut (12-24)	16	\$7.19/50pack	1	\$7.19	McMaster-Carr
91831 A007	18-8 Stainless Steel Nylon-Insert Locknuts (6-32)	192	\$4.43/100pack	1	\$8.86	McMaster-Carr
96765 A115	18-8 Stainless Steel Washer (No. 6)	192	\$3.88/100pack	1	\$7.76	McMaster-Carr
97633 A170	External Retaining Ring (3/8")	48	\$9.09/100pack	1	\$9.09	McMaster-Carr
97633 A200	External Retaining Ring (1/2")	24	\$10.54/100pack	1	\$10.54	McMaster-Carr
9017 K444	Low-Carbon Steel 90 Degree Angle (1"x1"x1/8") (6')	1	\$14.80	1	\$14.80	McMaster-Carr
Total Cost:						\$752.87

Table 6: Propulsion Bill of Materials

Product ID	Description	Qty	List Price/ unit	Seller Multiplier	Total Cost	Provider
873-1500 -H-L	Non-Relieving Pressure Regulator	2	\$750.00	0	\$0.00	Aqua Enviornment
AVS-3111 -120A	Normally Closed Solenoid Valve	5	\$20.50	1	\$102.50	AutomationDirect.com
4FLV2	Pressure Gauge	1	\$12.00	1	\$12.00	Grainger
4F-B6L J2-SSP	High Pressure Manual Valve	7	\$101.00	1	\$707.00	Parker Valves
796	Flow Restrictor	1	\$42.00	0	\$0.00	Aqua Enviornment

Table 6: Propulsion Bill of Materials

Product ID	Description	Qty	List Price/unit	Seller Multiplier	Total Cost	Provider
IORMAN 4500PSI	Composite Air Cylinder	4	\$400.00	1	\$1600.00	IORMAN
AM-316	Solenoid Valve Manifold	1	\$26.00	1	\$26.00	AutomationDirect.com
30-11HF4	Air Operated Valve	5	\$254.00	1	\$1270.00	High Pressure Products
D-11846-A-11	Air Reservoir	1	\$97.00	1	\$97.00	Bimba
SS-4R3A5	High Pressure Relief Valve	1	\$232.00	1	\$232.00	Swagelok
SS-RL3 M4-F4	Low Relief Valve	1	\$280.00	1	\$280.00	Swagelok
458	304 SS Pipe (0.25" OD, .049" WT, 8')	1	\$33.00	1	\$33.00	OnlineMetals.com
467	7' of 0.50" 304 SS Pipe 0.49" WT	1	\$19.00	1	\$19.00	OnlineMetals.com
VV500P-4	Low Pressure Manual Valve	1	\$26.00	1	\$26.00	Parker Valves
304 SS Stock	4" Bar Stock 16" Long 304 SS	1	\$400.00	1	\$400.00	DiscountSteel.com
MF Catalyst	Pelletized catalyst 1kg	1	\$695.00	1	\$695.00	BASF
SS-5605-04-04-04	0.25" Tee	15	\$25.00	1	\$375.00	Titan Fittings
SS-5652-04-04-04	0.25" Cross	1	\$44.00	1	\$44.00	Titan Fittings
SS-5504-04-04	0.25" Elbow	6	\$19.00	1	\$114.00	Titan Fittings
Tri-Gas (Est.)	Propellant AirGas	1	\$1000.00	1	\$1000.00	
SS-5404-04-04	0.25" Male Nipple	21	\$6.00	1	\$126.00	Titan Fittings
Total Cost:						\$7158.50

Table 7: Braking Bill of Materials

Product ID	Description	Qty	List Price/unit	Seller Multiplier	Total Cost	Provider
D-1022-A-0.125	Air Reservoir*	2	\$70.00	0	\$0.00	Bimba
6GD06	Ball Valve	6	\$11.00	1	\$66.00	Grainger
30E608	Fill Valve	2	\$10.00	1	\$20.00	Grainger
ST25-200	Relief Valve	2	\$7.39	1	\$14.78	Amazon
ST25-125	Relief Valve	2	\$7.39	1	\$14.78	Amazon
18755 HD	Pressure Gauge	2	\$4.95	1	\$9.90	Marlin P Jones

Table 7: Braking Bill of Materials

Product ID	Description	Qty	List Price/unit	Seller Multiplier	Total Cost	Provider
R35-01CP	Pressure Regulator	2	\$26.79	1	\$53.58	HJ Kirby
04F20O110 8ACF4C01	Normally Open Solenoid Valve	4	\$68.00	1	\$272.00	Kleen Rite
71215SN2MN 00N0C111C2	Normally Closed Solenoid Valve	2	\$51.33	1	\$102.66	Kleen Rite
4004-0039	Pneumatic Caliper Brakes	4	\$250.00	0	\$0.00	WC Branham
4000-1052	Friction Brake Pad	8	\$20.00	0	\$0.00	WC Branham
13Y892	Three Way Union Fitting	10	\$5.00	1	\$50.00	Grainger
13Y903	Four Way Union Fitting	6	\$10.00	1	\$60.00	Grainger
5038K97	Aluminum Piping	1	\$34.94	1	\$34.94	McMaster-Carr
4813K11	Stainless Steel Piping	1	\$17.84	1	\$17.84	McMaster-Carr
SUM-220984	Stainless Steel Braided Piping	1	\$47.69	1	\$47.69	Summit Racing
AAA00006	Flexible Pipe Fittings	8	\$6.99	1	\$55.92	Pit Stop USA
AAA81606	1/4" NPT Adaptors	8	\$2.99	1	\$23.92	Pit Stop USA
73450	8-32x3/8" Socket Head Bolt	12	\$0.22	1	\$2.68	Fastenal
1173449	10-32x3/4" Socket Head Bolt	8	\$0.45	1	\$10.80	Fastenal
2-1217	3/8-16x4" Grade 8 Bolt	12	\$0.35	1	\$2.80	Wholesale Bolts
3-72	3/8-16 Grade C Top Lock Nut	25	\$0.06	1	\$0.48	Wholesale
T6 6061 Aluminum (8"x8"x2")*		2	\$0.00	0	\$0.00	ESDC
Total Cost:						\$844.01

Table 8: Controls Bill of Materials

Product ID	Description	Qty	List Price/unit	Seller Multiplier	Total Cost	Provider
1585J-M4TBJM-2	Ethernet Cables, 4 Conductors, RJ45	3	\$44.95	0.27	\$36.41	Rockwell Automation
1783-ETAP	EtherNet/IP Tap3 copper ports	1	\$389.55	0.27	\$105.18	Rockwell Automation
Rocket M900	Network Access Panel	2	\$179.00	0	\$0.00	Ubiquiti
HG924-2TP-RSP	Wave Blade Antena	2	\$20.59	1	\$41.18	L-Com

Table 8: Controls Bill of Materials

Product ID	Description	Qty	List Price/unit	Seller Multiplier	Total Cost	Provider
5069-L3100ERS2	Safety Controller	1	\$13,860.00	0	\$0.00	Rockwell Automation
5069-RTB64-SCREW	RTB kit for 4/6 pin Screw type	1	\$59.50	0.27	\$16.07	Rockwell Automation
5069-RTB64-SPRING	RTB kit for 4/6 pin Spring type	1	\$59.50	0.27	\$16.07	Rockwell Automation
5069-RTB64-SCREW	RTB kit for 4/6 pin Screw type	1	\$59.50	0.27	\$16.07	Rockwell Automation
5069-HSC2XOB4	6 Channel 3 Wire High Speed Counter Module	1	\$944.00	0.27	\$254.88	Rockwell Automation
5069-RTB18-SCREW	Screw type terminal block kit	7	\$59.50	0.27	\$112.46	Rockwell Automation
5069-IB6F-3W	6 Channel 3 Wire Fast 24V DC Sink Input Module	1	\$505.00	0.27	\$136.35	Rockwell Automation
5069-FPD	Field Potential Distributor Module	1	\$151.00	0.27	\$40.77	Rockwell Automation
5069-RTB6-SCREW	6 pin Screw type RTB kit	1	\$16.38	0.27	\$4.42	Rockwell Automation
5069-RTB6-SPRING	6 pin Spring type RTB kit	1	\$16.38	0.27	\$4.42	Rockwell Automation
5069-RTB6-SCREW	6 pin Screw type RTB kit	1	\$16.38	0.27	\$4.42	Rockwell Automation
5069-OW4I	4 Channel Relay Output Module	2	\$284.00	0.27	\$153.36	Rockwell Automation
5069-IF8	8 Channel Voltage/ Current Analog Input Module	3	\$834.00	0.27	\$675.54	Rockwell Automation
1734-AENTR	EtherNet I/O Adapter Module	1	\$681.45	0.27	\$183.99	Rockwell Automation
1734-IB8S	8 Point Input Module	1	\$539.70	0.27	\$145.72	Rockwell Automation
1734-TOP	Terminal Base	4	\$19.47	0.27	\$21.03	Rockwell Automation
1734-OB8S	8 Safety Sourcing Output Module	1	\$627.90	0.27	\$169.53	Rockwell Automation
42CM-D8MNA-A2	Photoelectric Laser Sensor	2	\$198.79	0.27	\$107.35	Rockwell Automation
836P-D2NMGC58PA-D4	Solid-State Pressure Sensor	17	\$371.28	0.5	\$3,155.88	Rockwell Automation

Table 8: Controls Bill of Materials

Product ID	Description	Qty	List Price/ unit	Seller Multiplier	Total Cost	Provider
SCAXL-125G-12-SHX	Super OMEGACLAD™ Thermocouple Probes	11	\$47.90	1	\$526.90	Omega
TFMini Micro Lidar	Laser sensor	2	\$39.90	1	\$79.80	Amazon
ARDUINO UNO REV3	ATmega328P microcontroller	1	\$22.00	1	\$22.00	Arduino
W5100 Ethernet Shield	WIZNet ethernet chip	1	\$17.99	1	\$17.99	SainSmart
9398C-EDCTKIT1B	EducationalToolKit	1	\$221.00	1	\$221.00	Rockwell Automation
Total Cost:						\$6268.77

2.4 Pod Velocity Profile

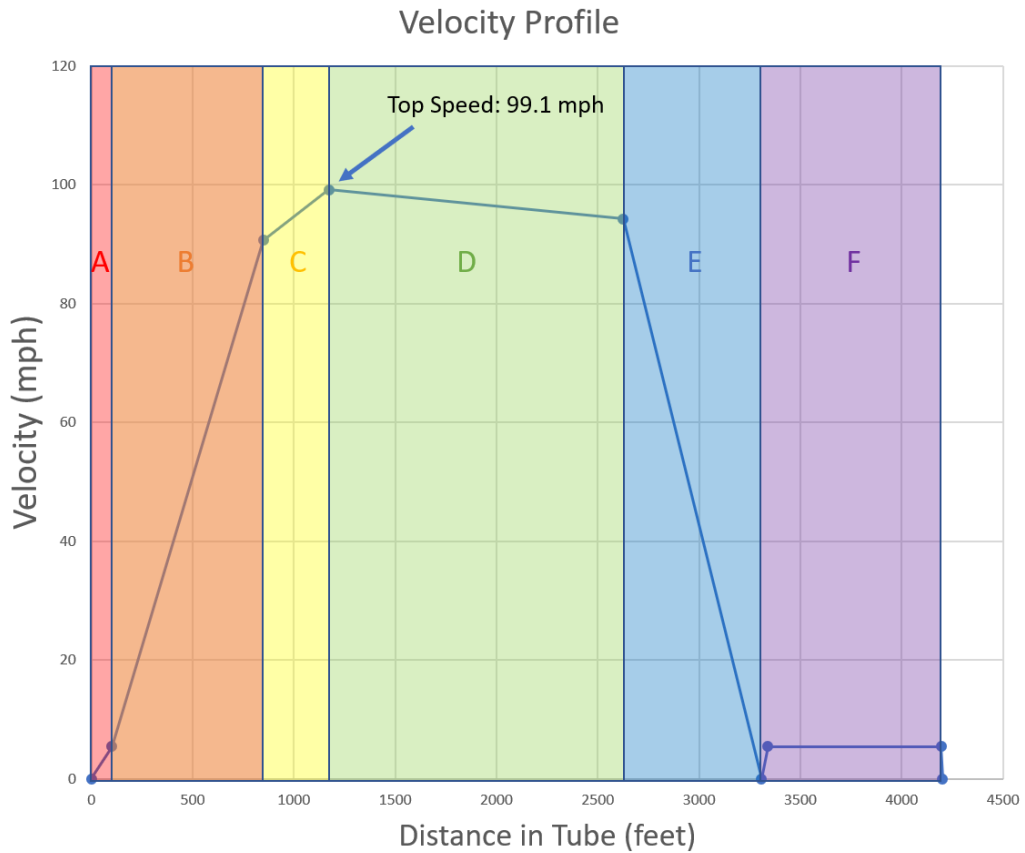


Figure 5: Pod Velocity Profile

The 2019 OneLoop pod's predicted velocity profile is displayed in Figure 5. Descriptions of the six acceleration regions can be found below the figure. The magnitudes of the forces that affect pod velocity, along with the sections of the report in which those forces are calculated, are tabulated in Table 9.

Table 9: Relevant Forces Affecting Pod Velocity

Force	Wheels Propulsion	Wheels Rolling Friction	Stability System Friction	Tri-gas Propulsion (supersonic)	Tri-gas Propulsion (residual/sonic)	Braking (Nominal)	Braking (Single Failure)
Magnitude	4.11 lbf (after friction)	6.94 lbf	0.43 lbf	60.1 lbf	22.48 lbf (avg)	46.90 lbf	23.45 lbf
Section	3.5.4	3.5.4	3.4.4	3.6.4	3.6.4	3.7.3	3.7.3

Region A: Crawl 1

At the beginning of the run, the motorized wheels on the pod will activate and accelerate the pod to a speed of 5.5 mph. These wheels will remain active until the pod reaches the 100-foot marker in the tube. During this time, system checks can be performed to ensure proper alignment with the I-beam prior to main propulsion. The relevant forces on the pod during crawl are the propulsive force from the wheels and the friction force of the stability system.

Region B: Primary Thrust

During the second propulsive stag of the run, the nozzles provide peak thrust (60 lbf) and the pod undergoes its highest acceleration. While this happens, the pod is affected by the friction of the wheels and stability system as well as the propulsive force from the nozzles.

Region C: Residual Thrust

In region C, the gas flow rate has fallen below the value necessary to choke, and sonic thrust is achieved. This is characterized by its low acceleration compared to the primary thrust region, despite the same set of forces being relevant.

Region D: Coast

During the coast region, the only forces affecting the pod's velocity are the friction forces from the wheels and stability system.

Region E: Brake

After coasting, the brakes engage and the pod experiences rapid deceleration. The case depicted in Figure 5 is for a single braking system failure. If both braking systems function nominally, then twice the depicted braking force would be applied and the pod would stop in half the time. The off-nominal case is presented to demonstrate that, even in the worst case scenario, the brakes are capable of stopping the pod well before the end of the tube. During braking, the braking force dominates all other effects on the pod.

Region F: Crawl 2

After the pod has stopped, the wheels power on and propel the pod back to 5.5 mph, after which point the controls system toggles the motor power to maintain a constant velocity. The velocity is intentionally kept low to ensure that the brakes can bring the pod back down to a stop in less than a meter. During region F, the relevant forces on the pod are the propulsive force from the wheels ad the friction force of the stability system.

2.5 Cost Breakdown and Funding

2.5.1 Current Funds

The total listed cost of the 2019 OneLoop pod is \$49,391.22. Our team has already secured \$30,695.36 of this total through sponsorships, discounts, and donated components. A breakdown of the remaining cost of each subsystem after these adjustments is given in Table 10.

Table 10: Cost by Subsystem

Subsystem	Power	Structures	Suspension/ Stability	Propulsion	Braking	Controls	TOTAL
Cost	\$735.32	\$2,936.39	\$752.87	\$7,158.50	\$844.01	\$6,268.77	\$18,695.86

Furthermore, our team has received quotes from two professional testing companies: one for hydrostatic proof/leak testing and one for thermo-vacuum environment testing. These quotes are not final, but instead are "Not to Exceed" (NTE) numbers, implying the costs of the tests will be less than or equal to the quotes.

Table 11: Professional Testing Costs

Test	Company/Sponsor	NTE Quote
Hydrostatic Testing	Consolidated Labs	\$1,000
ThermoVacuum Testing	NTS	\$3,050

Lastly, an additional \$2,500 is needed to account for unanticipated expenses. Therefore, the total amount of funding required for this year's pod is \$25,245. Next, this number is broken up into two purchasing phases. The first phase consists of what is needed to build and test the individual subsystems. This includes everything except for the vacuum testing cost (occurs after full pod is assembled), the controller hardware and I/O modules (control algorithm can be developed and tested long before it needs to be on the hardware), and the additional/miscellaneous funds. It follows that Phase II consists of those items excluded from Phase I. Therefore, the two funding phases are shown below.

Table 12: Funding Phases

Phase I	Phase II
\$18,105.25	\$7,140

Currently, our team has \$17,246.14 in funding that can be applied to these two phases. A breakdown of this number and its sources is given below. Therefore, we are capable of covering 95% of Phase I.

Table 13: Current Funds and Sources

Source	Professor Thomas Gordon (Donation)	Professor Michael Meyers (Donation)	Membership Dues	Current Account Balance
Amount	\$8,000	\$5,000	\$1,600	\$2,646.14

2.5.2 Plans for Future Funding

There are multiple plans in place to secure the rest of the funds required for Phases I and II.

CITRIS Tech for Social Good Grant

This is a \$5,000 grant that our team has been awarded with for the past two years in a row. We have submitted the application and, if awarded the grant again, will receive \$5,000 in March.

MAE Department Matching Funds

We have submitted an application for funding from the department of Mechanical and Aerospace Engineering at UC Davis. Typically, the department provides student teams a minimum of \$1,500. How much money is awarded is based on a combination of a team's prior competition ranking, proof of independent fundraising, and progress for the current year. We firmly believe that we satisfy all three categories and will likely receive more than the minimum \$1,500. Our faculty advisor is also attempting to secure us matching

funds based on the fundraising initiative and success we have demonstrated this year.

UC Davis Center for Student Involvement Conference/Event Grant

This is a grant the OneLoop has applied to that provides student organizations \$2,500 that can be used to host a conference or event. If we receive this money, it will go to the organization and hosting of a OneLoop Design Showcase for the UC Davis College of Engineering. This will give our team a chance to present our hard work to our peers and professors, as well as secure more donations from UC Davis faculty.

2.6 Production Schedule and Pod Readiness

Please refer to the attached folder labeled "Production Schedules" for detailed schedules of both subsystem and pod level production and testing

2.6.1 Pod Readiness

To ensure that our pod will be ready to race by the competition, OneLoop has focused a large amount of energy and resources on establishing an effective infrastructure to enable continued success throughout the next stages of the competition. Some detailed examples of this infrastructure are listed below.

- At the beginning of the year, we negotiated for more lab space based on our large number of members. We were successful in these negotiations, doubling our working space from last year and gaining access to three large work benches.
- We have secured 10 temporary Studio5000 licenses for our controls members, which they will use to develop the PLC control algorithm. These licenses were donated by Rockwell Automation, and they will be active until after the competition in August.
- We have organized a seminar to be held at UC Davis by a Rockwell Automation applications engineer, in which our members will be able to ask questions and gain experience with Studio5000 and the ins and outs of ladder logic. Rockwell has also committed to advising us on our control algorithm development.
- We have organized a process plan for the tooling of our propulsion nozzles and received permission to use our school's 5-axis DMG Mori CNC lathe to do the machining.
- We have fostered a healthy and productive relationship with the ESDC (Engineering Student Design Center) as well as the Mechanical and Aerospace Engineering department, resulting in key material (composites and stock aluminum) sponsorships and an open channel for advice from respected faculty.
- We have received permission from both the ESDC and prominent members of the MAE department to test our propulsion system. We were previously concerned that this would be a bottleneck in our schedule, since such permissions can be difficult to bureaucratically obtain.
- By securing such a large amount of funding so early in the year, we have shown important members of our department that we have the means to realistically compete in this year's competition.
- We have received a discounted quote to test our entire pod in a thermo-vacuum environment with NTS. This service will allow us to test all subsystems at 0.125 PSI prior and receive a vacuum-safety certification prior to the competition.
- Having secured 95% of Phase 1 funding at this stage allows our team to immediately purchase almost all of the components necessary to build and test our pod in the near future. Having this funding, along with the high likelihood of more funding in the near future prevents us from wasting time waiting on more resources to purchase or manufacture components.

3 Subsystem Design

3.1 Power System

3.1.1 Technical Description

There will be two separate power systems on the pod. One system will be for the PLC, sensors, valves, etc., and consists of two 24V battery packs. The main pack will be for normal operations, and a backup pack will be for emergency situations. Normal operations are when there are no critical problems with the pack, such as overheating or current overload, while emergency situations are defined as when such problems exist.

The second power system will contain one 12v battery pack for the motors that run the motorized wheels, which will bring the pod to the end of the track after the run is complete.

All three packs consist of the Li-ion cells in cylindrical form, battery management systems for the main and secondary packs, protecting circuits as backup, and fuses.

3.1.2 Design Rationale

The Li-ion cylindrical cells advantages outweigh other cell chemistries and forms while still being safe.

Cell Selection

Cylindrical cells are easy to assemble and more ubiquitous than other geometries. Pouch cells are more efficient when it comes to space constraints and weight, but are prone to punctures and hazards under vibrating environments. This makes the pouch type undesirable for this application. Prismatic cells are sturdy, and are good for high powered electric vehicles, but due to weight concerns and the fact that our pod design does not require high voltage, the cylindrical cells are preferable.

Availability and Ease of Manufacturing

The cells and components are off-the-shelf and can be bought to save time on design and assembly. Additionally, manufacturing the battery modules will require less time and effort with Vruzend battery kits. This reduces manufacturing time, allowing more resources for testing.

3.1.3 Design

Power Requirements

Tables 14-16 contain the power requirements of our pod systems.

Table 14: Primary System Power Requirements

Subsystem	Voltage	Power Consumption	Max Current
PLC MOD Power	24 V	120 W	0.54 A
PLC SA POWER	24 V		0.01 A
NAP	24 V	6.5 W	1 A
PLC Sensors	24 V	185 W	0.5 A
Propulsion Valves (S-1 through S-5)	24 V	15 W	0.6 A
Braking Valves x 6	24 V	60 W	2.5 A

Table 15: Secondary System Power Requirements

Subsystem	Voltage	Max Power Consumption	Max Current
DC Motor x 2	12 V	674 W	67 A

Calculations

Primary (main) Module: Estimated runtime of 30 minutes

We compromised for extra capacity to ensure that the module has more than enough capacity for the duration of the run and during loading, unloading, and standby. We designed for 80% more energy than the calculated requirement to balance the weight-to-performance ratio.

Power requirement: $0.387\text{kW} * 0.5\text{h} = 193.5\text{kWh}$

Total energy with 80% increase: $0.194\text{kWh} * 1.8 = 0.348\text{kWh}$

The PLC requires 24VDC, necessitating 7 series connections.

Capacity desired: $0.348\text{kWh} / 24\text{V} = 14.5\text{Ah}$

Each cell's capacity: 2.5Ah

Therefore, the module requires 6 parallel connections.

Secondary Module: Estimated runtime of 11 minutes

20% more energy than the calculated requirement is provided, ensuring that there is sufficient power for the wheels during the crawl state. This also minimizes any unnecessary weight or cost of the module.

Power requirement: $0.18\text{h} * 700\text{W} = 0.128 \text{ kWh}$

Total energy with 20% increase: $0.128\text{kWh} * 1.2 = 0.154\text{kWh}$

The DC motors require 12VDC, necessitating 4 series connections.

Capacity desired: $0.154\text{kWh} / 12\text{V} = 12.8 \text{ Ah}$

Each cell's capacity: 2.5Ah

Therefore, the secondary module requires 6 parallel connections

Primary (backup) Module: Estimated runtime of 15 minutes

In the event of a main pack failure, this module has the same voltage requirement as the Primary (main) module, and identical capacity to match the Secondary module's runtime and to keep the PLC running in unloading phase.

Since the main module has an estimated runtime of 30 minutes and 6 parallel connections, the backup module will have 3 parallel connections.

Table 16: Battery Specifications

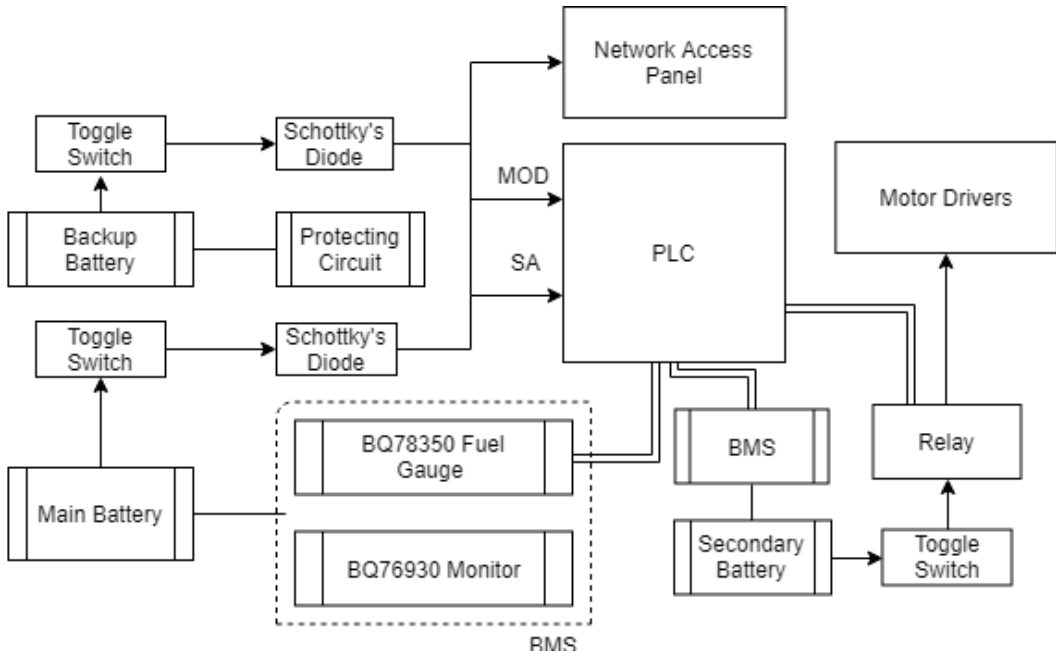
	Primary (Main)	Primary (Backup)	Secondary
Cell Supplier	LG Chem	LG Chem	LG Chem
Cell Chemistry	Li-ion	Li-ion	Li-ion
Cell Capacity	2.5 Ah	2.5 Ah	2.5 Ah
Manufacturing	Off the shelf	Off the shelf	Off the shelf
Configuration	7s6p (42 cells)	7s3p (21 cells)	4s6p (24 cells)
Tot. Energy Stored	0.378 kW-hr	0.189 kW-hr	0.216 kW-hr

Table 16: Battery Specifications

	Primary (Main)	Primary (Backup)	Secondary
Module Voltage	25.2 V	25.2 V	14.4 V
Module Capacity	15 Ah	7.5 Ah	15 Ah
Max Cont. Current	120A	60A	120A
Peak Current	10A	10A	58A
Nom. Current	6.5A	6.5A	N/A
Operating Temp. Range	-4F to 140F	-4F to 140F	-4F to 140F

Table 17: Packs Weights & Dimensions

Pack	Dimensions (in x in x in)	Weight (lbs)
Main	5.25x4.50x3.625	~6
Secondary	3.00x4.50x3.625	~4
Backup	5.25x2.25x3.625	~3



Note:

— Communication

→ Wired Connection

Figure 6: Power System Block Diagram

3.1.4 Fuses

Each individual cell will be connected to a nickel bar via 20A rated fuse wires. Parallel connections are done via thick nickel bar, and series connections through thin bus bars. Figure 6 displays how the fuses

will be installed with the VRUZEND battery kits.

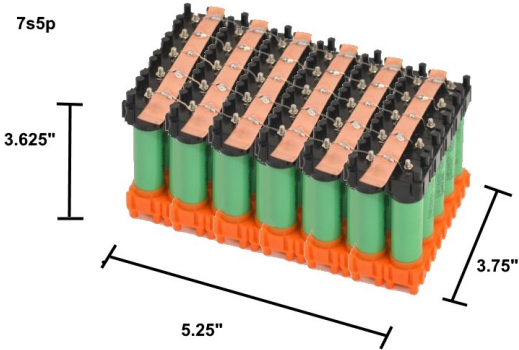


Figure 7: Battery Module

3.2 Chassis/Mounting

The purpose of the chassis is to provide mounting for subsystems and absorb loading from the pod's high speed environment. The total weight of all structures is estimated to be 83lb and yields a center of gravity located at the longitudinal center of the pod, 5.24" above the I-beam. The following sections provide an overview and rationale of the pod's structural design, as well as detailed design and supporting analysis.

3.2.1 Technical Description

Figures 8 and 9 provide a technical overview of the chassis and its mounting structures. The chassis is a TIG welded space frame structure shaped like an inverted U. C-channels supported by triangular brackets and L-shaped rails are attached to the sides of the chassis to provide mounting for eight propulsion tank clamps. A trapezoidal support structure is fastened to the aft end of the chassis to provide mounting for the gas nozzle flange. Modular composite mounting plates are attached to both the top surface of the chassis and its sides for the controls and pneumatic systems. Alignment pins and latches are used for the alignment and fastening of the aerodynamic shell to the chassis. Four hoist rings are located at the four corners of the chassis to allow loading and unloading by forklift. Slots are cut into the chassis for wire routing.

With the exception of the fiberglass/honeycomb composite mounting plates, all structures consist of 6061 T6 aluminum stock. Fasteners include a combination of pop rivets, rivet nuts, bolts with safety wire, and locknuts to ensure positive locking of all critical components.

3.2.2 Design Rationale

The chassis aluminum space frame design shown in Figure 9 was the result of trade studies on various materials and orientations. This section details the chassis' chronological conceptual design process.

At the beginning of the design process, material selection for the chassis led to choosing aluminum tubing over composites and aluminum plating. Table 18 shows an overview of the material selection trade study. Although composite materials have a higher strength to weight ratio than that of aluminum, we lacked the experience, facilities, and funding necessary to manufacture custom composite panels reliably. The use of bolted aluminum plating was considered due to its ease of manufacturing, but preliminary weight analyses showed that the structure would far exceed the self-imposed 40lb chassis requirement. As such, a 6061 T6 aluminum TIG welded space frame structure was chosen due its relatively high strength/weight efficiency and ease of manufacturing for students. Note that TIG welding services were offered by a professional welder and legacy usage of space frame structures from OneLoop's 2015-2018 chassis design

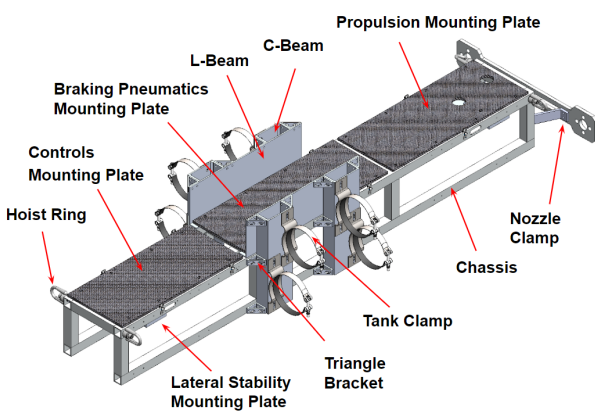


Figure 8: Structures Overview

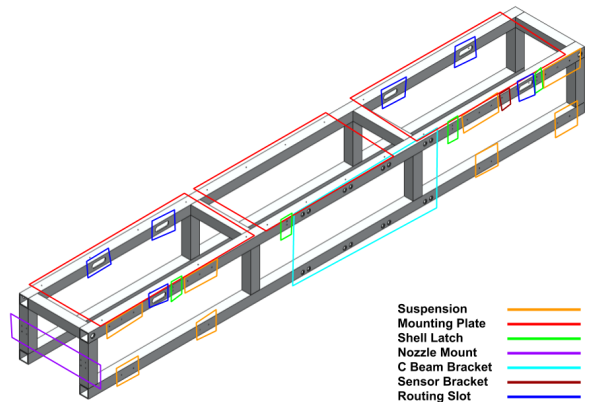


Figure 9: Chassis Design

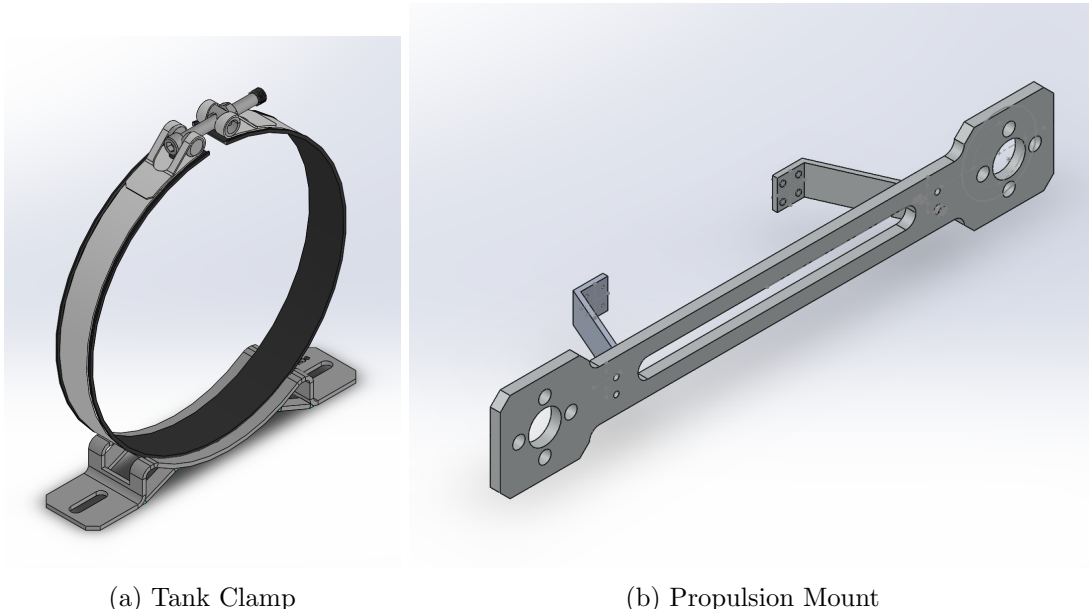


Figure 10: Propulsion Mount Design. Tank Clamp (left) and propulsion mount (right) are as shown.
Note that the tank clamp is used for reference only.

provided additional experience with its design, manufacturing, and testing. Note that the welder has 30 years of welding experience and has welded for Tesla before.

Table 18: Material Selection Trade Study for Chassis

Parameter	Aluminum TIG Welded Space Frame	Aluminum Plating	Composite Panels
Strength/Weight Ratio	Yellow	Red	Green
Ease of Manufacturing	Green	Red	Red
Ease of Design	Green	Yellow	Yellow

Once a space frame design was chosen, the chassis' inverted U shape was chosen. This choice was largely driven by the requirement to achieve a low pod center of gravity. Since braking loads are applied on the top flange of the I-beam, a low vertical center of gravity is desirable to minimize additional bending stress on the pod's chassis and stability systems. Thus, the inverted U-shaped chassis was chosen to allow the heaviest components (i.e. the propulsion system) to be mounted on the chassis side with their local center of gravity located as close to the ground as possible. Another benefit of the U-shaped space frame design is its modularity, allowing components to be mounted vertically or horizontally at any position along the chassis' top or side surfaces. This flexibility in subsystem attachment allows the mounting locations of components to be easily moved as necessary to provide space for other components; thus, allows for lenient subsystem redesigns, and shifts the pod's center of gravity without requiring a redesign of the chassis.

With the space frame design chosen, the chassis' cross section was initially arbitrarily chosen to be $1.5 \times \frac{1}{8}$ " square tubing. This geometry was chosen in response to problems regarding a lack of mounting space and strength with the $1 \times \frac{1}{16}$ " square tubing used in the 2015-2018 OneLoop chassis. Analysis given in following sections show that the resulting chassis far exceeds its necessary strength. In addition, if higher load cases are ever encountered, the chassis can be easily re-designed by increasing the thickness of its square tubing.

After the design of the chassis, all other structural components were designed as necessary to support other subsystems. See the following section for more details.

3.2.3 Design

Chassis

The chassis' design requirements are as follows:

- *Structural integrity under dynamic and static loads.* Critical loading scenarios were identified as during braking, propulsion, crashing, weight, hoisting, and vibration.
- *Structural integrity under vibration.* The natural frequencies of the chassis cannot be excited by the vibration environment during the pod's run.
- *No interference with components due to deflection.*
- *Provide wire routing for pneumatics and controls.*
- *Provide mounting for all components.*

To meet these requirements, the chassis is designed as a space frame consisting of sixteen $1.5 \times 1/8$ " T6 6061 aluminum square tubes. All tubes are welded at 90 degree angles for simplicity and to decrease manufacturing time. The final design weighs 28.6lb and is $82.5 \times 11.5 \times 9.5$ (LWH)", around the size of a twin-sized bed. Aluminum tubing will be sourced in compliance with ASTM B221-14. Tubing will be TIG welded by a professional welder in compliance with AWS D8.14. If necessary, a wooden jig will be built to assist in the welding process to ensure dimensional accuracy. A preliminary chassis will be built and failure tested to ensure its structural integrity under the expected load envelope. A final chassis will be built following failure testing and used on the final pod assembly. See structures test program for more details.

Figure 8 provides an overview of all chassis features and holes. Features are as follows:

- *Wire routing slots.* Eight 0.75" diameter slots are cut to provide wire routing for the braking pneumatics, as well as miscellaneous control wires. Note that the braking pneumatic wires are the largest of the routed wires, sized at 0.55" in diameter, and should easily fit through the chassis' 1.25" inner tube width.
- *Rivet nut / rivet holes.* Holes are drilled into the chassis to be used for $\frac{1}{2}$ -13, $\frac{3}{8}$ – 16, $\frac{1}{4}$ -20, 10-24, and M10-1.5 rivet nuts, as well as $\frac{1}{8}$ and $\frac{1}{4}$ rivets. Counterbores, drilled to a maximum depth of 0.04", are used for all rivet nut holes to provide a flush mounting surface. All holes are sized and prepared in accordance with MIL-R-47196A for rivets [2]. As a rule of thumb, all holes are also spaced a minimum of 1.5x their diameter from their center to edges.

Several FEA analyses under critical loading scenarios were performed using ANSYS Static Structural. It was found that the chassis far exceeded failure for all cases, with the nozzle mount expected to fail first. A modal analysis of the chassis was also performed, yielding its natural frequencies. It is important to note that the actual vibration environment is difficult to predict, and subsystem testing is required to determine actual frequencies. As such, it has not been determined yet as to whether the chassis' natural frequencies are excited. If testing indicates that a subsystem (e.g. propulsion) will indeed excite the chassis' natural frequencies, rubber vibration isolation pads at the subsystem's mounting location as necessary. This practice is commonly used to protect satellites from the high vibrations due to launch via rocket [16].

Controls/Pneumatics Mounting Plates

The mounting plates are required to support the weight of components without failing under bending. As such, composite floor paneling (BMSS4-17H, TYPE 1) made from fiberglass and a Nomex honeycomb core was deemed an ideal material due its low weight and high bending strength. These panels will be machined via waterjet, and press fit with through-hole inserts designed specific for Boeing floor panels to allow mounting via bolts.

Modeling the composite floor panels as a fixed-fixed beam with a distributed load applied at its center, an 8x24" section of panel was proof tested by having a 176lb student stand on top of it as shown in Figure 11. The mounting plate most likely to fail is the braking pneumatics mounting plate (10x24" with 24lb of weight applied) with a proven factor of safety of 7.



Figure 11: 2-point bending test of composite panels

Fittings

To ensure positive locking of all critical components (i.e. components whose failure would affect the functionality of the pod), a standard for fittings was set for all structures including braking and stability as is shown in Table 19. In general, pop rivets are preferable over nuts/bolts for mounting to the chassis' square tubes since they do not cause unnecessary stress when applied and weigh less. However, rivet nuts and wire lockable screws are used in cases when the component is attached to the chassis, but removable screws are preferable. For components not directly attached to the chassis, nylon lock nuts or split nuts and screws are used instead due to their ease of assembly/disassembly.

Table 19: Fitting Standards

Fitting Type	Application
Pop Rivets	Component is attached to chassis
Wire Lockable Screw + Rivet Nut	Component is attached to chassis, but screw required
Screw + Lock Nut	Component is not attached to chassis
Screw + Split Nut	High Temperature Applications

For superior strength, steel is chosen for all fitting materials unless otherwise specified. Note that all rivets are installed in accordance with MIL-R-47196A for rivets and all bolts are torqued to their required values. See supplemental documentation for a table of bolt torques used for all critical components.

Propulsion Mounts

As shown in Figure 8, the propulsion mounts are split into two sections: eight tank clamps (mounted to four C beams) and a nozzle support structure (mounted to the chassis). C beams, supported by an angle beam, are designed to offset the thruster valve assembly to avoid interference with the propulsion system. Under nominal braking conditions, the clamps and nozzle support are designed to support the propulsion assembly's weight and axial inertial force. Under nominal propulsion conditions, the nozzle support structure is designed to reduce nozzle vibration, and transmit thrust from the nozzles to the rest of the pod.

Each C beam utilizes thick aluminum and are fastened to the chassis and angle beam via triangular brackets. The thickness of the C-beam, angle beam, and brackets are $0.17"$, $\frac{3}{16}"$, and $\frac{3}{16}"$, respectively. $\frac{1}{4} - 20$ bolts and rivet nuts are used for all fastening.

Designed specifically for high dynamic load applications, the tank clamps are purchased from HYDAC. See supplemental documentation for specific product information. The clamps consists of an epdm rubber padded steel band welded to a steel web-reinforced support. M10 quick-release swivel bolts, used for quick assembly/disassembly, will be used in conjunction with a nylon lock nut to ensure that clamping is positively locked under vibration. Mounting is achieved using M10 rivet nuts and wire lockable bolts. The nozzle support structure consists of a $\frac{1}{2}"$ middle plate for flange mounting and two $\frac{1}{2}"$ angled plates used for triangulation support. All plates are machined from T6 6061 aluminum. $\frac{1}{4} - 20$ locknuts/bolts are used to fasten plates together, and eight $\frac{1}{8}"$ pop rivets are used to fasten the entire structure to the chassis. Bolt holes are oversized to allow for alignment of the nozzles prior to securing the tanks with its clamps. If necessary, spacers can be inserted on the middle plate's face to ensure the nozzles are pointed along the pod's longitudinal axis.

Hoisting Mounts

The chassis must be lifted onto the stage via forklift. As such, four $\frac{3}{8}$ -16 steel hoisting rings are placed at the four corners of the chassis, and will be lifted via spreader bar and ratchet straps. This configuration was used such that the straps and the sides of the aerodynamic shell are always parallel, prevent interference from occurring during lifting. See the loading/unloading plan for more details.

3.2.4 Structural Analysis

This section outlines the major load cases for the pod, and the resulting effect on components.

Braking Case

During braking, the structural integrity of the chassis and its mounting structures must be analyzed. Assuming emergency braking, the brake calipers apply a total of 1281N, decelerating the pod at $0.82g$'s. First, the propulsion system must be analyzed under this deceleration to determine whether the tank clamps fail. As shown in figure 12, the tanks and thruster valves are modeled as two beams, fixed at the tank clamps and propulsion assembly. Inertial loads are applied at the center of gravity of both the tanks and valves. This model also assumes the following:

- *Ignore the effect of all pneumatics located above the bottom tank.* Note that the joint strength of the $\frac{1}{4}$ NPT threaded pipe is estimated to be 457lb in supplemental documentation. Assuming the

entire inertial load of the propulsion system (150lb) is applied at a single joint, the pipes have a factor of safety of 3 and are still not likely to fail. By removing all upper pneumatics, this is a worst case scenario.

- Assume tanks are full.
- All thruster valves are of constant cross sectional area.
- Fixed tank clamp supports are located at the end of the tank. Since the aft-most tank clamp is most likely to fail, assuming the clamp is closer to the inertial load from thruster valve mass will increase the load the clamp carries. As such, this is another worst case scenario.

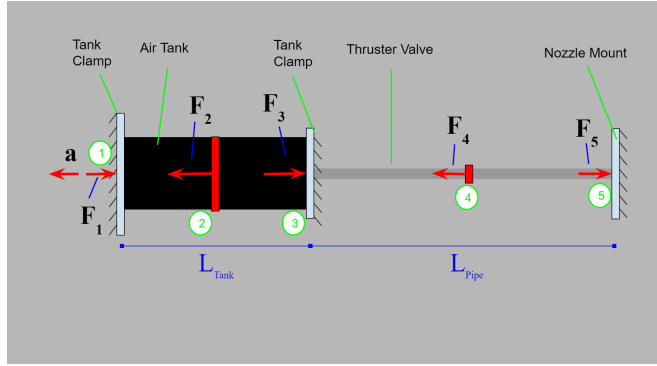


Figure 12: Load Schematic for Braking Case

The maximum force is derived in supplemental documentation, where the force F_3 on the aft-most tank clamp (3) is given by the following equation:

$$F_3 = \frac{1}{1 + x_{\text{pipe}}/(L_{\text{pipe}} + x_{\text{pipe}})} F_4 + \frac{F_2}{2} \quad (1)$$

Where the inertial loads of the tanks and thruster valves are F_2 and F_4 , respectively. Note that $F_2 = m_2 a$ and $F_4 = m_4 a$. Evaluating with $x_{\text{pipe}} = 16"$, $L_{\text{pipe}} = 40.3"$, $m_2 = 12.52\text{lb}$, $m_4 = 26.2\text{lb}$, the tank load versus acceleration curve is determined and displayed in figure 13 below.

Using figure 13, the expected load under braking is 21lb. The tank clamps are rated for an axial load of 141.6lb, so the Factor of Safety is 6.74. As such, the tank clamps are not expected to fail under braking, and can be used as fixed boundary conditions in pod-level analysis.

An ANSYS Static Structural simulation was created to model this scenario as shown in figure 14. Note that all non-structural components are treated as point masses located at their respective center of mass. Boundary conditions are set at the linear bearing mounting holes of the stability system mounting plate. The only loading condition is deceleration at 0.82g's.

The resulting stress distribution was found to create stress concentrations at the nozzle mount as shown in figure 15. The maximum stress is 1155.8PSI, with a resulting factor of safety of 35 under yielding. As such, the nozzle mount will not fail under these loads.

Crashing Case

In the unlikely case of brake failure, the pod will crash into the foam pit at the end of the tube. Upon impact, the front of the chassis is fixed, with all its mounted components lurching forward. We are most concerned with the resulting scenario where the high-pressure pneumatic system ruptures, causing the tanks to become a dangerous projectile. As such, the structural integrity of propulsion system must be analyzed.

The maximum speed of the pod is 44.7m/s when it is approximately 800m away from the end of the tube. The total resistive force on the pod is 40.8N due to aerodynamic drag and friction, decelerating the pod at 0.026g's. Applying kinematics, the maximum speed of the pod is 39.8m/s at the end of the tube.

An ANSYS explicit dynamics simulation was then run, modeling the impact behaviour of the pod crashing into foam as shown in figure 16. The resulting crash deceleration was found to be 3.87g's. See

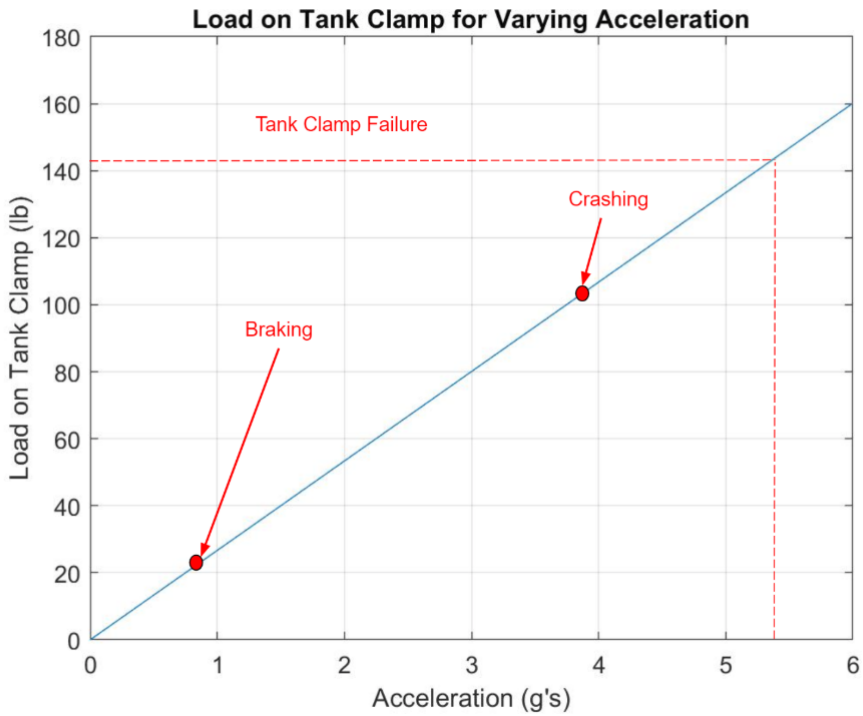


Figure 13: Load on Tank Clamp for Varying Acceleration

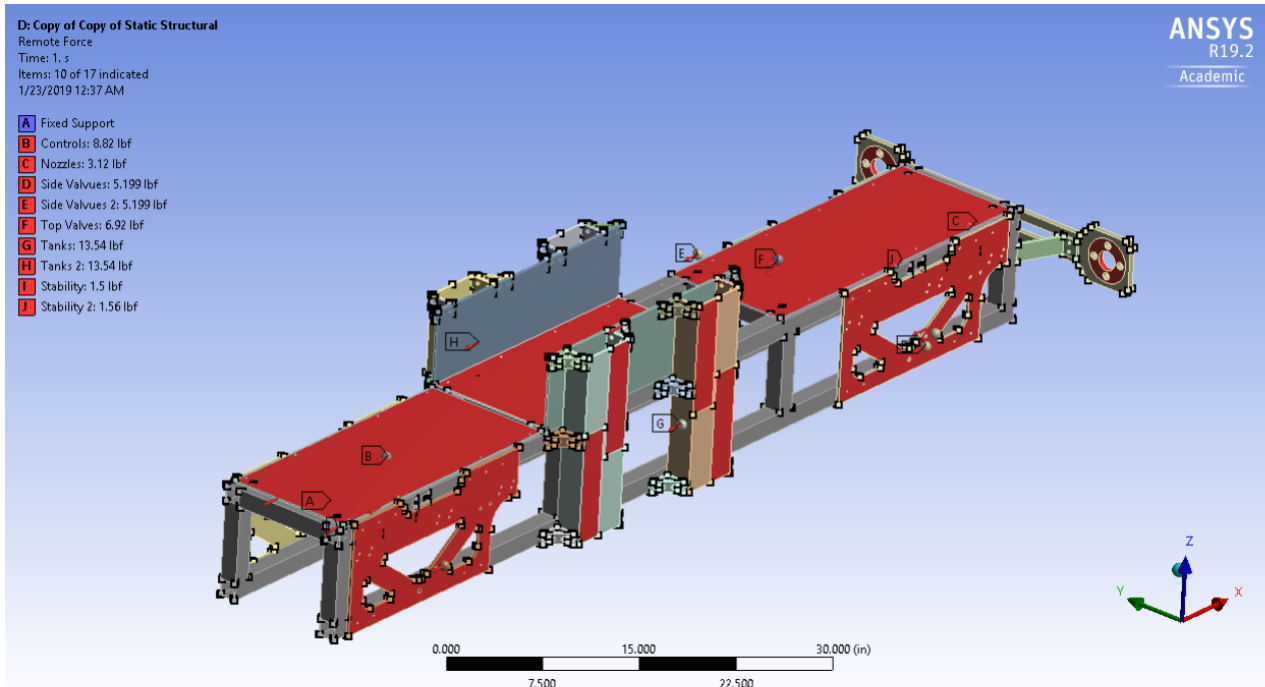


Figure 14: Chassis Static Structural Analysis Under Braking Loads

supplemental documentation for specific details on the analysis.

Since the NPT pipes are structurally sound under 15.5g's as calculated in the previous section, the pneumatic piping will not break. Referencing the tank clamp analysis in figure 13, crashing at 3.87g's results in 103lb of force applied to the tank clamp. As such, the tank clamp's factor of safety is 1.37, so the clamp will not fail. Although this factor of safety is below SpaceX's requirement of 3, it is acceptable since crashing is an off-nominal scenario.

For thoroughness, it is still assumed that both tank clamps fail under the 103lb crashing load. In this case, the tanks are expected to shear through the tank clamp's rubber and is only supported by the

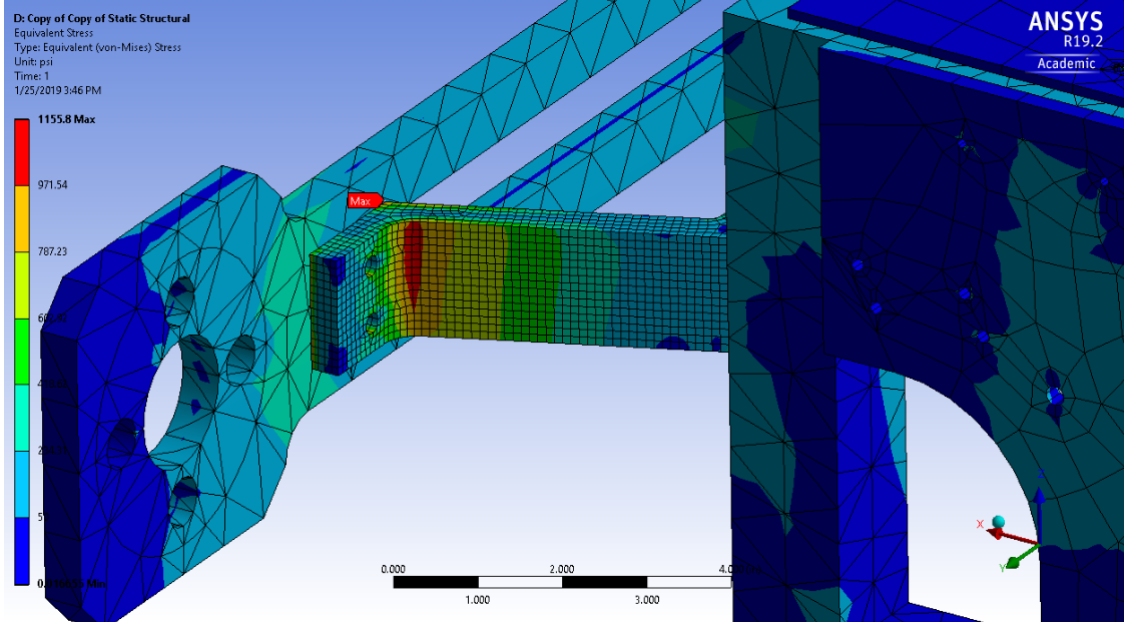


Figure 15: Chassis Static Structural Analysis Under Braking Loads

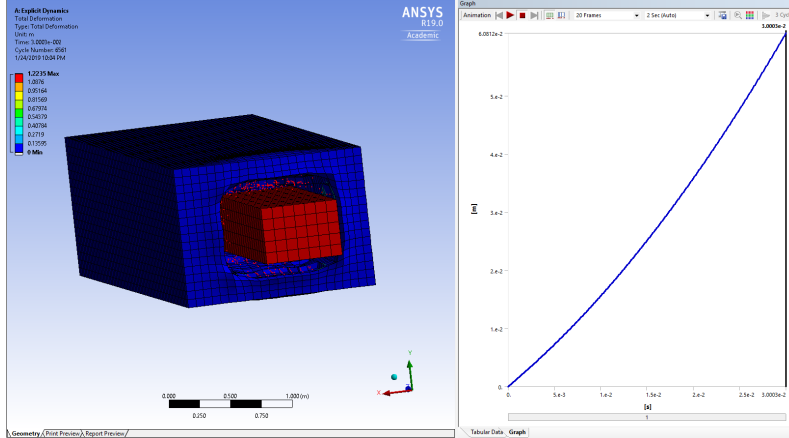


Figure 16: ANSYS explicit dynamics model of pod crashing into foam. Note that the pod is modeled as box with its outer dimensions as a worst case scenario.

strength of the nozzle mount. The force applied on the nozzle mount is due to the 51.2lb of supported mass (thruster valves, both tanks full of gas, and nozzle) decelerating at 3.87g's, resulting in a 198.2lb force applied to each flange connection points of the nozzle mount. Applying this inertial load as a distributed load in ANSYS static structural, the stress distribution is Section 17 was obtained. As shown in figure 17, the crashing load results in a maximum stress of 13.0kPSI at the bracket joints with a yield and ultimate factor of safety of 3.0 and 3.46, respectively. As such, even in the unlikely case of tank clamp failure, the nozzle mount will not break under inertial loading. Furthermore, the pneumatic assembly will not rupture, and will stay connected to the chassis during the entire crashing scenario.

Vibration Case

During the run, vibration will occur due to a variety of sources on the pod. Similar to that of a rocket engine, the tri-gas thruster system will likely create high frequency vibrations that may possibly excite the natural frequencies of structural components. We are primarily concerned about the nozzle mount under these vibrations, whose failure would be catastrophic for the pod. As such, the its first 6 resonant frequencies were calculated in ANSYS Modal as shown in table 20 and 21 below. Until the tri-gas thruster system is tested, we will not know whether the resulting vibration will cause resonance in the mount. In the case that a resonant frequency is excited, vibration isolating dampeners or a redesign may be needed.

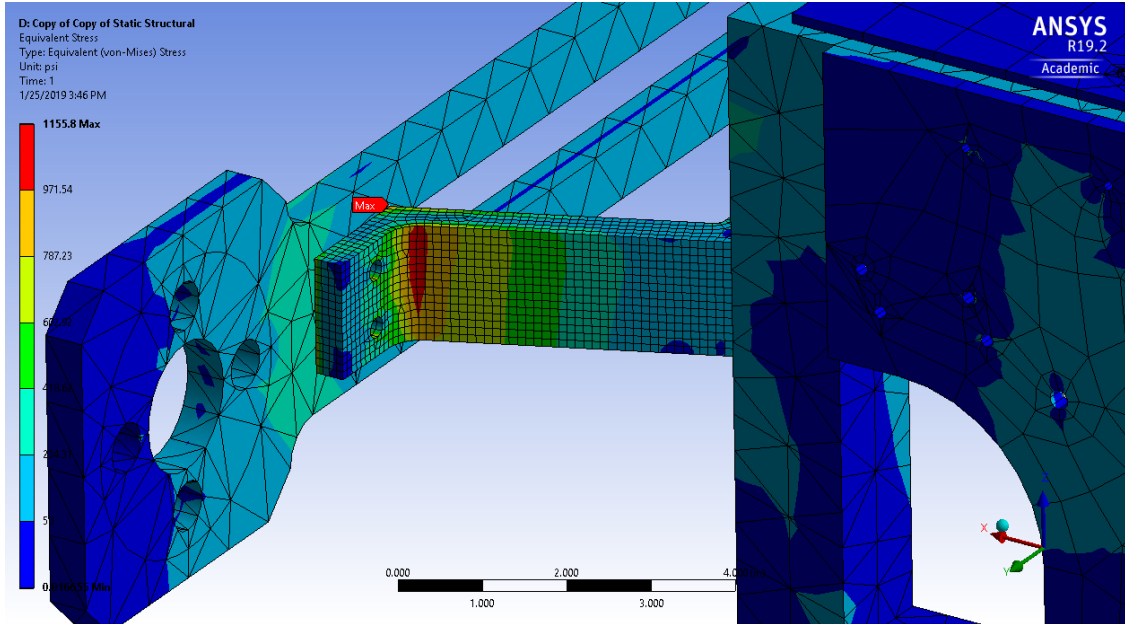


Figure 17: Crashing Case Load Applied to Nozzle Mount

Table 20: Resonant Frequencies of Nozzle Mount

Mode	1	2	3	4	5	6
Frequency (Hz)	162.22	269.39	276.94	411.93	461.53	481.21

Table 21: First 6 Modal Frequencies of Chassis

Mode	1	2	3	4	5	6
Frequency (Hz)	61.045	77.558	95.707	113.7	120.42	146.05

Chassis: Propulsion

The propulsion analysis was done similarly to the braking analysis. The purpose of this analysis is to see the stresses caused by the acceleration of the components attached to the chassis. Each component of the pod is represented by a point mass and attached to the chassis at their respective mounting points, and then 64.5 lbf was applied to the nozzle mount. As shown in Figure 18, the maximum stress experienced was 868.7 PSI. Given the yield strength of aluminum is 40 kPSI, the safety factor is 46.

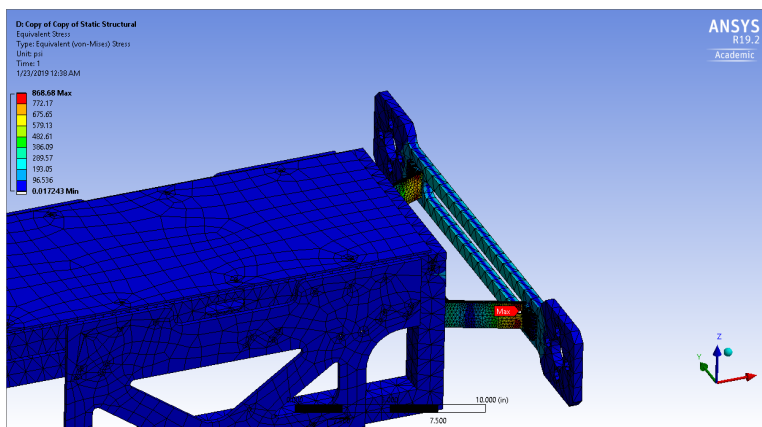


Figure 18: Chassis: Propulsion Analysis - Stress

Weight

ANSYS Static Structural Analysis was used to determine the maximum weight capacity of the chassis as it rests on the four suspension systems. By applying the load at the center of the top layer, this simulated the greatest stress that chassis could undergo under this case. As a result, the maximum load before the chassis experiences plastic deformation is 3507 lbf. During competition our chassis will hold 320 lbs, and therefore the chassis has a SF = 11 before yielding.

As Figure 20 shows below, the maximum deflection under 3507 lbf loading case is 3.37 mm (0.132 in), which occurs in the middle of the two longest square tubes on the top layer of the chassis. This is not a concern as the applied load to reach this deflection is 10 times the expected load, and there are no components that are affected due to this deformation.

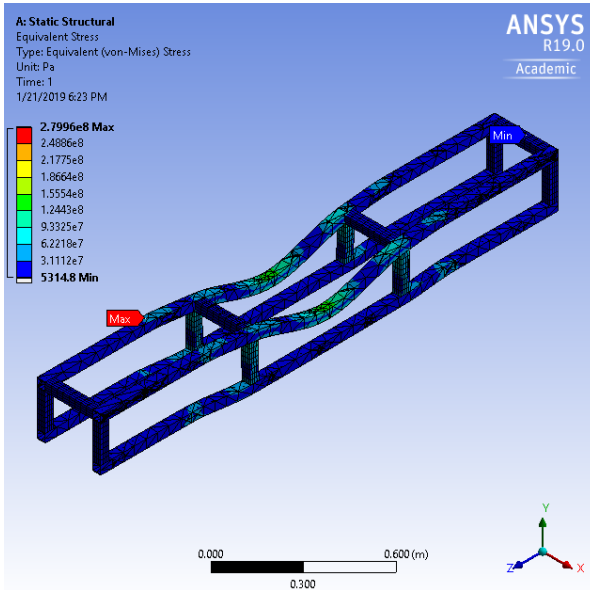


Figure 19: Chassis: Weight Analysis - Stress

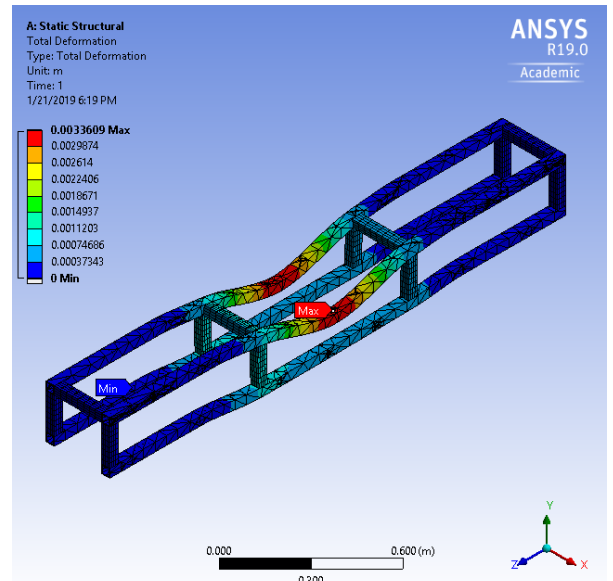


Figure 20: Chassis: Weight Analysis - Deflection

Vibration Case

Table 22: Modal Frequencies

Mode	1	2	3	4	5	6
Frequency (Hz)	4.3283	5.1021	6.7068	7.1429	24.286	28.003

Hoisting Case

The pod will be lifted from the ground to the staging area via forklift. See loading/unloading section for more information. During this time, the hoisting hooks and ratchet must be structurally sound for lifting. Since the straps are to be angled at 60deg from the horizontal, a simple force equilibrium will determine that the applied load to each strap and hoisting ring during lifting is 100lb. Rated for 1000lb each, the $\frac{3}{8}$ -16 threaded hoisting rings maintain a factor of safety of 10. Rated for 3300lb, the straps maintain a factor of safety of 33. The setup is thus extremely safe during lifting.

The chassis' structural integrity must also be investigated via FEA analysis. Fixed boundary conditions were applied to the holes using for mounting the hoisting rings. A 350 lbf load (the weight of the pod) was applied at the center of the top square tubes, assuming a worst case scenario for non-uniform weight distribution. It was found that the maximum stress and deflection experienced by the chassis is 33 MPa and 0.518 mm (0.0204 in) respectively. This results in a yield factor of safety of 8.4, so we are not concerned.

Nozzle Support: Propulsion

The propulsion loads are estimated to be 267 N per nozzle at max pressure, as shown in Section 3.6.3. The analysis was conducted at a worst-case scenario by applying all thrust loading to the propulsion mount. An ANSYS Static Structural analysis with fixed boundary holding the mount in place on the chassis,

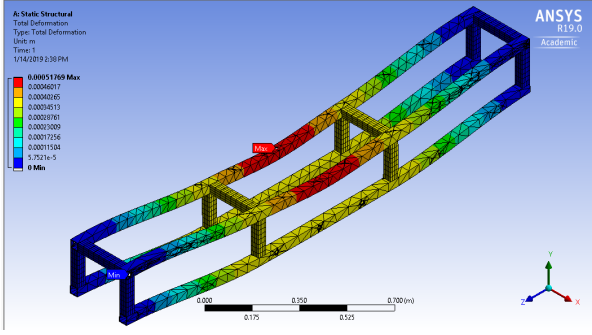


Figure 21: Chassis: Hoisting Analysis - Deflection

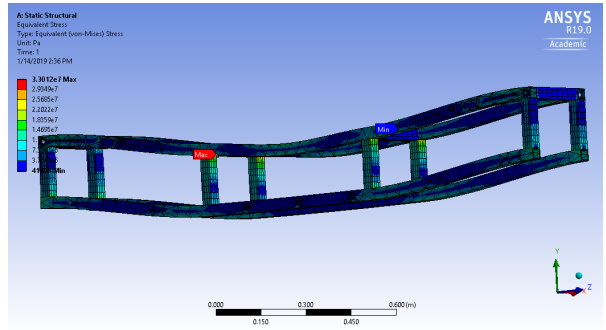


Figure 22: Chassis: Hoisting Analysis - Stress

the load was applied to the inner circular surface of the propulsion mount to simulate the worst-case nozzle loading. A triangular mesh was used with 0.02 element sizing and three successive refinements at the max stress location. The rivets were modeled with beam connections and the bolts with simplified models under 100 lbs of pretension.

3.3 Aerodynamic Shell

3.3.1 Technical Description

Our shell design is separated into three sections: front, middle and back. Each component will be manufactured out of $\frac{1}{32}$ " 6061-T6 aluminum sheets and fastened to $\frac{1}{16}$ " ribs with rivets as depicted in figure AS1. After analyzing the expected drag force, it was deemed that at a pod speed of 125 mph with tube pressure at 0.125 PSI, a partially covered aerodynamic shell was sufficient. The shell's coefficient of drag is estimated to be 0.74 and produces a maximum of 0.1 lbf of drag at the pod's maximum speed of 125 mph.

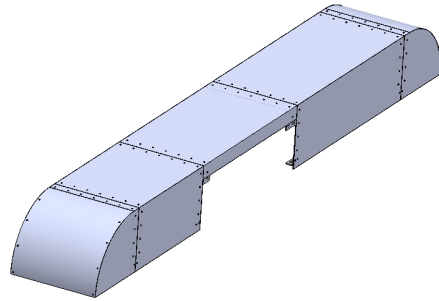


Figure 23: Isometric View of Aerodynamic Shell

3.3.2 Design Rationale

Due to the low ambient pressure of 0.125 PSI, the team decided that at our predicted speed of 125 mph, our expected drag forces were negligible. Therefore the shape had a minimal effect on the aerodynamic drag, and as a result the team designed the aerodynamic shell with a simpler geometry. Therefore the question that was left to answer, was what material should be chosen.

Carbon composites was a potential option; however, due to the lack of experience and resources to produce a custom composite aerodynamics shell, it was decided that it was more difficult to work with than 6061 aluminum given our aggressive production schedule. Ultimately, aluminum was chosen because of the cost efficiency, the high strength/weight ratio and the ease of manufacturing.

3.3.3 Design

The major design driver of the aerodynamic shell is the weight limit of 10 lbs. This requirement is necessary to meet the 350 lb overall pod weight limit, and to improve our maximum speed by maintaining the lowest possible weight. By implementing an aerodynamic shell only where critical electronics and pneumatics are located and using structurally efficient ribs, allowed the aerodynamic shell to weigh 10 lbs.

Simple geometries for our shell, such as flat sheets and 1D curves, accommodated our limited access to manufacturing facilities and aggressive production schedule. To construct the shell, $\frac{3}{16}$ " blind rivets were chosen as the primary method of attaching the aluminum sheets and ribs together. Blind rivets were chosen over nuts and bolts due to quick installation and the positive locking nature of rivets.

Strength

The aerodynamic shell must withstand the load imparted by 10g deceleration while having a minimum ultimate safety factor of 3. The chosen blind rivets can withstand 330lb of shear force and weigh only 0.0078lbs/rivet. To further strengthen the shell, a series of $\frac{1}{16}$ " ribs are attached and act as mounting points to the chassis.

Accessibility

To allow easy access to the pneumatic and electronic components, the aerodynamic shell must be easily removable. As such, a set of 8 latches are mounted on the sides of the front and back sections of the aerodynamic shell, while the middle section is screwed onto the L-beams.

3.3.4 Analysis

Sheet Metal

CFD was conducted to see the effects of air pressure on the aluminum sheet metal, specifically deformation.

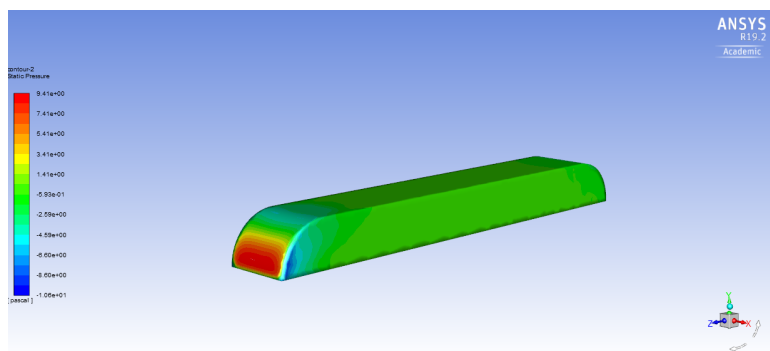


Figure 24: Pressure Profile of Aerodynamic Shell

Given that the yield strength of aluminum is 40 kPSI and the maximum stress experienced due to the air pressure is 0.0014 PSI (shown in Figure 24), the team has deemed that the aerodynamic shell will withstand the stress and experience minimal deformation.

Latches

The latches are capable of loads up to 130 lbf. The worst case scenario is when the latches have uneven fastening and only one latch is holding the aerodynamic shell to the chassis. Using $F = ma$, where m is the mass of the heaviest section of the shell, and a is 10g, the expected load, F , on one latch is 33.3 lbf. This gives a safety factor of 3.9.

CFD Analysis (ANSYS Fluent)

To measure a coefficient of drag of the aerodynamic shell, a CFD simulation was performed in ANSYS. See Supplemental Documentation for more detail on the method of the simulation. The results were as follows:

- Coefficient of Drag: 0.74
- Coefficient of Lift: 0.069
- Drag Force: 0.1lbf

$$F_{drag} = \frac{1}{2} C_d \rho V A \quad (2)$$

To analyze the total drag force of the entire pod, a simple calculation of each contributing element under the following approximations were performed:

1. Pressure: 0.125 PSI
2. Speed: 125 mph
3. Temperature: 77 degrees Fahrenheit
4. C_d was approximated using known C_d of similar geometries
5. Frontal Area is calculated by using the largest dimensions of the shape

Table 23: Total Drag Force per Contributing Element

Element	Number of Elements	Approx. Geometry	C_d	Effective Area (ft^2)	Total Contributed Drag Force (lbf)
Aerodynamic Shell	1	N/A	0.74	-	0.1
Front Cover	1	Flat Plate	1.00	0.53	0.175
Suspension	2	Flat Plate	1.00	1.02	0.336
Tanks	4	Long Cylinder	0.82	0.866	0.234
Total Drag Force					0.845

3.4 Lateral Stability System

3.4.1 Technical Description

A custom stability system is used to maintain the pod's position relative to the I-beam. The system mounts to the flange of the I-beam using two identical trucks connected by a strut. The stability system is also responsible for positioning the calipers of the braking system, and includes a plate to which the calipers are mounted. Several views of the stability system are shown in Figures 25a-26.



(a) Front view of a truck without brake mounting plate (b) Stability system truck isometric view with brake mounting plate

Figure 25: Two views of the lateral stability system



Figure 26: Side view of stability system and connecting struts

Our system uses high-speed bearings and polyurethane rollers to create a tight rolling fit with the I-beam. A linear bearing is used to connect the stability system to the chassis. This linear bearing allows the pod to move vertically in relation to the I-beam, and because the brake calipers are mounted to the stability system, the braking system is unaffected by any vertical motion.

The load carried by the stability system consists of two stability truck systems (4.0 lbs each), four brake calipers (2.1 lbs each), two mounting plates (1.75 lbs each), and two struts (2.1 lbs each), for a total load of 24.1 lbs.

3.4.2 Design Rationale

The lateral stability system must maintain proper pod alignment, adjust for I-beam misalignment, dampen developing vibrations, and provide a mounting point for the brake calipers.

To ensure the brake caliper and I-beam will not make contact before actuation, it is necessary to maintain an air gap of $\frac{1}{16}$ of an inch. The top and bottom rollers are in constant contact with the track, and therefore are used to define the position of the caliper brakes. Thus, making the stability system and braking system one unit provides a reliable reference for the braking calipers and ensures the calipers will not make contact with the I-beam prematurely.

We rely on the internal elasticity of the chosen roller materials to provide the corrective force necessary to dampen motion and correct the position of the braking calipers. Polyurethane 70A was selected for the top and bottom rollers because it is soft enough to initially deform in response to large discontinuities, which protects the pod from sudden jolts, but is also hard enough to rapidly correct the position of the brakes in response to small track discontinuities. A harder polyurethane, 90A, was selected for the side rollers because they must guide the mass of the entire pod rather than the stability and braking systems only. Furthermore, the effective width of the side wheels is limited to the thickness of the I-beam flange, which further necessitates the 90A material with a higher corrective force per inch width than the top and bottom rollers.

In order to transfer horizontal and lateral forces between the stability system and the chassis without transmitting vertical forces, the stability system is connected to the pod using a linear bearing. This bearing allows the stability system to maintain the precise position of the calipers while still transmitting in-plane forces such as braking and acceleration. The linear bearing was chosen for its simplicity and low-cost compared to other possible systems like linkage or rack-and-pinion systems.

The rollers, shafts, and linear bearing are the most critical components of the stability system, and are the components which directly carry loads. The rest of the assembly constitutes a $\frac{3}{8}$ " aluminum 6061 T6 casing which contains and supports the critical components. The thicker aluminum casing carries no direct loading; thus, the team was primarily concerned with analyzing the critical stability components and not the casing itself.

3.4.3 Safety

Our chassis has several failure modes, which the stability system is designed to counteract. One potential cause of failure is the brake pads contacting the track during propulsion. To prevent contact, the top roller must support the brake weight without compressing enough for the brake calipers to contact the I-beam, and the top roller central shaft must not experience significant deflection. Polyurethane 70A was

determined to provide adequate support without deforming excessively under the weight of the brakes, and steel was used for the central shaft. The analysis conducted demonstrates that the deformation and deflection are small enough to maintain the required $\frac{1}{16}$ " air gap.

We also investigated failures due to an over-rotation of the bearings. In the Performance Analysis section, we determine the maximum theoretical pod speed for our bearing rating, which exceeds our expected top speed by 50%.

Finally, we investigated the frictional forces between the I-beam and stability system to ensure that excessive friction is not generated during operation. Manual testing was conducted to determine frictional forces under loads both above and below our loading weight, and the data was curve-fit to estimate frictional force under the loading of our braking system weight. The frictional force was found to be very small, and should not hinder the acceleration of the pod.

3.4.4 Analysis

Linear Bearing Shaft

Analysis of the linear bearing is completed in Section 3.7.3.

Bearing Speed

The bearings are rated for a maximum rated speed of 32,000 RPM (533 rotations per second) when lubricated with a petroleum or synthetic oil. Because the stability system uses the same shielded bearings for all rotating components, the worst-case rotation scenario occurs on the bearing attached to the roller with the smallest circumference, this being the top roller with a circumference of 4.71". We calculate the maximum allowable pod speed the fastest-rotating bearing can handle by multiplying the smallest roller circumference by the maximum rated speed:

$$Top\ Speed = C * \omega = 4.71in * 533RPS = 2512in/s = 142.7mph \quad (3)$$

Therefore, our bearings are rated up to a maximum pod speed of 142.7 mph. Given our expected top pod speed of approximately 95 mph, the stability system has a safety factor of 1.50.

Roller Deformation and Shaft Deflection

It is critical to ensure the top roller and supporting shaft do not cause significant deflection under the loading of the braking system. The following analysis calculates expected deflections to ensure they are smaller than the designed air gap of $\frac{1}{16}$ ".

The governing equation for the top roller deformation distance is as follows:

$$U = \left(\frac{0.75Ps}{E\omega(8R)^{\frac{1}{2}}} \right)^{\frac{2}{3}} [in] \quad (4)$$

P is the load applied to the stability system from the brakes; since the total load of 24.1 lbs is divided between the two stability trucks, with each top roller supports 12.05 lbs. E is the elastic modulus of the 70A polyurethane, 0.77 ksi. The length of the top roller, w , is 4.75". R is the top roller external radius, 0.75", and s is the internal diameter, 0.5".

Calculating the maximum deformation of the top roller:

$$U = \left(\frac{0.75 * 12.05lbf * 0.5in}{770PSI * 4.75 * (8 * 0.75in)^{\frac{1}{2}}} \right)^{\frac{2}{3}} = 6.334 \times 10^{-3}in \quad (5)$$

Next, we will calculate the maximum deflection of the central top roller shaft. The governing equation for the shaft deflection is as follows:

$$\delta_{max} = \frac{PL^3}{384EI} [in] \quad (6)$$

Our moment of inertia for the solid cylindrical shaft cross-section is:

$$I = \frac{\pi}{4} R^4 = \frac{\pi}{4} (0.25in)^4 = 0.00307in^4 \quad (7)$$

The length of the shaft is 4.75", and the elastic modulus E is 2900 ksi. Therefore, the maximum deflection under the braking load P of 12.05 lbf is:

$$\delta_{max} = \frac{12.05lbf * (4.73in)^3}{384 * (2.9 \times 10^7 PSI) * 0.00307in^4} = 3.777 \times 10^{-5} \quad (8)$$

These results lead to a total deflection of 0.00637". This deflection is small, and is not enough to breach the $\frac{1}{16}$ " air gap and impinge on the I-beam.

Rolling Friction

We experimentally determined the rolling friction of the stability system under various loading conditions. Our experimental setup entailed joining the trucks with a wooden plank and placing weights on the plank to simulate pod weight. Then, a force sensor measured the force required to keep the trucks moving at an approximately constant speed under 5 loading conditions. Finally, we performed a linear regression on our data and interpolated the resulting line to find the frictional force for the weight of the braking system. The experimental results can be seen in Figure 27.

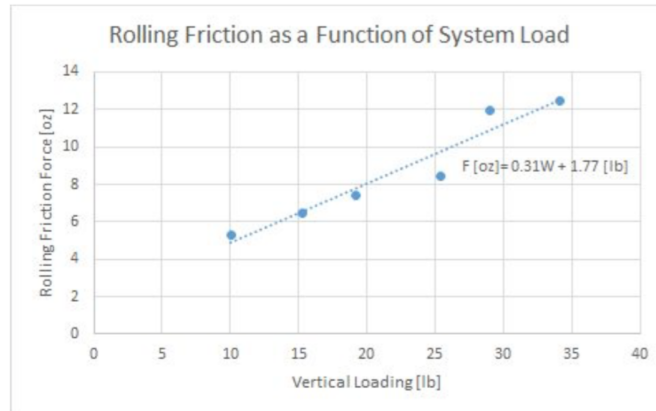


Figure 27: Experimental results of rolling friction test

Using the linear curve fit to find the frictional force when loaded with our braking weight of 24.1 lbs:

$$F[oz] = 0.31W[lbf] + 1.77 = 0.31(24.1) + 1.77 = 9.24[oz] = .578[lbf] \quad (9)$$

Using this method, we calculated a frictional force of 0.58 lbf for the stability system under weighted conditions. This frictional force is well within our expectations, and will not significantly hinder the 120 lbf propulsion from the tri-gas thrusters.

3.5 Suspension System

3.5.1 Technical Description

The suspension system on the pod is dual purpose. The suspension system both carries the weight of the pod, allowing for smooth movement along the test track, as well as providing motorized travel along the track while the propulsion system is not engaged. The motorized aspect of the suspension system is only engaged during initial operation of the pod to reach the track's first distance marker and to facilitate removal of the pod from the track after the pod's run is complete. As depicted in Figure 28, The suspension system is comprised of four identical modules, of which only the two modules located at the front of the pod are capable of providing propulsion via. electric motor. Attached to each module is a coilover which is used to absorb and dampen impact due to track imperfections.

Each suspension module is mounted to the chassis using an $\frac{1}{8}$ " aluminum chassis plate with rivets, fixed through ten rivet holes. The $\frac{1}{8}$ " aluminum side and top plates are attached to the chassis plate using six

steel brackets as well as steel bolts and locknuts. Each suspension module also consists of a polyurethane wheel that is friction fit to a steel shaft with retaining rings to prevent lateral motion. The steel shaft for each module is fixed to press fit ball bearings on the triangular suspension pivot brackets via. a friction fit with retaining rings on either side of each bearing. See Figure 28 for a visualization.

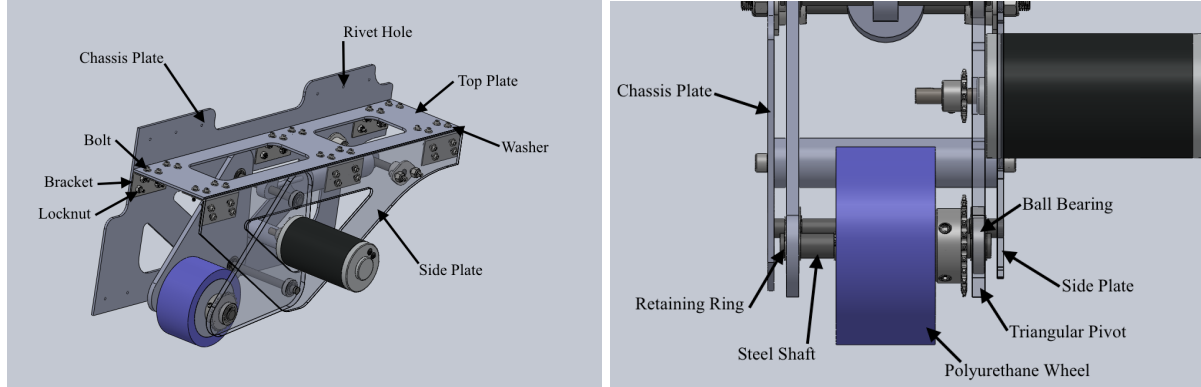


Figure 28: Isometric and Front View of the Suspension System

A coilover is used to absorb and dampen the shock forces the wheel experiences. One end of the coilover is fixed to the triangular fixture while the other end is attached to the chassis. A steel shaft is used to fix the coilover to both the chassis and triangular fixture plate. The fixture method for the coilover shaft attached to the triangular fixture plate is identical to the wheel shaft. The coilover shaft attached to the chassis is fixed using mounted bearings, bolts, and locknuts. See Figure 29 for a visualization.

The mechanical orientation of each suspension module allows any vertical displacement experienced by the wheel to translate into compression of the coilover. To prevent full compression of the coilover in the event of extreme shock, a stop bar is mounted between the chassis and side plates such that the triangular fixture plates will make contact with the stop bar before full compression of the coilover is reached, see Figure 29 for a visualization.

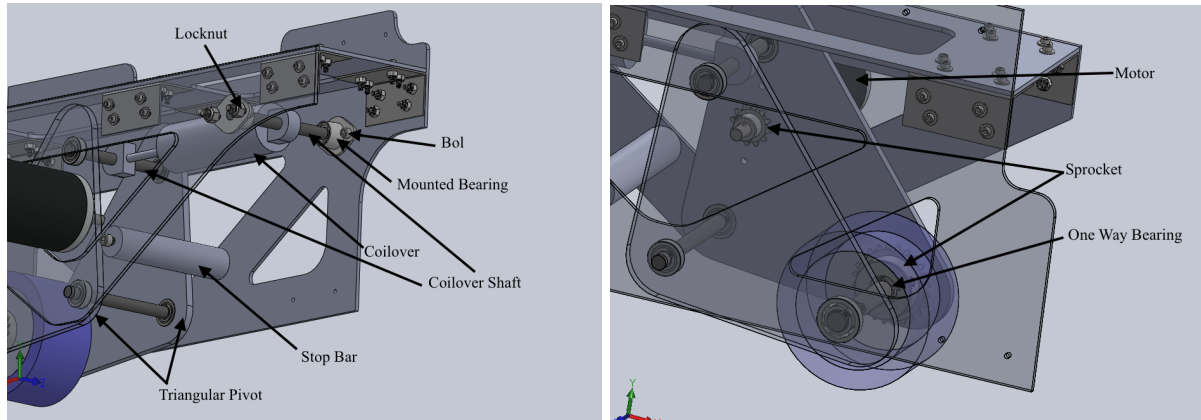


Figure 29: Rear and Side View of the Suspension System

As mentioned previously, two of the four suspension modules attached to the chassis are motorized as seen in Figure 29. Each motorized suspension module consists of an additional two sprockets connected by a chain. The two sprockets are in a gear ratio of $\approx 2 : 1$, the motor is mounted through the triangular pivot plate via friction fit bearings to allow power to be transferred to the wheels regardless of wheel elevation. In addition to the motor and sprockets, the motorized suspension modules include a one-way roller bearing attached to the sprocket located on the wheel axle, allowing for unpowered rotation of the motorized suspension modules.

3.5.2 Design Rationale

Design rationale of the system was influenced by trade studies and research into real world suspension systems. The design ultimately chosen was inspired by Washington Hyperloop's 2018 suspension, based on the single pivot linkage system. The final suspension system was designed to meet four objectives:

- *Ease of Manufacturing:* The system was designed such that many parts could be manufactured easily and with high precision using manufacturing methods available to the team. An example of this can be seen in the components highlighted in Figure 30, which are designed to be cut from $\frac{1}{8}$ " thick 6061 T6 aluminum by waterjet, greatly reducing production time and effort compared to machining parts individually.
- *Purchasable Components:* As many components as possible will be bought from industry suppliers, ensuring industry-level quality, thereby minimizing risk due to component failure. Complex precision parts such as: bearings, wheels, coilovers, motors, bolts, nuts, sprockets, chains, and retaining rings, will be bought along with standard shafts and brackets, adjusting them to our needs as necessary.
- *Strength and Safety:* Our system has been designed to comply with the required factor of safety of 2.0 for yield stress and 3.0 for ultimate stress. Due to the difficulties in predicting the exact loads experienced by the system in the event of a bump, the system has been designed with a factor of safety of 3.26 for all machined components and 2.7 for purchased components. This represents a worst case assumption for the bump scenario, to ensure system survival in the event of failure. The ANSYS simulations done on the system show a minimum yield strength safety factor of 3.26 for across all suspension components. Additional information on the system's structural integrity can be found in the analysis section.
- *Flexibility in Mounting:* Our design also allows for the re-positioning of the system along the length of the pod should such a change be necessary. As depicted in Figure 31, the system mounts on the side of the chassis with the use of rivets. As the geometry of the chassis remains the same along its length, there is flexibility in where the system is mounted along the chassis. This requirement was set to allow for some tolerance in C.G calculations, so that desired stability requirements could be met even in the event of discrepancy between estimated C.G and true C.G of the pod.

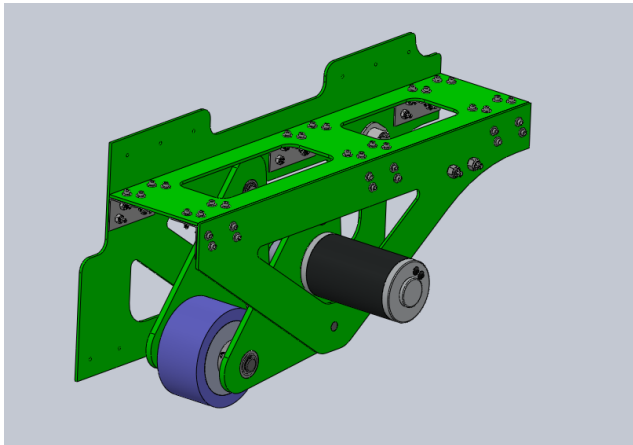


Figure 30: Water Jet Cut components (green)

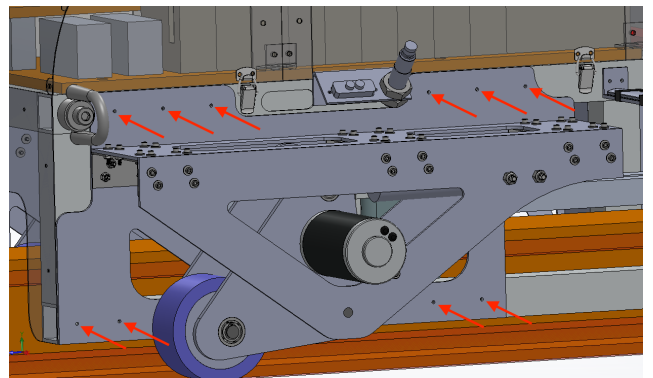


Figure 31: Suspension Mounting Points to Chassis

3.5.3 Design

From our design objectives for the suspension system, three design requirements were imposed. We wanted the suspension system to support the weight of the pod when encountering elevation discontinuities (ie. 'bumps') in the track. Secondly, we wanted the suspension system to be designed such that the change in pod elevation was minimized in the event a bump was encountered. Lastly, we wanted

the suspension system to enable motorized pod propulsion to facilitate pod removal after pod runtime. From these requirements, components were chosen to satisfy the design criteria. In the design, wheel bearings were chosen to support a max radial load of 310 lb statically, and 750 lb when in motion. Since the max load on a bearing in the system was found to be 196.22 lb and occurs during movement, the resulting in a safety factor of 3.8, in addition to loading requirements, the chosen wheel bearings meet the maximum speed requirements for each bearing which were found to be 10,500 rev/min with a given maximum speed of 25,500 rev/min.

Chosen wheels are rated for a maximum weight of 750 lb. With the max load on the wheel simulated in ANSYS being 277.5 lb, resulting in a safety factor of 2.7.

Mounted bearings fixed to the coilover's rear shaft support a maximum radial load of 600 lb when static. The load applied on the mounted bearings was found to be 69.38 lb, resulting in a safety factor of 8.6.

The coilover was chosen to have a spring rate of 750 lb/in, resulting in a maximum compression of 0.37 inches, well within the maximum compression of 2.16535 inches (55 mm) compared to the maximum of 0.37 inches.

For all other manufactured components, ANSYS simulations were run, ensuring a minimum yield strength safety factor of 3.26 above the minimum required safety factor of 2. The greater safety factor margin allows for greater tolerances for expected loads experienced by the suspension system. Design requirements were verified via. ANSYS analysis, which can be found in the supplemental documentation.

3.5.4 Analysis

This section will review the methods used to test the structural integrity of key system elements, pod behaviour under bump load, and predicted behaviour under motorized operation of the pod. For a more in depth explanation of the procedure and results of each analysis, see the supplemental documentation.

Suspension Bump Analysis:

To measure suspension performance on impact of subtrack joints (aka. 'bumps'), MATLAB models were created using worst case joint elevation and separation as outlined in the HyperLoop pod competition rules and regulations. In the bump analysis, Both wheel and pod elevation response to bumps can be seen in Figure 32, while force imparted by bumps can be seen in Figure 33. In both analyses, the maximum deflection of the wheels and pod respectively where found to be: 0.0057ft & 0.0056ft from nominal elevations. Maximum force induced by bumps on the wheel was found to be 171.23lb. From wheel manufacturers, maximum load capacity of wheels is estimated at 750lb [19], allowing for a safety factor of 4.38.

Suspension Structural Analysis:

To determine the structural integrity of the suspension system ANSYS simulations were performed to determine the structural viability of the wheel, the suspension joint and the suspension frame. For each simulation, the worst case equivalent loading experienced by one wheel was used, that being one fourth the pod weight along with the expected maximum loading due to subtrack bumps, adding up to a total of 277.5lb. Loading and boundary conditions for each ANSYS simulation were translated accordingly for the frame and suspension joint. Results for each simulation can be see in Table 24 and Figures 34-36.

Table 24: Structural Analysis Results of the Suspension System

Simulation	Max Deflection (in)	Max Stress (PSI)	YS (PSI)	SF	Material
Wheel	0.09854	13,000	45,000	3.46	1045 carbon steel
Pivot	0.0004	936	40,000	42.7	T6 6061 aluminum
Frame	0.012116	12,266	40,000	3.26	T6 6061 aluminum

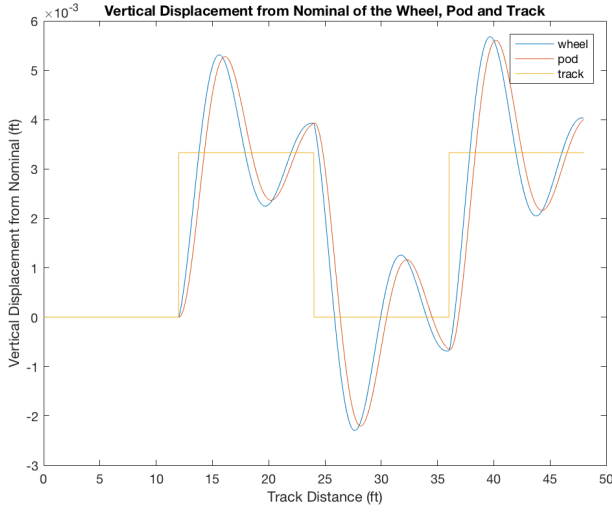


Figure 32: Nominal Vertical Displacement of the Wheel, Pod and Track

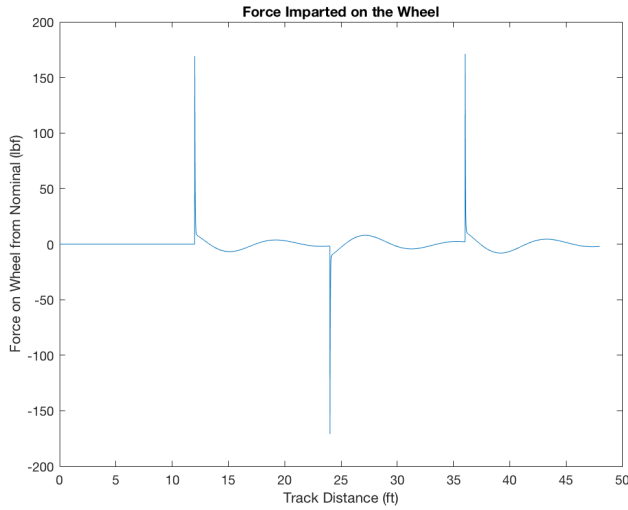


Figure 33: Force Imparted onto the Wheel from Nominal

Motorized Wheel Performance Analysis:

To measure the transient and steady state performance of the pod under motorized power, we performed an analysis using MATLAB to determine the velocity and distance to time profiles of the pod while motors were active. To accurately model the velocity and time curves, we approximate the total torque of the pod-motor system as a summation of the motor torque and frictional torque on each wheel. The final model can be seen in Equation 10 [17].

$$\tau_t = \tau_{stall}(1 - \frac{\omega}{\omega_f}) + \tau_f, \quad \tau = I\alpha = \vec{F} \times \vec{r}, \quad \alpha = \frac{d\omega}{dt} \quad (10)$$

Where in Equation 10 τ_t is the total torque on the wheel system, τ_f is frictional torque acting on the system, τ_{stall} is the stall torque on each motor and ω_f is freeload speed of the motor. The motors used are FR801-001 2.5in DC sim motors, with a stall torque and freeload speed of 343.4 oz-in and 5310 rpm respectively. Frictional torque in the system was assumed to arise solely due to rolling friction and resulted in a torque of 58.5 oz-in acting on each motor. The resulting ODE plugging all inputs to Equation 10 was then solved using a first order backwards finite difference with the initial boundary conditions of $\omega(0) = 0$ & $d(0) = 0$. Results can be seen in Figures 37 & 38.

In Figures 37 & 38 the point at which motor power is terminated and propulsion systems are engaged

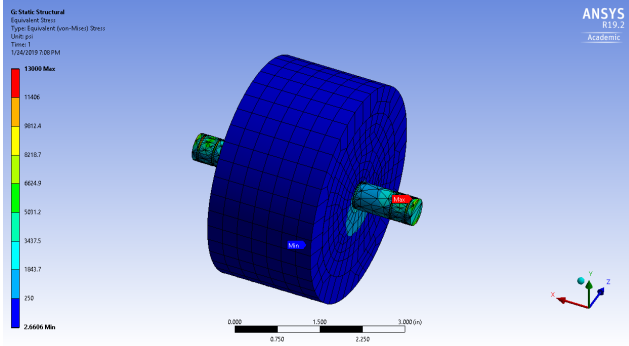


Figure 34: Stress on the Wheel and Shaft

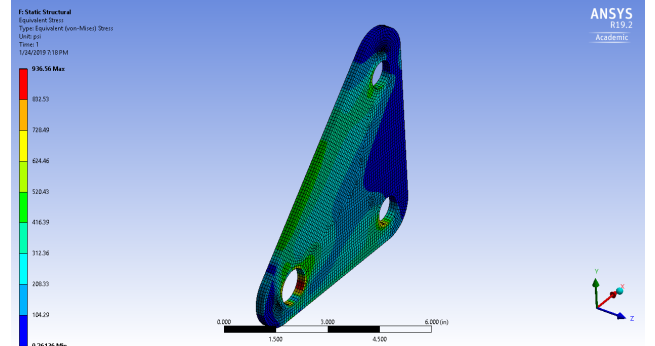


Figure 35: Stress on the Triangular Pivot

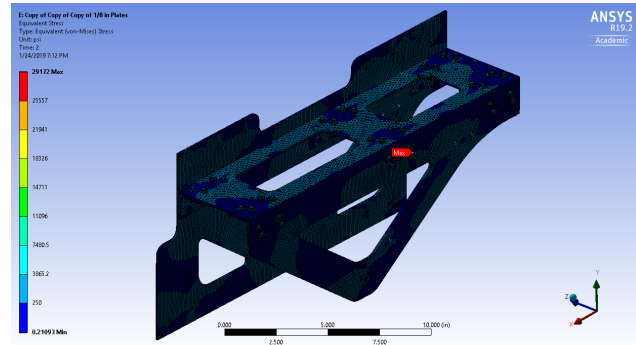


Figure 36: Stress on the Frame

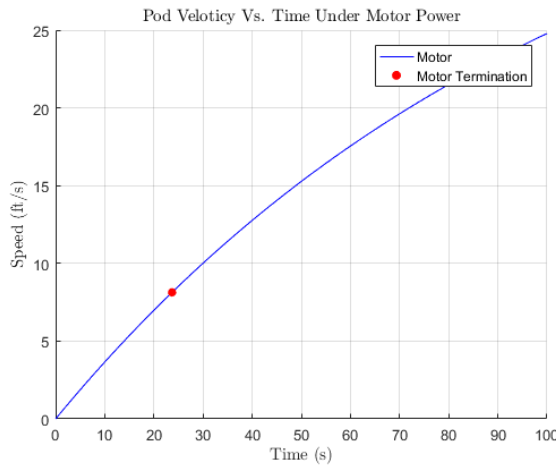


Figure 37: Transient Pod Velocity W. Motor Power

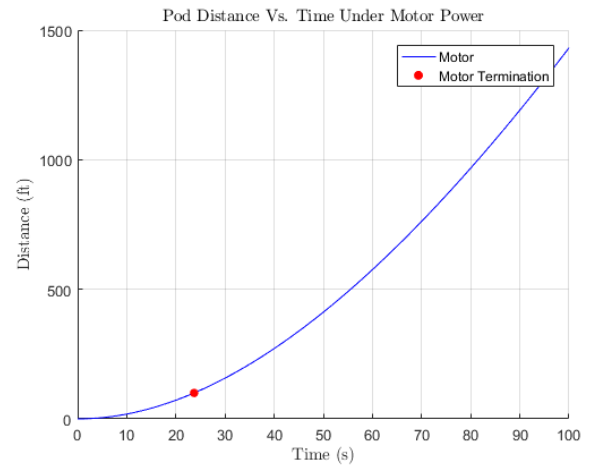


Figure 38: Transient Pod Distance W. Motor Power

during initial startup of the pod is marked in red. The time to the first marker at 100m under motor power is estimated to be 23.7s , with a velocity of: $8.1\text{ft/s} = 5.5\text{mph}$

3.6 Propulsion System

3.6.1 Technical Description

The 2019 OneLoop propulsion system consists of two tri-gas thrusters. “Tri-gas” refers to a modified cold gas thruster system that increases propulsive efficiency by reacting the gaseous propellant with a chemical catalyst prior to expansion through a nozzle. Tri-gas functions similarly to a resistojet, but utilizes chemical heating rather than electrical heating. As the name suggests, tri-gas propellant is a mixture of three gases: Hydrogen, Oxygen, and an inert carrier gas. The defining characteristic of a tri-gas system is that it contains a very high (>90%) concentration of inert gas and very low concentrations of Hydrogen and Oxygen, rendering the entire mixture non-detonable.

This propulsion system design is inspired by a research paper written by a team at Marshall Space Flight Center in 2014, titled *Tri-gas Thruster Performance Characterization* [6]. The purpose of the paper was to investigate “potential efficiency improvements from using tri-gas” and to “optimize thruster performance” for a tri-gas system. Several variables were tested, including catalyst types, catalyst lengths, and initial catalyst temperatures” [6]. In that study, a 5 lbf thruster was developed using Helium as the inert gas; for this year’s propulsion system, a much stronger thruster is designed using Nitrogen instead.

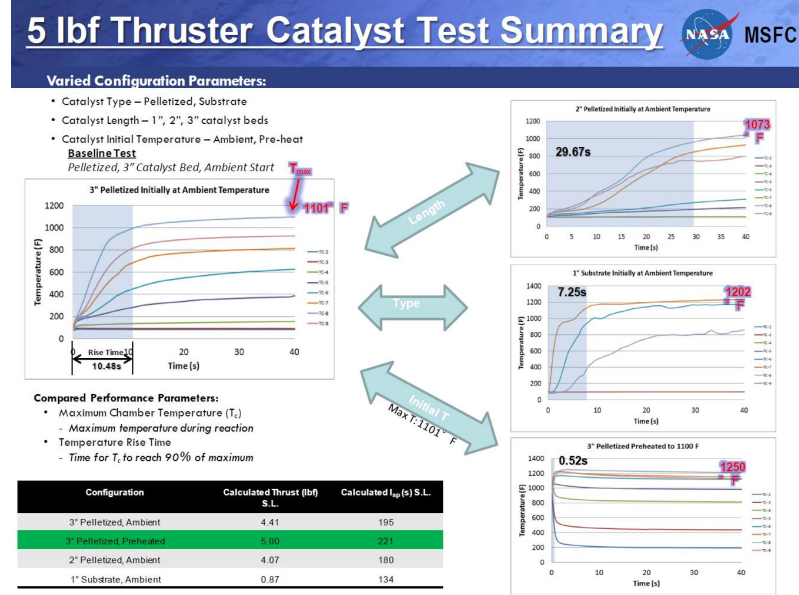


Figure 39: NASA tri-gas experimentation results. Conclusions: increasing catalyst bed length and preheating catalyst bed both significantly reduce rise time [6].

Breakdown

A breakdown diagram of our tri-gas system can be seen below. There are four primary systems located on the pod and two auxiliary systems located off the pod that will be used to prepare the pod for its competition run. Designs for the primary systems are included in this report, while designs for the auxiliary systems are located in the Supplemental Documentation.

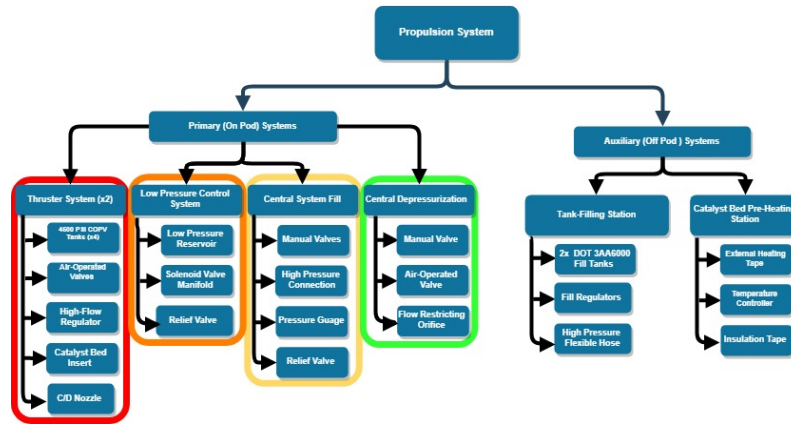


Figure 40: Propulsion system breakdown. Highlighted sections correspond to corresponding sections of the P&ID.

Components and P&ID

A comprehensive table of selected pneumatic components is included below, followed by the system P&ID. Relevant datasheets for selected components are included in a folder labeled “Datasheets” submitted with this report.

Table 25: Selected Pneumatic Components

Part Number	Component Type	Component
TA-1, TA-2, TA-3, TA-4	COPV High-Pressure Tank	IORMAN 4500 PSI 6.8 Liter tank
TA-5	Low Pressure Air Reservoir	Bimba Air Reservoir
S-1, S-2, S-3, S-4, S-5	Normally-Closed 3/2 Solenoid Valve	NITRA AVS-3111-120A
Q-1,Q-2	Non-Relieving Pressure Regulator	Aqua Environment 873-1500-H-L
A-1,A-2,A-3,A-4	Air Operated Valve	High Pressure Equipment Co. Mini-Hippo 30-11HF4 (Normally closed)
A-5	Air Operated Valve	Mini-Hippo 30-11HF4 (Normally open)
G-1	Pressure Gauge	Grainger 4FLV2
M-1, M-2, M-3, M-4 M-5, M-6, M-7, M-8	Manual Flow Control Ball Valve	Parker 4F-B6LJ2-SSP
M-9	Low Pressure Ball Valve	Parker VV500P
R-1	Relief Valve	Swagelok SS-RL3M4-F4
R-2	Relief Valve	Swagelok SS-4R3A5
O-1	Orifice	Aqua Environment 796

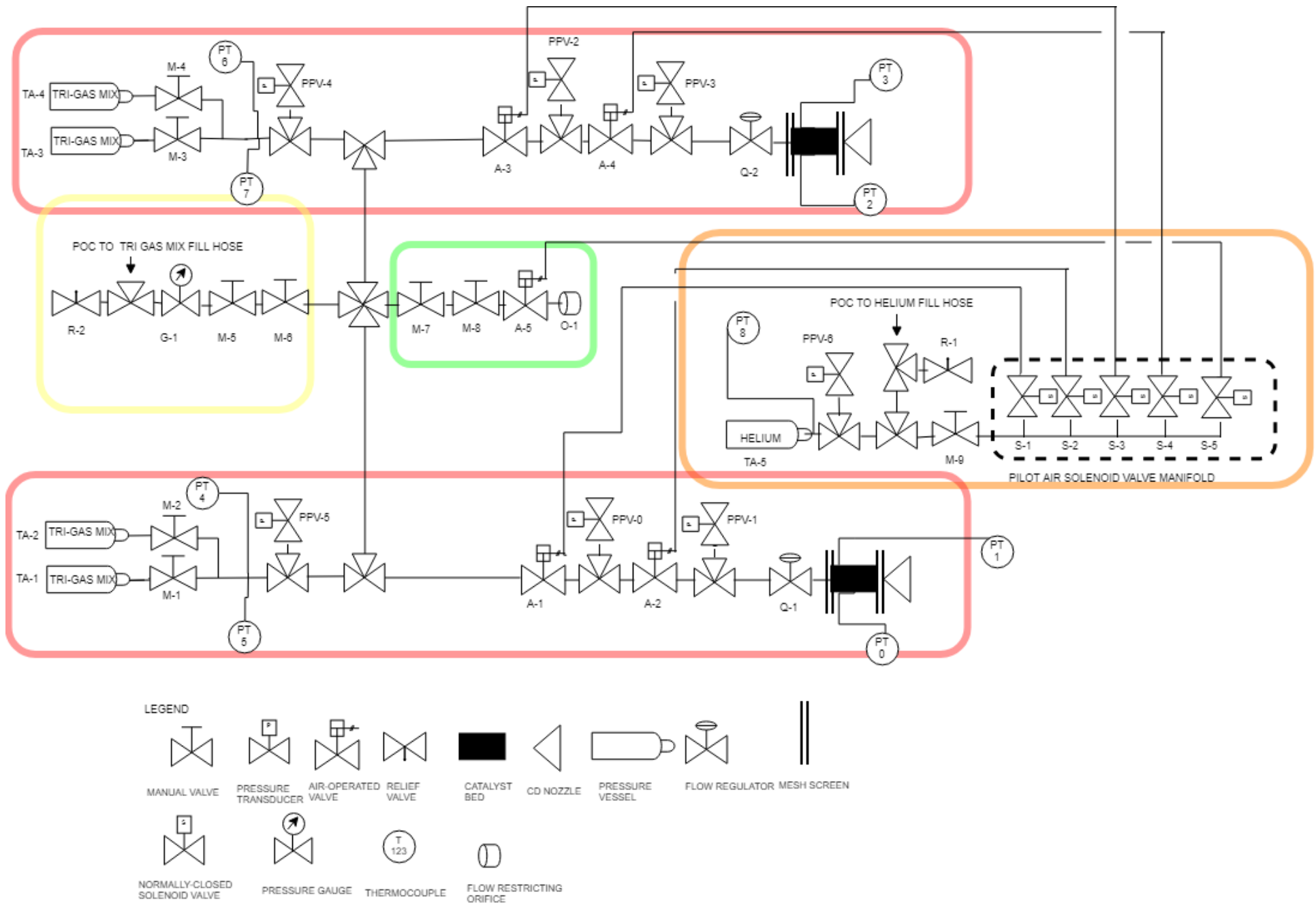


Figure 41: P&ID

3.6.2 Design Rationale

At the beginning of the year, an initial trade study was performed to determine what kind of propulsion system the team would pursue. Three candidate systems were identified based on last year's research as well as designs that were seen to be successful at the 2018 Hyperloop competition: cold gas thrusters, a clamped drive-wheel, and a linear induction motor (LIM). The results of that trade study are included in the Supplemental Documentation document.

To summarize the study, the cold gas system was found to be best suited to both the technical capabilities and high aspirations of this year's pod. More specifically, cold gas thrusters offer three key advantages over the alternative systems mentioned.

- *Small Electrical Power Requirement:* This year, our team is increasing focus on system safety and test readiness, so switching from a high-voltage, high power density LIM to a simpler pneumatic system is advantageous. Furthermore, members of the propulsion team have prior experience with high pressure system design, while only a handful of members on our entire team have experience with high-power voltage systems.
- *High Acceleration:* While LIMs may be more scalable to a real Hyperloop system (as evidenced by the dominance of LIM propulsion systems in the Hyperloop industry), they provide a relatively low initial acceleration. For this competition, there is not enough track to utilize the advantages of a LIM. A cold gas system, on the other hand, allows for a significantly faster release of stored energy, allowing for a larger initial acceleration and therefore a higher top speed within the tube.
- *Manufacturability:* Last year, the LIM proved to be difficult to manufacture. Because the team's second major focus this year is on testing and validation, it is advantageous to have an easy-to-manufacture system that allows for multiple, rapid design iterations. The only necessary manufacturable components are the nozzles. Our team has a strong manufacturing experience and access to a CNC lathe and mill.

While cold-gas thrusters were found to be most ideal, they are also known to be very inefficient due to the low chamber temperature of the propellant. This problem is compounded in the case of on-pod storage tanks, since rapid expansion from finite tanks results in the gas temperature falling rapidly over the course of the run.

Two potential methods of combating this inefficiency were identified. The first is to run the system without pressure regulation, since higher chamber pressures result in higher thrust. However, this method is extremely dangerous, as gas would be expelled at over 4000 PSI and could cause extreme injuries if mishandled. Furthermore, unregulated flow makes it difficult to design a consistent nozzle due to the changing inlet pressure profile. The other method to combat cold gas inefficiency is to heat the propellant gas prior to nozzle expansion. While this method is more complex than simply removing pressure regulation, it is much safer, as it allows for significantly lower chamber pressures and more flow control. In addition, it allows the nozzle to be designed for more optimal performance throughout the run, which increases the system efficiency, producing closer to constant thrust. Therefore, it was decided that heating the gas at the nozzle inlet is best option for this year's pod.

After preliminary investigation, it was determined that external heating tape or internal heating probes would require far too much on-pod power to effectively heat the cold gas, particularly because of the short time available for heating as the cold gas moves quickly through the pneumatic system before relief. Adding enough onboard power to heat the gas would negate one of the primary advantages of a cold gas system, which is power system reduction. Therefore, a simpler, faster method was needed. After discovering the NASA tri-gas paper and consulting with NASA Marshall Space center, catalytic heating was selected as the best option for the following reasons.

- *Safety:*
 - The main advantage of a tri-gas system is that the large concentration of inert gas keeps the mixture non-detonable [6]. This means that there are small enough concentrations of

Hydrogen and Oxygen that a combustion reaction does not spread throughout the mixture as the exothermic reaction takes place.

- Another safety advantage is the inverse relationship between tank pressure and pod-speed. This implies that as our pod goes faster, the total amount of stored energy on the pod decreases. This is especially important when considering a crashing scenario, since there will be little to no propellant left in the tank during any crash event. If there is still significant propellant in the tank, then little propulsion must have occurred, since the pneumatic system is the only source of meaningful thrust.

- *Simplicity:* Tri-gas systems are extremely similar in design to traditional cold gas systems, with the only difference being an added catalyst bed prior to nozzle expansion. Furthermore, this catalyst bed can be press-fit into the thrust chamber of the nozzle, adding very little complexity to the overall system [6].

- *Temperature:*

- *High Chamber Temperature:* In the NASA study, the tri-gas catalytic ignition raised the temperature of the exiting Helium up to 1200 °F. The study also hypothesized that a Nitrogen propellant system with the same gas ratios would experience temperatures up to 800 °F [6]. On the Kelvin scale, these temperatures are more than double what a cold gas propellant would experience.
- *Low Exit Temperature:* However, in the case of expanding to near vacuum, the gas undergoes a significant temperature drop. Using isentropic expansion calculations, the expected outlet gas temperature is 70 K, signifying no risk of overheating the subtrack. This will be discussed further in the thermal considerations section of this report.

- *Testability:* By maintaining system simplicity, the tri-gas propulsion system can be easily modified to a regular cold gas system just by switching to a different nozzle without catalysts. In other words, multiple nozzles can be designed for either cold gas or tri-gas applications, with minimal differences between them. This also allows for system testing to be done in a logical, “proof of concept” order. A purely cold gas system that runs on Nitrogen propellant can be tested first to verify thermodynamic model predictions and assist in the tri-gas nozzle design. This test would also test the pneumatic system safety before adding the catalyst bed and testing the hotter system. How to build up the testing procedure in this way is included in Section 7.1.5.

- *Rise Time:* One important conclusion from the experiments at NASA is the effect of pre-heating the catalyst bed before using the thrusters. When a 3 inch bed of pelletized catalysts was pre-heated to the expected maximum temperature, the “rise time” (time for propellant in chamber to reach 90% theoretical maximum) was significantly shorter. This can be seen in Figure 39. A short rise time is ideal to gain optimal performance as quickly as possible during the competition. Stored propellant tanks drop in temperature very quickly when rapidly expanding through a nozzle, so the early seconds of higher temperature are crucial.

3.6.3 Design

Component Selection

Propellant – 92% Nitrogen, 5.33% Hydrogen, 2.67% Oxygen

This graphic shows that the mixture is non-flammable at STP as long as the Nitrogen concentration is above 90% [15]. Furthermore, NASA Safety Standards state that the mixture cannot ignite at a pressure of 0.125 PSI, and its flammability will remain low during scheduled or emergency relief [15]. For more information on system flammability safety, see Section 6.4 of this report.

Catalyst – Research Catalysts Puri-Star R20-47 Palladium

In the NASA tri-gas study, pelletized catalysts were found to perform better under the structural loads

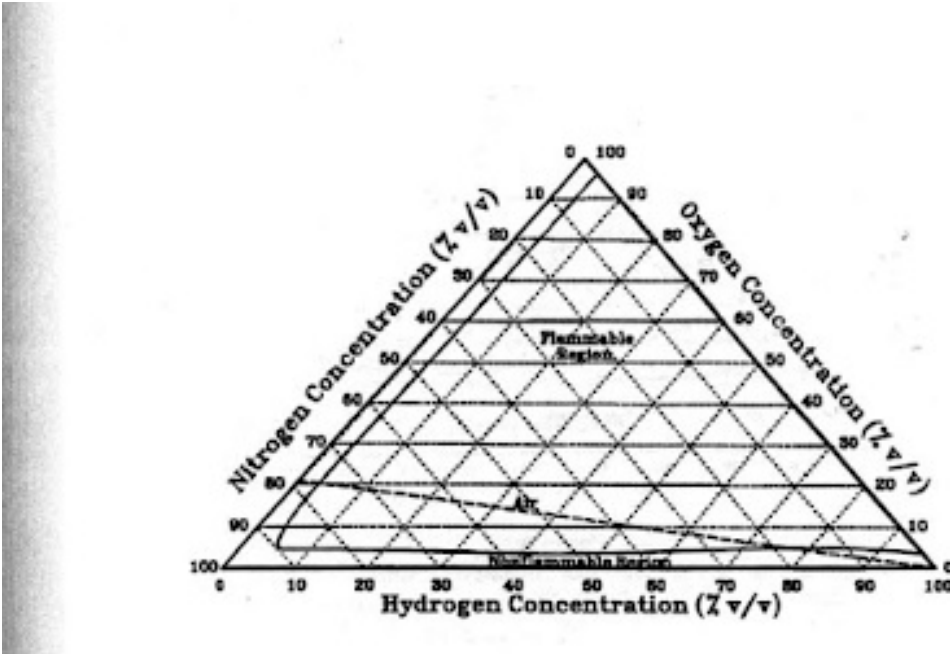


Figure 42: Flammability Triangle for Hydrogen Oxygen mixtures at STP [15].

caused by the pressure drop across the packed bed; the R20-47 type catalyst is comprised of small, 1/8" diameter pellets. The maximum pressure drop across the bed for our system is 29 PSI, as determined by the thermodynamic model detailed in Section 3.2 of this report. According to the catalyst datasheet, the pellets' yield strength for crushing is 11 lbf. This corresponds to a safety factor of 31 for the compressive strength of the catalyst pellets.

These catalysts were selected based on their low cost and non-reactivity with air. Platinum-Iridium based catalysts would require high-temperature baking prior to use in order to remove oxidation from their surface. A Palladium catalyst does not require this treatment, which is ideal for performance and preparation during the competition.

A critical calculation for the application of this catalyst is its temperature increase, shown below.

The energy balance equation of the adiabatic reaction is

$$\text{Heat released by formation of H}_2\text{O} = \text{Heat absorbed by H}_2\text{O and N}_2$$

From this equation, the heat of formation for 5.33 moles of H₂O at 298 K is 1289760 J. Using the integrated H₂O Cp value from the NASA experiment (17243.58 J/mol), the heat absorbed by the H₂O could be calculated [6]. This value is 91960 J. As a result, ΔQ was calculated to be (1289760 J - 91960 J), equal to 11977800 J. ΔT of the N₂ gas for the ΔQ above was calculated to be 446 K. Adding this to the initial gas' temperature of approximately 298 K, the maximum temperature of the catalyst is 744 K.

Tanks – IORMAN 4500 PSI, 6.8 Liter cylinders (Empty Bottle) (x4)

The IORMAN 4500 PSI offers many advantages:

- *Lightweight Material*: These COPV tanks weight just 3.8 kg per unit.
- *High Pressure*: The tanks are rated for up to 4500 PSI, which was considered high enough for this application when considered along with storage volume.
- *Safety*: These tanks are DOT certified, which is displayed on their labels. Furthermore, they have a hydrostatic test pressure rating of 7,300 PSI, satisfying the 1.5 x working pressure requirement.



Figure 43: Selected Carbon Fiber Cylinder Labels.

- *Cost:* These tanks are sold as empty bottles, which is ideal since we need them filled with tri-gas. This also lowers the cost of tanks significantly. Furthermore, since the cylinders do not come with pre-installed valves, we are not technically replacing any components by attaching the tanks directly to our thruster and fill systems.

Pressure Regulator – AE 873-1500-H-L

The thruster system flow regulator is selected based on the following considerations:

- *High Flow:* This regulator can provide a maximum flow rate of 440 SCFM for our outlet pressure setting.
- *Inlet Pressure Rating:* The selected regulator is rated for an inlet working pressure 6000 PSI and has been hydrostatically tested to four times its working pressure in accordance with ASME Vessel Code Section 8. Since we will be using an inlet pressure of 4500 PSI, this corresponds to a safety factor of 5.33.
- *Outlet Pressure Range:* The selected regulator can output 0 -1500 PSI.
- *Cost:* Two AE 873-1500-H-L regulators would typically cost around \$1500. However, our generous sponsor Aqua Environment donated two brand new regulators along with a 796 flow restrictor.
- *Temperature Considerations:* The selected regulator uses a low-temperature, Nitrale O-ring that can withstand -60 °F. Furthermore, this model comes with a body-heating manifold that can be used to prevent component freezing during testing and decrease the risk of damaging the component.

Air-Operated Valves – High Pressure Equipment Co. Mini-Hippo 30-11HF4 (Normally closed)

Four different criteria were considered when selecting the control valves for this system:

- *Speed:* The selected control valve type should have a sufficient opening torque for faster valve opening/closing.
- *MAWP:* The selected control valve type must be rated for a max pressure 1.5 times greater than the anticipated maximum working pressure (4500 PSI).
- *MADP:* The selected control valve must be rated for a maximum differential pressure 2 times greater than the highest differential pressure seen (4500 PSI).
- *High Flow:* Although pressure is downregulated upstream, the type of control valve selected should have a high Cv as to mitigate the pressure drop across the control portion of the system before entering the flow regulator.

From these criteria, a decision matrix was created comparing different types of pneumatic control.

Table 26: Flow Control Trade Study

	Weight (5 = High Importance)	Dual Burst Disk Assembly	Solenoid Valve	Air-Operated Valve
Speed	4	4	2	3
Reliability	4	5	3	5
Safety	5	2	5	2
Low Cost	3	4	1	3
Reusability	3	1	4	4
Total Points		61	60	63

From the results shown above, valves A-1, A-2, A-3, and A-4 will be normally-closed air operated valves.

The force acting on any closed air operated valve for the max pressure scenario (4500 PSI) was found to be 176 lbf. Using 90 PSI pilot helium, the specific air operated valve chosen was calculated to apply 240 lbf. This is a sufficient pressure of pilot air to properly open a specific air operated valve.

The *Falcon 9 User’s Guide* published by SpaceX states that “additional precautions are required for operating systems that are considered hazardous, such as redundant valving between pressurant and propellant.” Redundancy is needed in this scenario but to what degree? Thus, an interesting trade-off is created between increased redundancy of air operated valves and the subsequent total cost for all the air operated valves. The closest estimate for the failure probability of an air operated valve was found to be (for the 2” to 3.99” valve size range which is much larger than what will be used) very conservatively, 0.089 [5]. The effects of added redundancy of these air operated valves on the total cost per thruster system is shown below.

Each AOV failure is assumed to be independent and as such, the probability of multiple valves failing can be found by finding the intersection probability of n valve failures.

Table 27: Redundancy Trade Off Costs

Proposed control valve redundancy per thruster	Corresponding number of control valves needed per thruster	Probability of total thruster control failure	Cost increase from the n base case per thruster
n (no redundancy)	1	0.089000	+\$0
$n+1$	2	0.007921	+\$254
$2n$	2	0.007921	+\$254
$2n+1$	3	0.000705	+\$762

From the above, it can be seen that an increase from $2n$ to $2n+1$ redundancy does not warrant a 2x cost increase. $2n/n+1$ redundancy is sufficient for this application as there is a failure rate of less than 1 percent. Our initial design shown previously incorporated $2n$ redundancy (A-2 redundant to A-1, A-4 redundant to A-3); This study validates that design decision.

Based on these requirements and considerations, the Mini-Hippo 30-11HF4 (Normally closed) from High

Pressure Equipment Co. is selected for all air-operated valves.

Relief Valves - Swagelok SS-RL3M4-F4 and SS-4R3A5

Relief valves R-1 and R-2 must be sized properly for safe function of this high pressure system. A table summarizing the relief valve pressure specifications are below. These pressures were calculated using page 4 of the API 520 document posted by SpaceX.

Table 28: Relief Valve Pressure Specifications

	R-1	R-2
Max Allowable Working Pressure	250 PSIG	4500 PSIG
Design Pressure	110 PSIG	4500 PSIG
Max Set Pressure (105% of MAWP)	263 PSIG	4725 PSIG
Max Over Pressure (103 % of MAWP)	258 PSIG	4635 PSIG

Subsequently, the necessary orifice area of the relief valve can be calculated with the equation below.

$$A = \frac{W}{CK_d P_1 K_b} \sqrt{\frac{T \times z}{M}}$$

The variables used to calculate this area for each relief valve are shown below.

Table 29: Variable Values For Orifice Area Equation

	R-2	R-1
W (kg/s)	0.069	0.0012
K_d	0.975	0.975
K_b	1	1
P₁ (Pa) = (1.1* P_{MAWP})	4.56*10 ⁷	1.99*10 ⁶
T (K)	300	300
Z	~1.1	~1.0
M (kg/mol)	0.02674	0.004
C (s·K^{1/2}·mol^{1/2} / kg^{1/2}·m)	0.0336	0.0289

Since in both relief valve scenarios the percentage of backflow is less than 40%, K_b=1 can be used. The resulting area and diameter values are below.

Table 30: Calculated Orifice Areas And Diameters

	R-2	R-1
A (m ²)	6.8*10 ⁻⁶	5.8*10 ⁻⁶
d (in)	0.1164	0.1074

Moreover, subsequent selections are below.

Table 31: Selected Orifice Components And Diameters

	R-2	R-1
Component	Swagelok SS-4R3A5 relief valve	Swagelok SS-RL3M4-F4 relief valve
d (in)	0.125	0.125

Piping, Threads, and Connections - Stainless Steel, $\frac{1}{4}$ inch and $\frac{1}{2}$ inch NPT

The pipe chosen for this system must satisfy three criteria:

1. Allow for a gas velocity through the pipe of Mach 0.3 or less
2. Have a maximum working pressure with a factor of safety 2x greater than the pressure the pipe will see (4500, 550 PSI)
3. For the half inch case (which interfaces with combustion chamber), must be capable of withstanding extreme temperatures (up to 900 °F)

Half-inch NPT stainless steel pipe satisfies the three criteria for the 550 PSI case. As such, it is the chosen pipe for the plumbing that is downstream of the regulator. For plumbing that is upstream of the regulator, quarter-inch stainless steel NPT satisfies the necessary requirements. Both pipes will have a 0.049" wall thickness. The characteristics of these pipings are shown below.

Table 32: Stainless Steel Pipe Characteristics [1]

Nominal Size	Worst Case Scenario Pressure (PSI)	Maximum Allowable Working Pressure (PSI)
1/4"	4500	7500
1/2"	550	3700

Due to the nature of the NPT interference fit, it is not practical to estimate the friction coefficient or the torque specification of the connections. As a result, a “turns from finger tight (TFFT)” approach will be used for connections. Two to three additional turns will be done following a finger tight connection [1].

Thermodynamic Model

To design a nozzle and characterize the performance of this system, the state properties of the propellant must be estimated for any time during operation. To this end, a thermodynamic model was developed in Python based on a system of ODEs derived from the Redlich-Kwong equation of state and the First Law of Thermodynamics. This model is for a single tri-gas thruster, and is built upon a model created by Sarah Nothnagel for the design of a TALARIS Nitrogen cold-gas lunar hopper [12]. Her model, in turn, is based on a paper written by Professor Alessandro Golkar [8].

The core of the model is the system of ODEs shown below, which are directly derived from the First Law of Thermodynamics and the Redlich Kwong Equation of State, as detailed in Reference [8].

$$P = \frac{\partial P}{\partial T} \dot{T} + \frac{\partial P}{\partial V_m} \dot{V}_m = A \dot{T} + B \quad (11)$$

$$A = \frac{\partial P}{\partial T} = \frac{R}{V_m - b} + \frac{1}{2} \frac{a}{T^{3/2} V_m (V_m + b)} \quad (12)$$

$$B = \frac{\partial P}{\partial V_m} \dot{V}_m = \left\{ -\frac{RT}{(V_m - b)^2} + \frac{a(2V_m + b)}{\sqrt{T[V_m(V_m + b)]^2}} \right\} \left(\frac{-VM}{m^2} \right) \dot{m} \quad (13)$$

$$\dot{T} = \frac{1}{\left(\frac{\partial h}{\partial P} - \frac{V}{m}\right)A + \frac{\partial h}{\partial T}} \left\{ \frac{1}{m} \left[\dot{Q} + \dot{m} \left(2h - \frac{PV}{m} \right) \right] - \frac{PV}{m^2} \dot{m} - \left(\frac{\partial h}{\partial P} - \frac{V}{m} \right) B \right\} \quad (14)$$

Table 33: Nomenclature For The System Of ODEs

a,b	Redlich Kwong Equation Constants
V_m	Molar Volume
R	Universal Gas Constant
m	Mass
V	Volume
P	Pressure
T	Temperature
h	Enthalpy
\dot{Q}	Heat Transfer

An attempt was made to recreate this model to simulate thermodynamic changes for our system. A working version could not be finished in time for this report.

However, it was discovered that the propulsion system designed for the TALARIS project is similar to our own propulsion system. The main aspects of the TALARIS system and our tri-gas system are listed below to show their similarities [12].

1. The TALARIS system tanks started with 4.14 kg of pure Nitrogen gas; our system tanks for a single thruster contain 4.10 kg of tri-gas, which is 92% Nitrogen.
2. Both the TALARIS tanks and our system tanks start at an initial pressure of 4500 PSI.
3. Both the TALARIS tanks and our system tanks start at an initial temperature of 300 K.

The model developed by Professor Golkar is designed to track the mass, temperature, and pressure of the gas in the storage cylinders over time given a mass flow rate and initial tank conditions. As shown above, our initial conditions for mass, pressure, and temperature are the same as the conditions in Ms. Nothnagel's completed model. Furthermore, by setting our regulator to an outlet pressure of 550 PSI, our system has a mass flow rate of approximately 0.24 kg/s, which is identical to the average mass flow rate of the TALARIS system [12].

Based on the similarity of the systems, the baseline pressure and temperature curves for the TALARIS are curve fit as seen in Figure 44 and used as starting points to create a modified thermodynamic model that can be used for our system.

Our model starts with these curve fits and adjusts the temperature and pressure curves from the TALARIS model based on flow, pressure, and temperature considerations specific to the components selected for our system.

Flow Considerations

Flow rates for the AE 873-1500 HL regulator for various inlet and outlet pressures are documented in Figure 45. For this system, the regulator's outlet set pressure is chosen to be 550 PSI. This pressure was selected as a compromise between high flow (better performance) and system safety, as well as its similarity to the TALARIS system value (for accuracy of results). As seen in the chart, with a set outlet pressure of 550 PSI, the regulator can provide a maximum flow of 440 SCFM (allowing for a 10% reduction in outlet pressure) as long as the inlet pressure is above 1200 PSI. Once the pressure falls below that

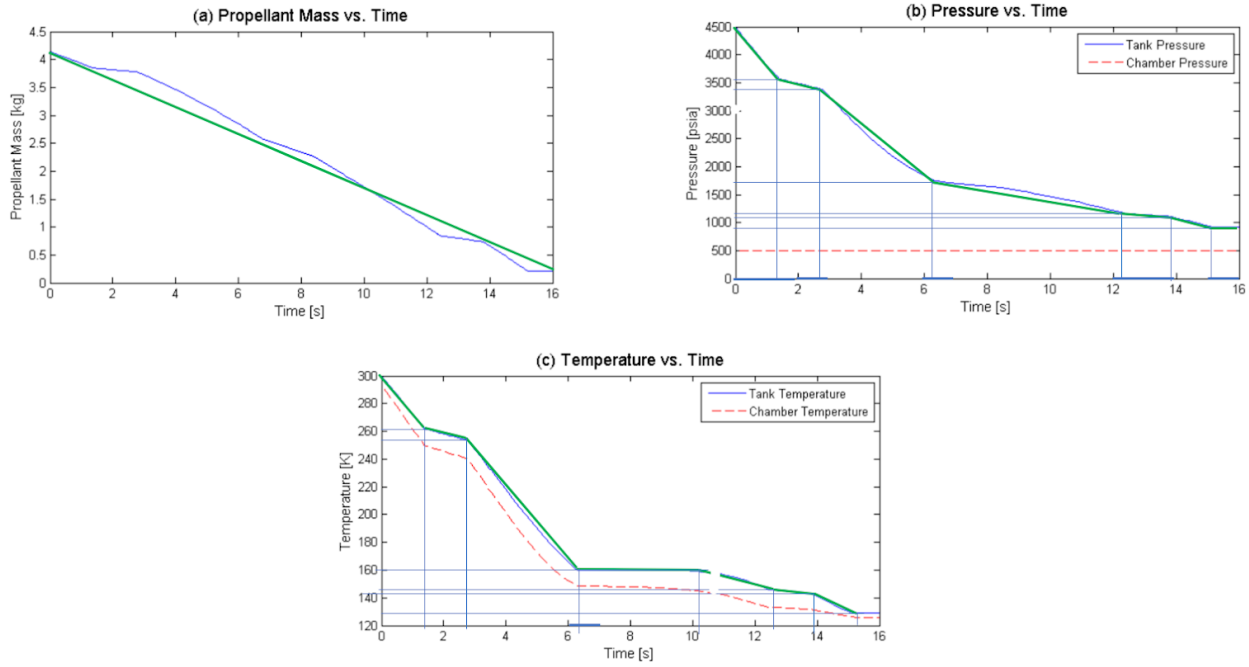


Figure 44: Piecewise curve fits of TALARIS model [12].

point, the flow switches from outlet-restricted to inlet-restricted, and flow rate drops. This information, along with the shape of the inlet curves as they travel down the y-axis, is used to create a curve-fit equation to characterize flow rate as a function of inlet pressure once it drops below 1200 PSI, which is displayed in Figure 46. The full flowchart document is included in the Data sheets file submitted along with this report.

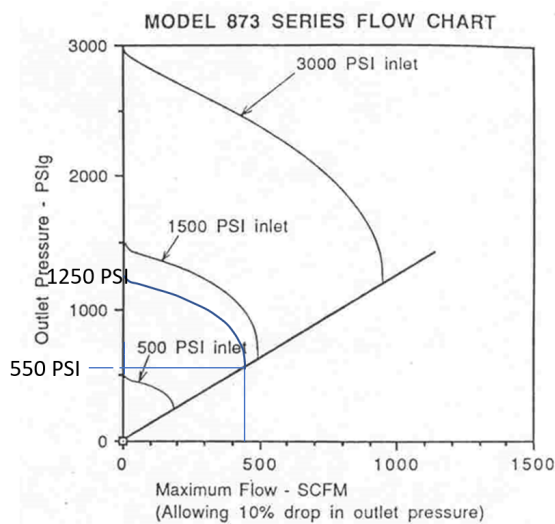


Figure 45: 873-1500 HL flow chart

Pressure Considerations

To determine the chamber pressure, two pressure drops are characterized between the regulator set pressure (550 PSI) and the thrust chamber. The first pressure drop is the “droop” seen by the regulator as a function of the mass flow rate. According to the regulator specifications, this droop results in a 10% loss of outlet pressure at maximum flow rate and just a 3% loss in outlet pressure at half maximum flow rate. Since no other information is provided, the droop is assumed to have a linear dependence on flow rate between these two values. The second pressure drop occurs across the catalyst bed. This drop is calculated in the model at each time step using the Ergun Equation, shown below [6]. The value for ϵ ,

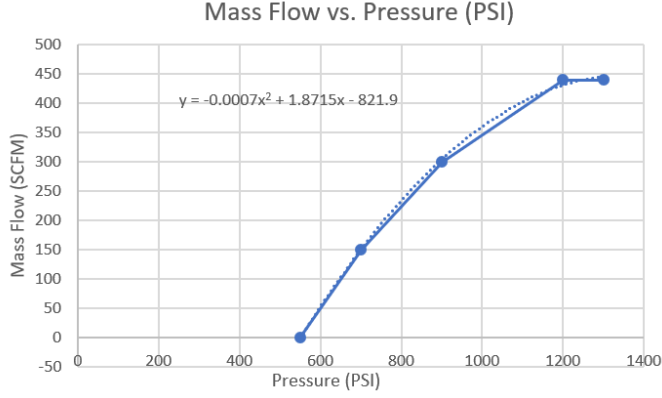


Figure 46: Curve fit of 873-1500 HL pressure dependence

the void space factor, is assumed to be the same as charcoal: 0.41.

$$\frac{\Delta P}{L} = \frac{150\mu V}{gD^2} \frac{(1-\epsilon^2)}{\epsilon^3} + \frac{1.75\rho V^2}{gD} \frac{(1-\epsilon)}{\epsilon^3} \quad (15)$$

Table 34: Nomenclature For Ergun Equation

Pressure	Length	Viscosity	Volume	Particle Diameter	Void Space Factor	Density
P	L	μ	V	D	ϵ	ρ

Temperature Considerations

Similarly, two temperature drops occur in the system due to isenthalpic throttling through both the regulator and catalyst bed. These drops are dependent on the Joule-Thomson coefficient of the propellant, which changes based on temperature and pressure. To obtain these coefficient values, .csv files were created and populated by writing a data-scraping script to access the NIST Chemistry Webbook and record values for density and the Joule-Thomson coefficient [11]. Because the Webbook does not contain data on our tri-gas mixture, all state values recorded are for Nitrogen gas only. However, because so much of the mixture is Nitrogen, this should have a small impact on the results. The properties were sampled from 3.4 to 34 MPa with a resolution of 0.051 MPa and from 140 K to 310 K with a resolution of 0.01 K. This fine of a resolution allows for accurate determination of the needed values, improving model accuracy. The chamber temperature, T_C , is determined using those Joule-Thomson coefficients from the .csv file and solving the equation shown below for both the regulator and catalyst bed at every time step [8].

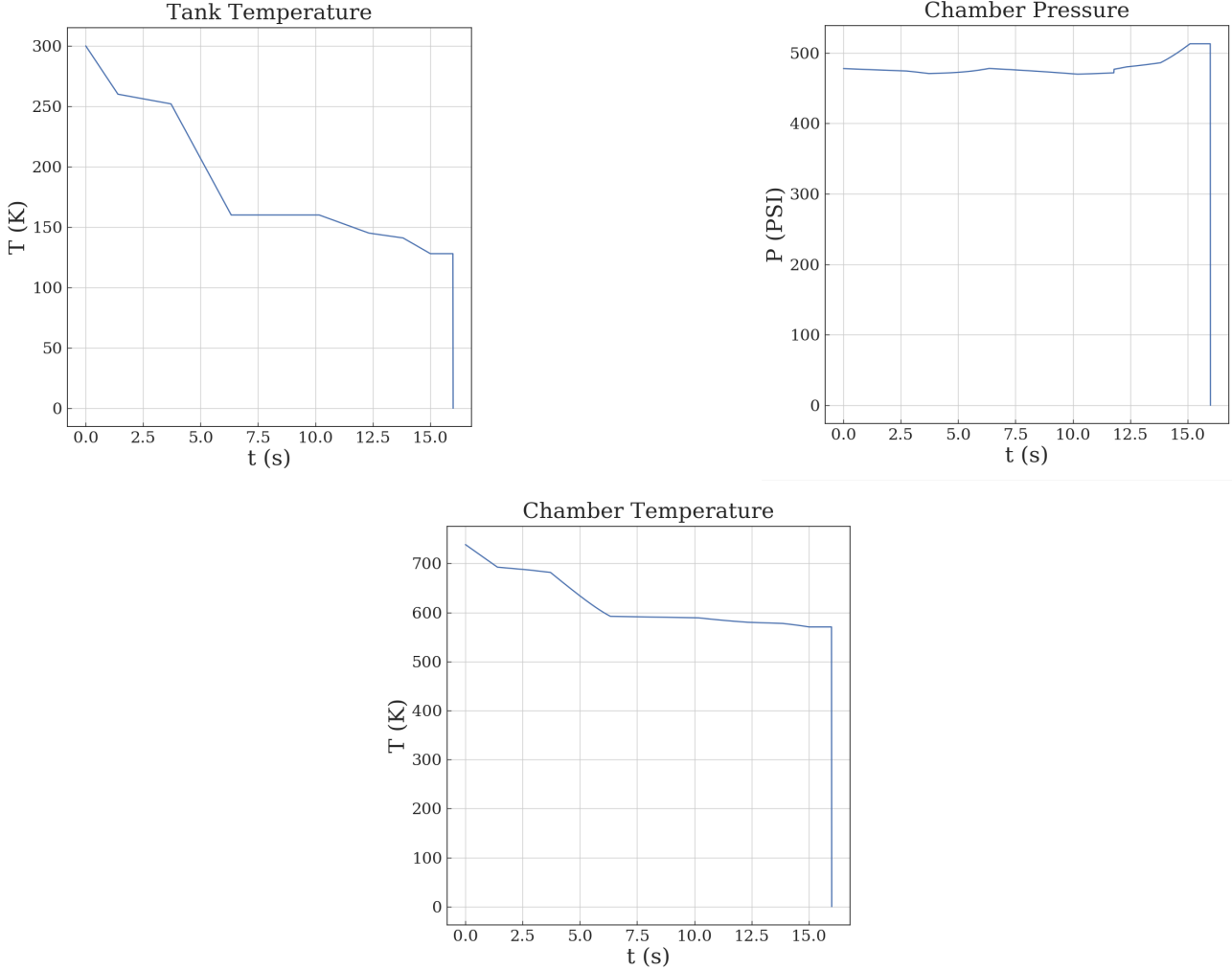
$$T_C = T_{tank} - \mu_\pi(P_{tank} - P_1) \quad (16)$$

To account for the temperature increase through the catalyst bed, the chamber temperature is increased by 445 K throughout the duration of the run, since the calculations for temperature increase are on a per-mole basis and should remain constant.

Thermodynamic Model Results

These flow, temperature, and pressure considerations specific to our system were used to adjust the TALARIS results in a python script, which is included in the Supplemental Documentation. Tank and chamber property results from the thermodynamic model are shown in Figure 47 over a 16 second runtime. These results are used to inform the design of the converging-diverging nozzle.

Figure 47: Thermodynamic Model Results



Nozzle Design

For this system, an optimum nozzle (exit pressure = 0.125 PSI) is designed following methods outlined in the eighth edition of Rocket Propulsion Elements by Sutton and Biblarz [7]. The nozzle material is chosen to be 304 stainless steel, as it has good strength properties at high temperatures, with a service temperature of 1200 K [7]. Furthermore, this is the material that was used in the tri-gas characterization paper, which subjected the nozzle to similar pressures and higher temperatures.

Throat Area

The nozzle throat area can only be designed for one chamber temperature and chamber pressure set. Therefore, it is necessary to establish the operation conditions for which the nozzle is designed. The equation below shows the relationship between choked flow and chamber temperature/pressure.

$$\dot{m} = \frac{A_t v_t}{V_t} = A_t P_1 k \frac{\sqrt{[2/(k+1)]^{(k+1)/(k-1)}}}{\sqrt{k R T_1}} \quad (17)$$

As seen in Figure 47, the chamber pressure, p_1 , does not change very much throughout the run. The chamber temperature, however, does change significantly throughout the run. Because there is an inverse relationship between choked flow rate and temperature, it is logical to time the maximum flow to occur at the lowest temperature. While choked flow increases during the run, the system is limited by nozzle throat area. However, once the tank pressure falls below 1250 PSI, the system becomes limited by the regulator as its maximum flow rapidly decreases (See Figure 46). The initial choked flow rate of the system is found to be 0.221 kg/s by plugging in the initial tank temperature and pressure values from Figure 47 into Equation 17. Because the initial choked flow only differs from maximum system flow by

0.022 kg/s, a linear flow curve over the pod runtime is assumed. This allows the mass flow over time to be modeled as seen below. If a working model was obtained, this mass flow rate would then be used to resolve the system; since the average flow rate is lower than in the first iteration, this would result in a longer useful thrust time before the flow rate falls off. However, using this flow profile with the original temperature and pressure curves can be considered a worst-case scenario, since the tank pressures and temperatures are lower than the real flow profile would predict. Design will proceed for this worst-case scenario.

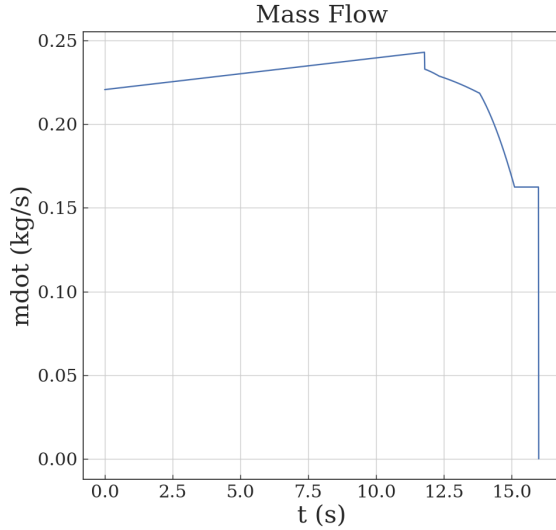


Figure 48: Mass flow over time. During the first 12 seconds, the flow is restricted by the nozzle, and choked flow slowly increases as temperature drops. For the last 4 seconds, the flow is restricted by the regulator's inlet pressure.

To ensure choked flow during the first 12 seconds of the run, the nozzle throat is sized for conditions that occur right as inlet regulator pressure falls below 1250 PSI. Using these conditions in Equation 17, the design throat area is found to be 0.0724 in^2 .

Exit Area and Chamber Area

After determining the throat area, Equation 18 is used to determine the exit mach number for our system, and Equation 19 is used to determine the optimal expansion area ratio.

$$p_0 = p [1 + \frac{1}{2}(k - 1)M^2]^{k/(k-1)} \quad (18)$$

$$\frac{A_2}{A_t} = \frac{1}{M_2} \left[\frac{1 + [(k - 1)/2]M_2^2}{(k + 1)/2} \right]^{(k+1)/2(k-1)} \quad (19)$$

According to these equations, optimum expansion mach number for an inlet pressure of 473 PSI and an outlet pressure of 0.125 PSI is found to be 6.9; the appropriate expansion area ratio for this exit mach number is found to be 98. Therefore, the nozzle exit area is found to be 6.30 in^2 . A contraction ratio for the system is chosen as 15, since a contraction ratio greater than 4 minimizes pressure drop through the thrust chamber and increases efficiency [7]. Therefore, the chamber area is calculated to be 1.09 in^2 . It is important to note that this chamber area is actually the internal area of the catalyst bed insert, which is press fit into to the nozzle chamber.

Nozzle Contour

The contour of the nozzle is designed as a 66% length bell contour based on a cone half angle of 15 degrees. The shape of the diverging section was approximated as a parabola that runs through both endpoints of the exit plane and both endpoints of the throat plane, as suggested by the Sutton and Biblarz text [7]. The chamber length is designed such that the catalyst bed insert can contain three inches of packed bed material. If testing finds that the chamber temperature does not reach expected

maximum values, this length can be increased to increase reactivity and decrease rise time. Lastly, the contour is widened in the chamber to account for the catalyst bed insert that will be press fit into the nozzle. The final nozzle contour is shown below along with its critical dimensions.

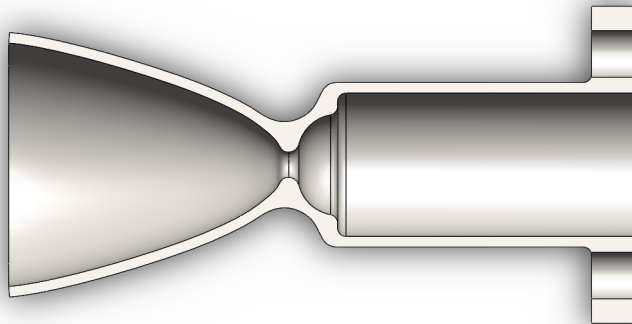


Figure 49: Nozzle cross-section to show contour (66% bell contour via parabolic approximation)

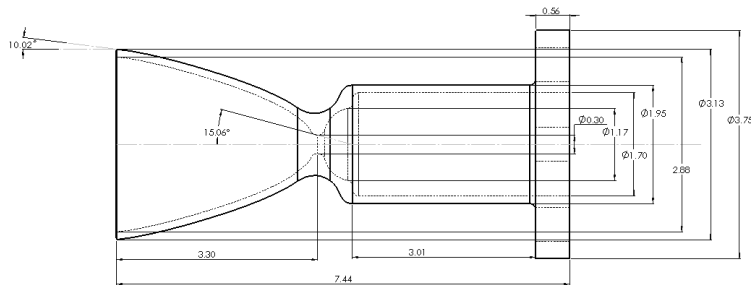


Figure 50: Critical Nozzle Dimensions

Wall Thickness

Material properties of stainless 304 at elevated temperatures are displayed below.

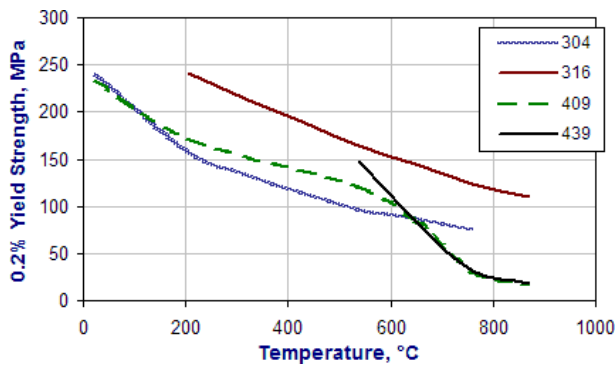


Figure 51: Yield Strength of stainless 304 at elevated temperatures [10].

Based on the curve for 304, the yield strength of the nozzle material is 100 MPa (15400 PSI) at a temperature of 745 K. The minimum wall thickness necessary to contain the chamber pressure with a safety factor of 2 can be found using the hoop stress equation, shown below.

$$YS/2 = PD/2t_w \quad (20)$$

However, our nozzle design also involves press-fitting the catalyst bed insert into the thrust chamber at a fitting pressure of 4 MPa (580 PSI), as seen in Figure 51. Assuming a worst case scenario in which the outer wall thickness would need to contain both the maximum chamber pressure (550 PSI without losses) and the press-fit insert pressure, the minimal wall thickness is calculated thusly:

$$t_w = YS/(P_c D_c + P_{bed} D_{bed}) = 15400/((550)(1.17) + (580)(1.70)) = 0.1123 \text{ in} \quad (21)$$

Based on this calculation, a wall thickness of 1/8th inch was chosen, as displayed in Figure 50.

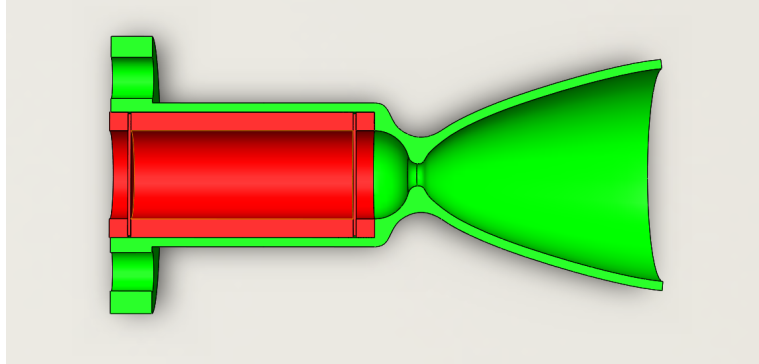


Figure 52: Section view of catalyst bed insert interfacing with nozzle

Nozzle Manufacturing and Test Nozzles

Our team is currently working with the campus machine shop, the Engineering Student Design Center, to create a process plan for the machining of this nozzle. In fact, the shop has granted us permission to use a 5-axis, DMG Mori-Seiki CNC Lathe to perfect our nozzle design. We are being very careful about this step, as the thinness of the wall and the complex internal geometries could cause vibrations in the part that would ruin the machining process or hurt the machine. Therefore, to master the tooling process plan prior to attempting it with stainless steel, test nozzles will be manufactured from 6061 aluminum instead, which was sponsored by the ESDC and is much more machine-friendly.

Furthermore, these test nozzles will be designed for atmospheric pressure rather than for vacuum, with an exit mach number of 2.91 and an expansion ratio of 3.9 according to Equations 18 and 19. Our team is also investigating variable throat inserts for our test nozzles to allow for more rapid prototyping with less manufacturing costs. For information regarding how these test nozzles will be used to optimize our system, refer to Section 7.1.5.

Performance Analysis (Thrust Profile)

Thrust is calculated for the system using the following equation. Because the nozzle is designed for optimum expansion, the pressure thrust term is ignored [7].

$$F = mv_2 + (p_2 - p_3)A_2 \quad (22)$$

As previously mentioned, the mass flow through the entire system will be limited by the nozzle during the majority of the run time. During this phase, the flow is choked, resulting in a supersonic expansion and meaningful thrust. The mass flow rate during this time is given by the equation below [7].

$$\dot{m} = \frac{A_t v_t}{V_t} = A_t p_1 k \frac{\sqrt{[2/(k+1)]^{(k+1)/(k-1)}}}{\sqrt{kRT_1}} \quad (23)$$

The Nozzle exit velocity during this time can be calculated using the following equation, which is dependent on the specific heat ratio, chamber temperature, and pressure ratio of the system:

$$v_2 = \sqrt{\frac{2k}{k-1} RT_1 \left[1 - \left(\frac{p_2}{p_1} \right)^{(k-1)/k} \right]} \quad (24)$$

Once the tank pressure falls below 1250 PSI, however, the flow becomes restricted by the regulator, resulting in lower, non-choked flow rates and very insignificant thrust since the flow remains sonic. Sonic flow thrust is estimated to be rapidly decreasing and proportional to the ratio between the actual mass flow rate and the required flow rate for choking.

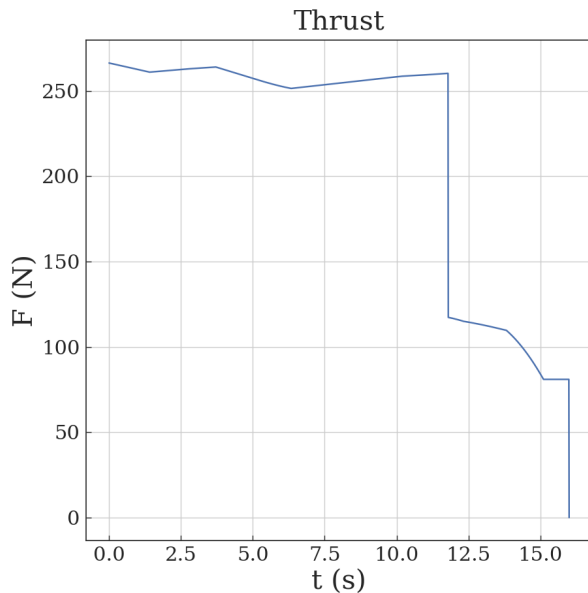


Figure 53: Simulated thrust profile

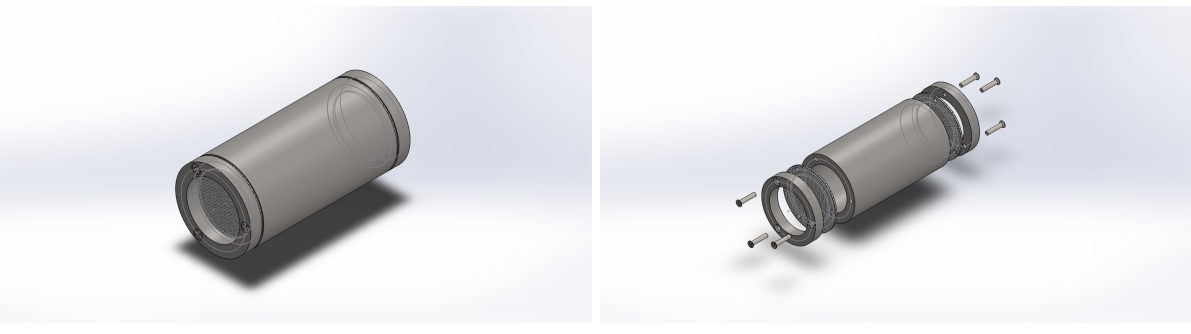
Using these equation, the thrust profile is calculated and plotted as seen in the figure below.

Average thrust per nozzle during the meaningful acceleration phase is 267 N; total average thrust over the 16 second runtime is 218 N per nozzle.

3.7 Catalyst Bed

3.7.1 Technical Description

The catalyst bed inserts into the thrust chamber of the tri-gas system nozzle and holds Palladium beads used to heat the gas prior to expansion.



(a) Integrated view of the catalyst bed

(b) Exploded view of the catalyst bed

Figure 54: Model of the catalyst bed

3.7.2 Design Rationale

In designing the catalyst bed, the engineering design parameters were the main body's inner area and length. The inner area of the chamber is 1.075 in^2 , and the length is 3".

A Stainless Steel 304 hollow cylinder forms the main body and containment chamber, which is pressure fit into the entry region of the tri-gas thrust chamber. Across either open end of the body cylinder is a 12x12" T304 Stainless Steel mesh, used to allow flow through the body while containing Palladium beads. A Stainless Steel 304 endcap is bolted to either end using #3 304 Stainless Steel machine screws to attach the mesh to the body and to evenly distribute stresses about the outer edge of the mesh. One

end cap is manufactured slightly smaller than the body for ease of removal after the unit is pressure fit.

Stainless Steel 304 was selected for the body and endcaps for its chemical stability, and because it is the material used for the surrounding thrust chamber. 304 Stainless Steel was also selected for the bolts and mesh due to its chemical stability, strength, and heat tolerance.

3.7.3 Analysis

SolidWorks Simulation analysis is performed on the catalyst bed in the steady state loading condition. According to our propulsion team's thermodynamic model, the maximal loading condition is a 501 PSI upstream pressure load and a 472 PSI downstream pressure load, resulting in a 29 PSI drop across the bed.

Figure 55 contains the stress analysis of the catalyst bed in the steady state loading condition. The maximum stress occurs in the center of the upstream mesh and has a magnitude of 52.16 ksi, corresponding to a factor of safety of 1.45. The maximum stress experienced by the downstream mesh is 46.19 ksi, corresponding to a factor of safety of 1.49.

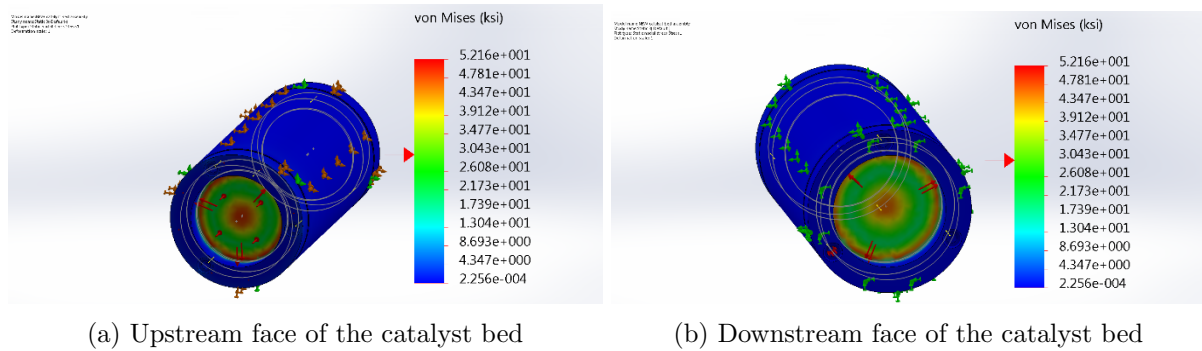


Figure 55: Stress analysis of the catalyst bed in steady state conditions

In both loading cases, the main body, caps, and bolts experience no significant stresses due to the pressure gradients. Therefore, because we are operating within their temperature ranges, it is reasonable to assume these components will function as expected.

3.8 Braking System

3.8.1 Technical Description

Our pod will include two independent pneumatic caliper friction braking systems. For each system, an air tank will supply pressure to pneumatic calipers controlled by two parallel, normally-open valves for redundancy. The pneumatic calipers mount symmetrically on the flange of the I-beam and will actuate to induce braking force. Each system is able to brake within our allotted distance in the case of a failure in another system. One of our independent systems is diagrammed in the figure below.

This system has a fill valve that can be accessed by opening BV-3, once the tank has reached the desired pressure the relief valve will start to release excess air. During the tank pressurization process, the tank pressure and temperature can be monitored by BTC-0 and BPT-4. Once the tank has been pressurized BV-3 can be closed and BV-1 can be opened.

A pressure regulator will be used to maintain the desired pressure for the brake calipers, which induce a force that is linearly related to the pressure they receive.

BPT-0 and BPT-1 are used to measure the pressure downstream of the regulator to ensure the pressure has been set accurately during pre-launch checks and monitor that there is no pressure loss during pod operation. The two parallel, normally-open valves are used to ensure the brakes actuate if the pod loses power. BPT-2 and BPT-3 ensure that the brake calipers are at the proper pressure and that the

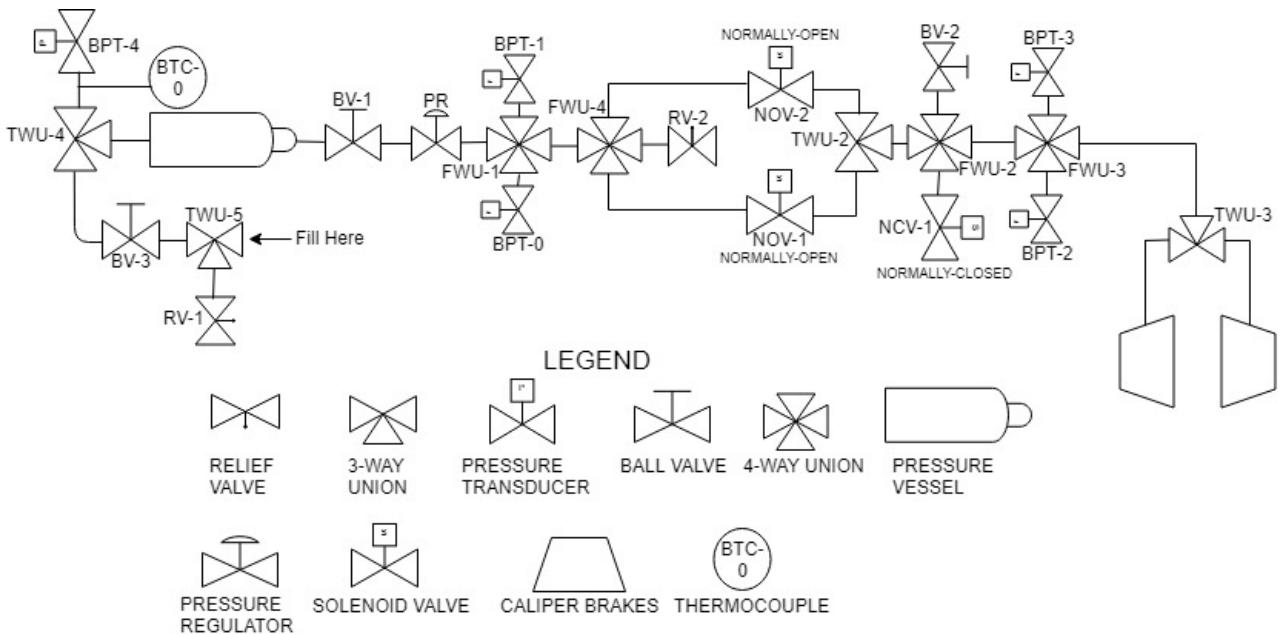


Figure 56: Braking System Diagram

valves are in the open position. Relief valve RV-2 is located after the pressure regulator to ensure that downstream components never experience pressure greater than their maximum working pressure specifications.

A flexible steel pipe will be used to connect the pneumatics located on the chassis to the calipers located on the stability system assembly. This allows the stability and braking systems to move freely, independent of the chassis, without causing piping geometry concerns.

In situations where the system must be opened, such as following brake caliper actuation or system failure, normally closed solenoid valve NCV-1 and ball valve BV-2 will be opened.

Finally, the brake calipers are mounted to the stability system which maintains tight tolerances with the I-beam, ensuring that the calipers don't contact the I-beam when not in use. Pictures of the caliper brakes and their mounting plate are given in Figure 57.

The specific components in this system are given in the Brakes Bill of Materials. Our system will use $\frac{1}{4}$ " inch NPT piping and ports whenever possible. Each component is rated to withstand at least 130 PSI; the tubing is rated to 1200 PSI, much higher than the required 1.5x MAWP for proof testing. In addition to these components, male to female adapters will be purchased as needed.

Table 35: Brakes Bill of Materials

Part Type	Quantity	Weight (lbm)	Material	Max Working Pressure (PSI)	Port Size (NPT)
Air Reservoir	2	4	Aluminum	250	1/2"
Ball Valve	6	1.2	Brass	300	1/4"
Fill Valve	2	0.2	Aluminum	250	1/4"
Relief Valve	2	.6	Brass	125	1/4"
Relief Valve	2	.26	Brass	200	1/4"
Pressure Gauge	2	.8	Stainless Steel	250	1/8"
Solid-State Pressure Sensor	10	4	Stainless Steel	200	1/4"
Thermocouple	2	1.5	Brass	250	1/4"

Table 35: Brakes Bill of Materials

Part Type	Quantity	Weight (lbm)	Material	Max Working Pressure (PSI)	Port Size (NPT)
Pressure Regulator	2	0.8	Aluminum	300	1/8"
Normally Open Solenoid Valve	4	4.8	Brass	130	1/4"
Normally Closed Solenoid Valve	2	2.4	Brass	200	1/4"
Pneumatic Caliper Brakes	4	8.4	Aluminum	200	1/8"
Friction Brake Pad	8	0.8	Organic Compound	N/A	N/A
Three Way Union Fitting	10	1.2	Brass	800	1/4"
Four Way Union Fitting	6	0.9	Brass	1000	1/4"
Aluminum Piping	1	2.9	Aluminum	150	1/4"
Stainless Steel Piping	1	2	Stainless Steel	1000	1/4"
Stainless Flexible Piping	4	2	Stainless Steel	2500	1/4"
Mounting Plate	2	3.5	6061 Aluminum	N/A	N/A

The total weight for the entire brake system is 43.5 lbs.

3.8.2 Design Rationale

Our pneumatically actuated caliper brakes were chosen primarily based on maximum braking force, reliability, and ease of design. The mechanical components of the caliper brakes are manufactured to withstand working pressures of up to 200 PSI, and all of the pneumatic components can withstand working pressures of up to 130 PSI. Our working pressure after pressure regulation is 100 PSI which gives an additional 1.3 safety factor to the system on top of the factory test safety factors.

For our air tanks, we utilize Bimba air reservoirs that will be pressurized to 200 PSI. This pressure, when combined with the internal volume of 27.5in^3 , can provide 55in^3 at our 100 PSI working pressure. We have determined this to be sufficient based on the internal volumes of our piping and valves.

During the design process, the caliper brakes chosen for the PDR were found to not be compatible with brake pads that have a lower hardness than the I-beam. A new caliper brake was found from W.C. Branham, which has brake pads that have a lower hardness than aluminum based on feedback from their design engineers. These new calipers also allow for a fully pneumatic system. Switching from a hybrid pneumatic-hydraulic system to a purely pneumatic system allowed our design to be greatly simplified.

The normally-open valves which control the flow to our calipers were chosen to ensure brake operation in the case of power loss. We also chose to have two parallel valves in order to ensure one valve failure could not cause a total subsystem failure.

3.8.3 Analysis

Our caliper brakes are designed to provide a braking force of $6.41 \frac{N}{PSI}$. For nominal scenarios, both braking systems (primary and redundant) will brake at a pressure of 100 PSI to produce a braking force of 1281 N. It is assumed that all propellant is consumed during the acceleration phase resulting in total mass of 332 lbs (150.6 kg), 18 lbs lighter than the initial mass. For our pod this results in a deceleration

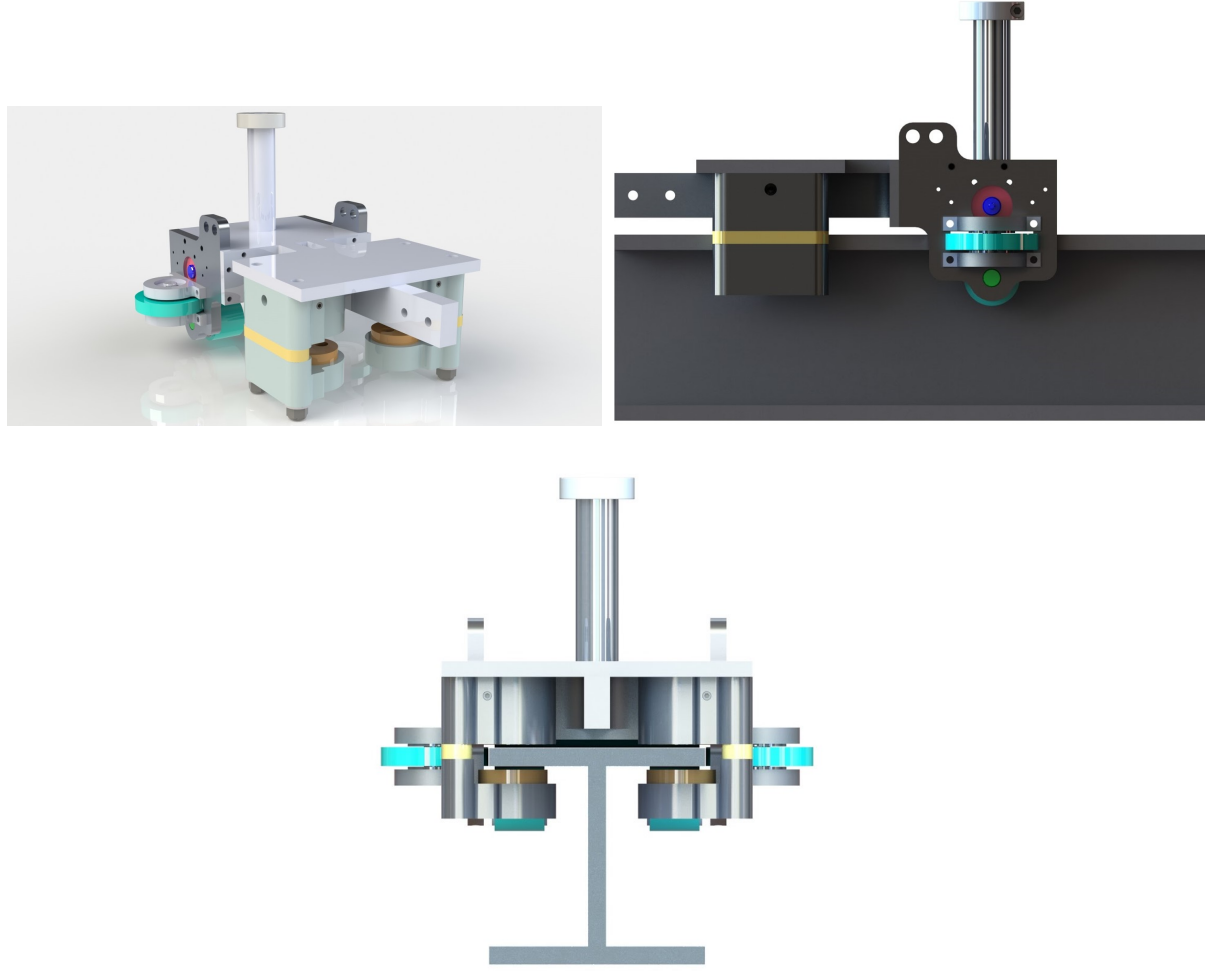


Figure 57: Isometric, Side, and Front Views of Braking Mounting Plate and Calipers

of $8.51 \frac{m}{s^2}$. With this deceleration, we can completely stop the pod from our theoretical maximum speed of $42.1 \frac{m}{s}$ in 104m. These results are based off the following guiding equations:

$$\begin{aligned} F &= m * a \\ 1281N &= 150.6kg * a \\ a &= 8.51 \frac{m}{s^2} \end{aligned}$$

$$\begin{aligned} v(t) &= -a * t + v(0) \\ 0 &= -(8.51 \frac{m}{s^2}) * t + (42.1 \frac{m}{s}) \\ t &= 4.95s \end{aligned}$$

$$\begin{aligned} x(t) &= 0.5 * a * t^2 + v(0) * t \\ x(5.55) &= 0.5 * (-8.51 \frac{m}{s^2}) * (4.95s)^2 + (42.1 \frac{m}{s}) * (4.95s) \\ x(4.95s) &= 104.3m \end{aligned}$$

$$Kinetic\ Energy = \frac{1}{2} * m * V^2 = 133.65kJ$$

With a braking distance of 104m and the total braking distance allocation being 400m, there is considerable margin of safety.

Once the pod has come to a complete stop, controls begins the brakes 'cooldown' state, during which the calipers retract. Table 36 has the states of the valves for this state and braking.

Table 36: Braking Valve States

Action	NOV-1	NOV-2	NCV-1	NOV-3	NOV-4	NCV-2
To Brake:	Open	Open	Closed	Open	Open	Closed
To Cooldown:	Closed	Closed	Open	Closed	Closed	Open

Table 37 provides the expected ranges of the pressure transducers before and after these states.

Table 37: Expected Pressure Transducer Values (PSI)

Stage	BPT-0, BPT-1	BPT-2, BPT-3	BPT-4
Standby	$95 < x < 105$	$12 < x < 16$	$150 < x < 170$
Braking	$95 < x < 105$	$95 < x < 105$	$100 < x < 140$
Cooldown	$95 < x < 105$	$0 < x < 10$	$100 < x < 140$

For an off-nominal scenario where one system fails, we will brake using a single system which has a braking force of 641 N corresponding to a braking distance of 208 m. Even in this scenario, there is plenty of margin before the 400 m allocated would be reached. In the case of complete loss of power, the four normally open valves will open causing both primary and redundant braking systems to engage, just like in the nominal scenario. To release the brakes in such a scenario, the ball valve (BV-2) must be opened manually.

Our brake calipers and mount are mounted to the stability system. This system was tested in ANSYS to ensure that it has a significant stress safety factor. For both the rear system and the front system a 380 N force was applied to each brake pad (2 brake pads per caliper) in the Y-direction (green arrow in lower right corner of figure) which is 2.4 times our expected force. Figures 58 and 59 below show the equivalent stress in MPa for the rear and front systems.

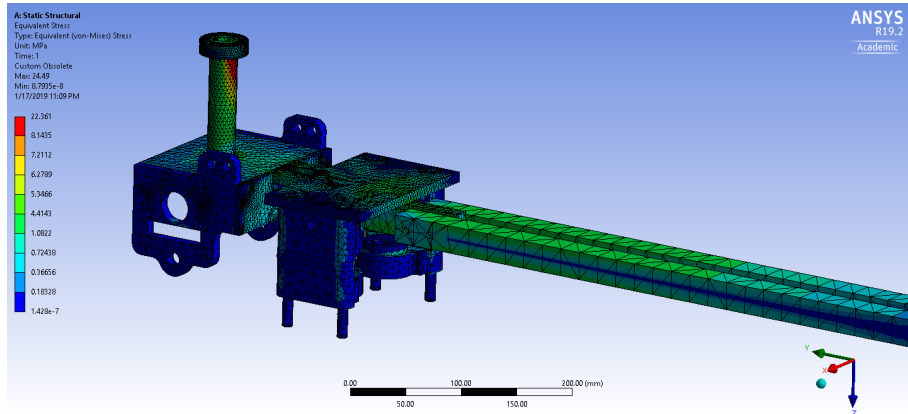


Figure 58: Stress Analysis for Rear Brake System

For our mounting plate, the maximum stress is about 5 MPa which is well within the elastic region for 6061-T6 Aluminum and has a safety factor of 10. The maximum stress occurs on the stability system mount which is relatively high, but the linear bearing is not shown which will decrease the torque on the shaft considerably. That being said, the stresses are still 6 times less than yield strength of the aluminum portion.

The deformations pictured below (figures 60 and 61) show that the maximum deformation is only 0.14 mm. When comparing this strain with the yield strength of the material, this is considerably in the elastic region.

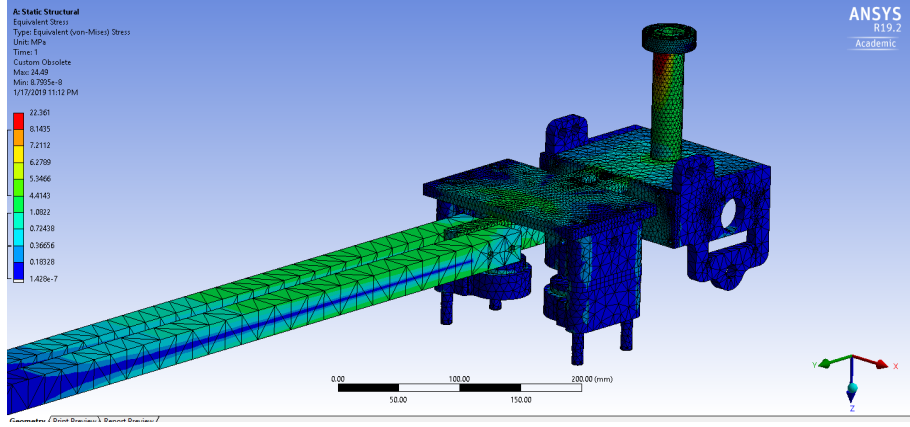


Figure 59: Stress Analysis for Front Brake System

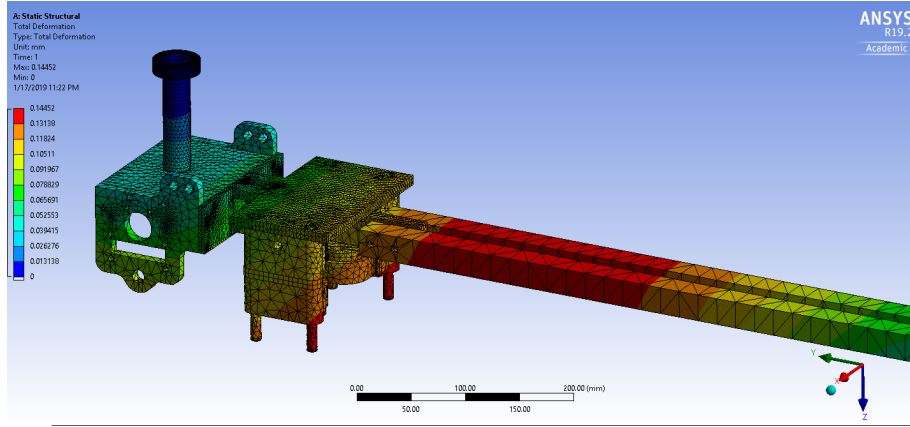


Figure 60: Deformation for Rear Brake System

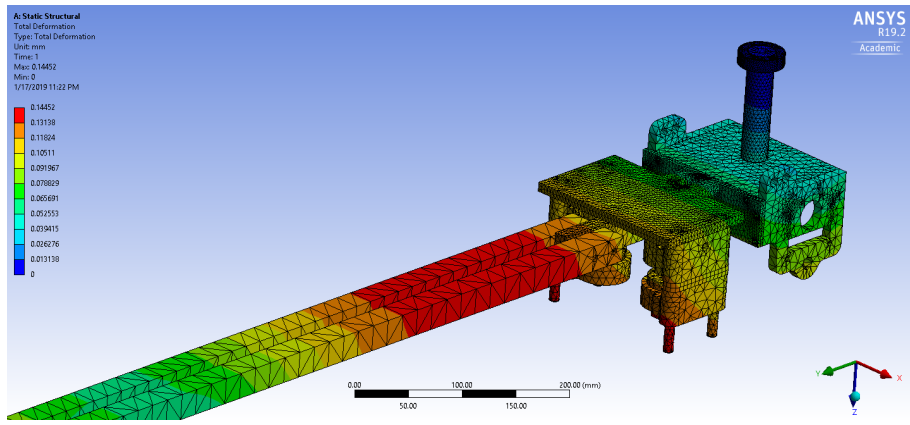


Figure 61: Deformation for Front Brake System

Based on this analysis, including the 2.4 times factor of safety for the force, our total safety factor is nearly 30 for the mounting plate. Because of this, a weight savings analysis will be done to lower the weight of the mounting plate.

3.9 Controls System

3.9.1 Overview

The OneLoop Team has been sponsored mainly by Rockwell Automation and will be using their platform and products for building a large portion of the pod's Controls System. Rockwell Automation has also

offered to guide our team in terms of refining and optimizing our algorithm on their platform so that we can fully utilize its features and safety capabilities. The design of the Controls System was implemented with the intention of minimizing complexity as much as possible to avoid uncertainties and safety concerns that will arise as a consequence of complexity. Instead of designing our own hardware modules, we relied on trusted off-the-shelf components to guarantee pod integrity and robustness.

3.9.2 Technical Description

The Controls System oversees the Propulsion and Braking Systems of the pod. It is responsible for monitoring sensor data, executing subroutines as well as pod error handling. A Programmable Logic Controller (PLC) will be used to conduct all the main operations and computations of the pod. The pod's status (health, position, velocity, etc.) is continuously communicated with the monitoring station with a Network Access Panel (NAP) which is interfaced to the PLC. The NAP supports bidirectional communication which will allow us to send operative commands to the pod.

3.9.3 Controller Program Loop

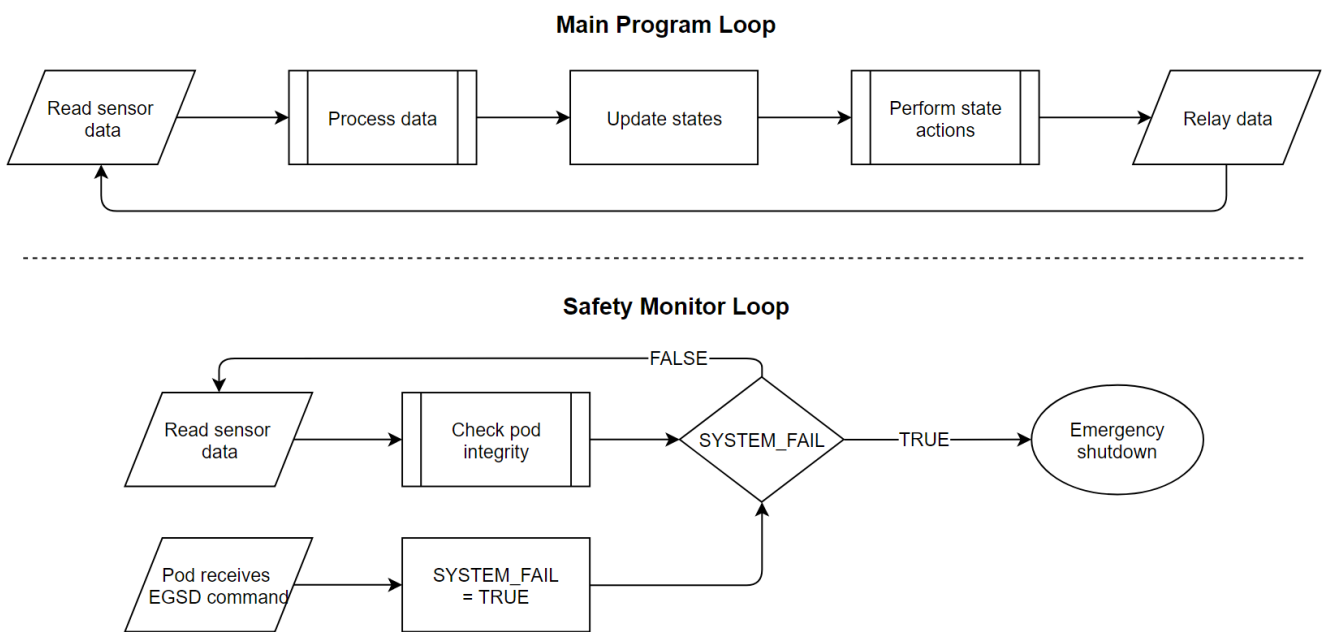


Figure 62: Flowchart of program loops

The Main Control Unit runs two loops in parallel: Main Program Loop and Safety Monitor Loop. The Main Program Loop is on the main memory of the PL Controller and the Safety Monitor Loop is run on a separate memory which is in the Safety Module (interfaced with PLC). The Main Program has five stages:

1. Read sensor data: Data from all sensors is read and saved in memory
2. Process data: The stored data is then processed to determine the pod's next actions
3. Update states: Based on the computation in the previous stage, pod's state is updated
4. Perform state actions: Actions relating to the new state of the pod are executed
5. Relay data: Information regarding pod's current status is relayed to the monitoring station

The Safety Monitor Loop has three stages:

1. Read sensor data: Data from all sensors is read and saved in memory
2. Check pod integrity: The stored data is then processed to determine the pod's health
3. **SYSTEM_FAIL** is **TRUE**: Pod is malfunctioning, next state is Emergency shutdown. See Transition 11 in Section 3.9.6 State Transitions

3.9.4 State Diagram

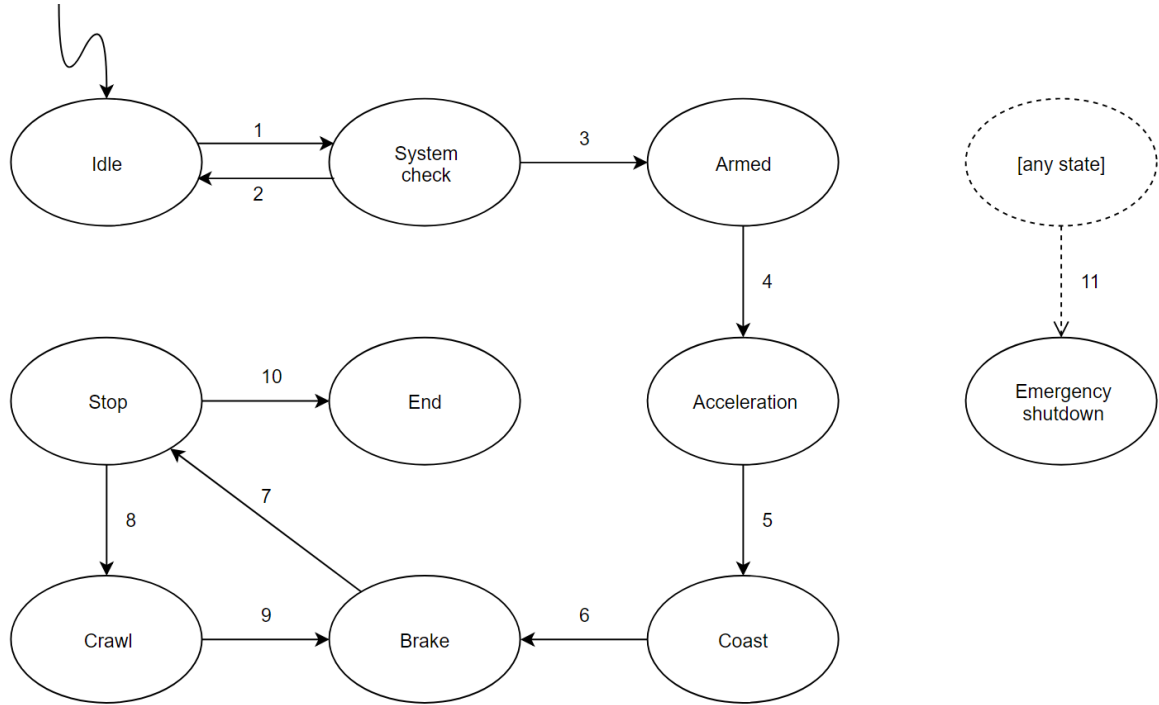


Figure 63: State diagram.

State Descriptions:

1. Idle

Idle is the state where the pod is not taking any actions. The pod enters this state when turned on. Pod remains in this state until it receives the BEGIN command.

2. System check

In this state the pod remains stationary, performs a brake actuation test (see Table 51 in Section 8), and checks the sensor data to make sure all systems are nominal for launch. The parameters of different subsystems that will be checked are as follows:

- Battery: Temperature, voltage, current
- Propulsion: Pressure, temperature
- Brakes: Pressure, temperature.

All sensor data will be sent to the monitoring station to confirm that sensors are outputting expected values. Discrepancies between two sensors measuring the same quantity will be noted at this point. The pod waits for a command to proceed. Possible outcomes here:

- (A) Nominal: all values are ideal. Pod is given the ARM command.
- (B) Realistic: some values are not ideal, but pod is still functional. Pod is given the ARM command.
- (C) Problematic: most or all values are not ideal, pod functionality is questionable. Pod is given the IDLE command.
- (D) Failure: most or all values are not ideal, pod may be malfunctioning. Pod is given the EGSD command.

3. Armed

If pod is in this state, the pre-launch protocol has been executed and the pod has successfully cleared all tests. The pod waits for a command to proceed. Possible outcomes here would be:

- (A) OK: sensor data is unchanged from previous state. Pod is given the LAUNCH command.
- (B) Not OK: sensor data is altered, which may cause problems during the run. Pod is given the EGSD command.

4. Acceleration

In Acceleration the pod first starts crawling using the onboard motors so that the main stage (propulsion system) only has to deal with rolling friction instead of static friction. After passing the 100 ft mark (3000 cm), the motors are turned off and the propulsion system is activated. In the ideal case, the pod reaches its top speed before 1300 ft. The pod goes into Coast automatically once the following conditions are satisfied:

1. POD_ACCELERATION reaches zero (0)
2. PROP_TNK_PRES falls below 200 PSIG.

Note: There are no hardware inhibits on braking during acceleration. But there is one software inhibit which occurs when pod transitions from Acceleration to Emergency shutdown i.e., the subroutine ‘Close propulsion valves’ needs to occur before brakes are activated.

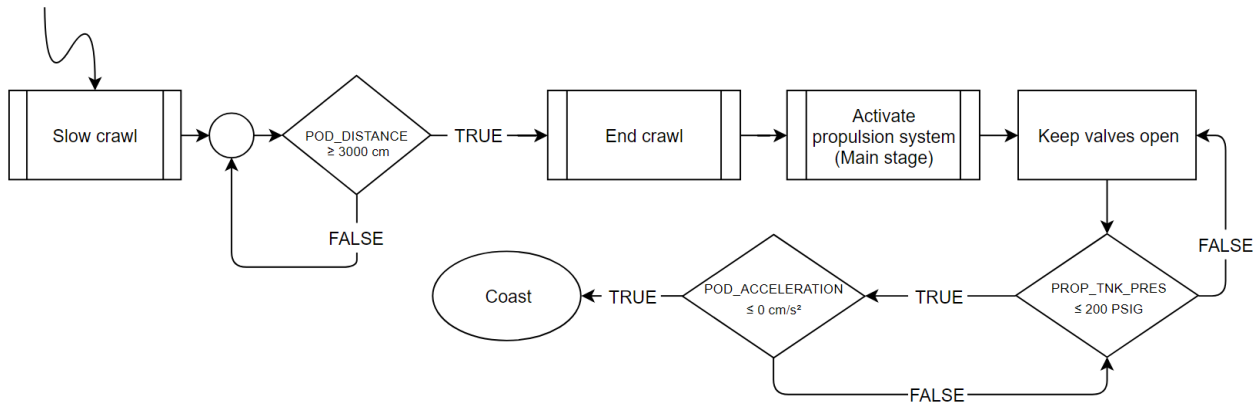


Figure 64: Flowchart of Acceleration

5. Coast

Coast is an intermediary state between Acceleration and Brake. In this state it is made sure that the propulsion system is no longer active by closing the air operated valves. The tanks are still pressurized, so they are first depressurized using the pressure release valves; this is done so that the pod no longer has any stored energy in the form of pressurized gas by the time it reaches the end of the track. The pod goes to Brake if:

1. The pod receives the STOP command, OR
2. POD_DISTANCE goes over 8000 centimeters, OR
3. COAST_TIMER goes over 10 seconds.

6. Brake

This is the state when the brakes are actuated and the pod begins braking. It is verified if the pod is braking by checking if the state variable POD_VELOCITY is decreasing. The failure detection and handling in the Braking system is analyzed in Section 6.1.3 Braking Safety.

7. Stop

The pod enters Stop after braking to a complete stop. In Stop the pod is stationary and is waiting to receive a command to determine the next step. The brakes are disengaged in this state, with a subroutine called Disengage brakes. However, the pod is not safe to approach yet.

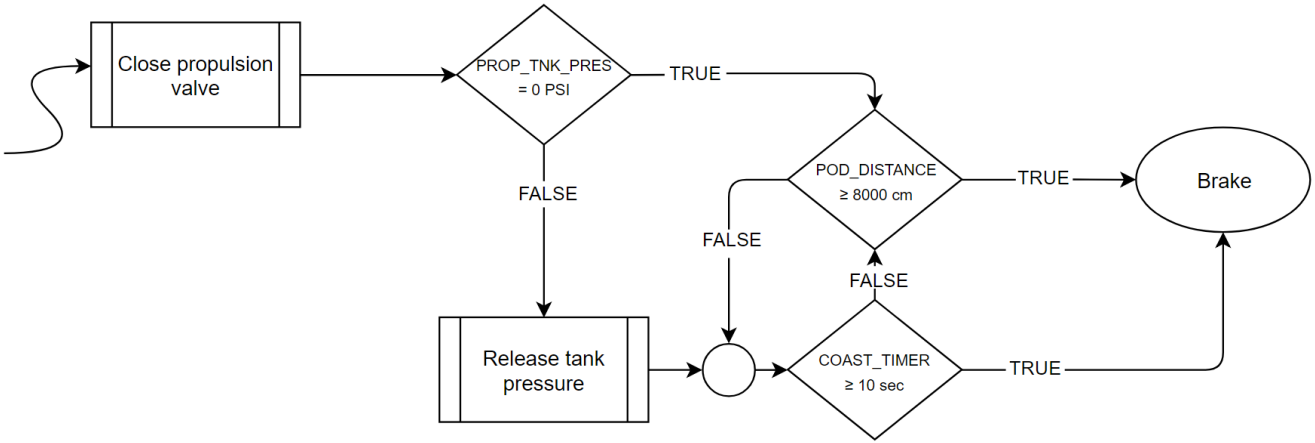


Figure 65: Flowchart of Coast

8. Crawl

In Crawl the pod propels itself using the on-board motors. The pod travels down the remaining length of the tube in this state. After the pod goes past a specified distance ($\text{POD_DISTANCE} \geq 125000$ centimeters) the pod will go to Brake again. The brakes should stop it in a distance of 100 feet or less from the end of the track, making it easy to unload the pod.

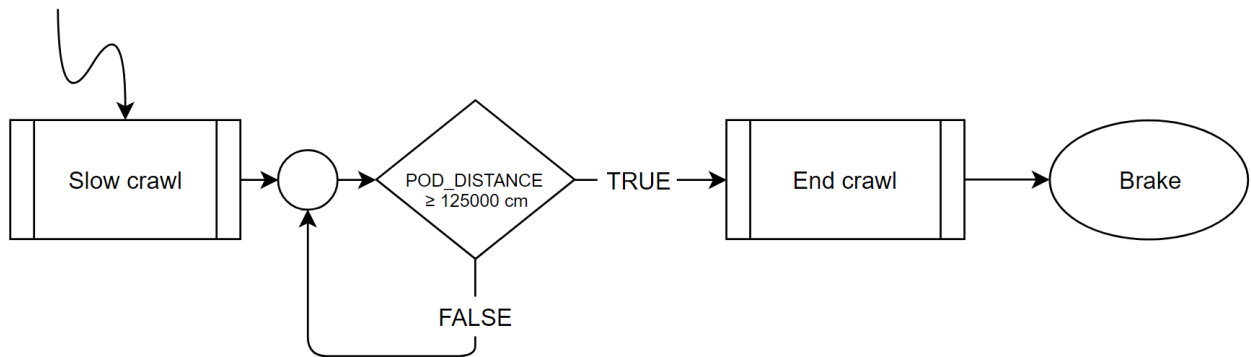


Figure 66: Flowchart of Crawl

9. Emergency shutdown

The pod enters Emergency shutdown if there is a critical failure in the propulsion, battery, braking or communication systems in any state. The state variable SYSTEM_FAIL is used to alert us of a critical failure. In this state the pod first makes sure that the propulsion valves are closed, engages its brakes, and then releases the remaining tank pressure.

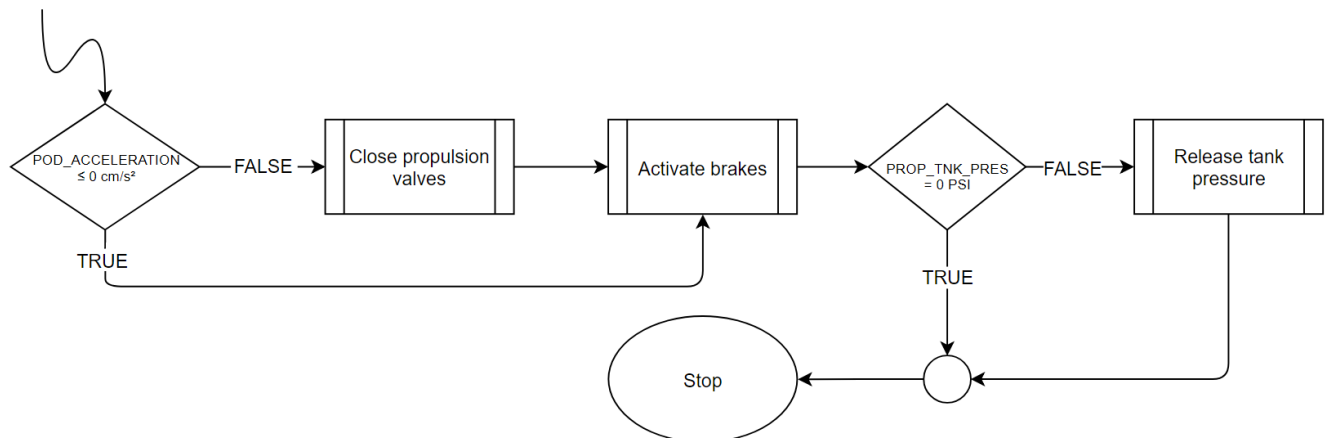


Figure 67: Flowchart of Emergency shutdown

10. End

In End the pod is stopped. The pod is safe to approach, and it cannot be activated again until a manual reset is performed.

3.9.5 Pod Navigation

The pod is equipped with two laser sensors on the chassis interfaced with the counter module (Allen-Bradley 5069 High Speed Counter Module) that can give us a precise count of retro-reflective stripes while the pod travels at a high velocity. This count tells how many tapes the pod has encountered, and the PLC calculates the distance travelled by using the given distance (100 ft) between consecutive strips of retro-reflective tapes. The data from the PLC is continuously transmitted using the Ubiquiti Rocket M900 Network Access Panel (NAP) to monitoring station. We will be able to know the pod's location with an accuracy of 100 ft. Ideally, the pod will go through a routine of 11 states from the start to the end of the run as follows:

- | | |
|------------------------|-----------------|
| 1. <i>Idle</i> | 7. <i>Stop</i> |
| 2. <i>System check</i> | 8. <i>Crawl</i> |
| 3. <i>Armed</i> | 9. <i>Brake</i> |
| 4. <i>Acceleration</i> | 10. <i>Stop</i> |
| 5. <i>Coast</i> | 11. <i>End</i> |
| 6. <i>Brake</i> | |

3.9.6 State Transitions

Note: (i) The sequence of these transitions do not follow the numerical order. Actual order is discussed in Section [3.9.5](#) Pod Navigation (ii) For list of commands and state variables, see Tables [38](#) and [39](#) respectively.

- **Transition 1:** The transition from Idle to System check. Triggered with the BEGIN command.
- **Transition 2:** The transition from System check to Idle. Triggered with the IDLE command.
- **Transition 3:** The transition from System check to Armed. Triggered with the ARM command.
- **Transition 4:** The transition from Armed to Acceleration. Triggered with the LAUNCH command.
- **Transition 5:** The transition from Acceleration to Coast. Automatically internal transition.
- **Transition 6:** The transition from Coast to Brake. Automatically internal transition, but can also be triggered with the STOP command.
- **Transition 7:** The transition from Brake to Stop. Triggered when the POD_VELOCITY is equal to 0.
- **Transition 8:** The transition from Stop to Crawl. Triggered with the CRAWL command.
- **Transition 9:** The transition from Crawl to Brake. Automatically internal transition, but can also be triggered with the STOP command.
- **Transition 10:** The transition from Stop to End. Triggered with the END command.
- **Transition 11 (Emergency shutdown transition):** The transition from any state to Emergency shutdown. Triggered if the system detects a critical failure i.e., if SYSTEM_FAIL is TRUE. The following flowchart gives more insight regarding the conditions that trigger this transition.

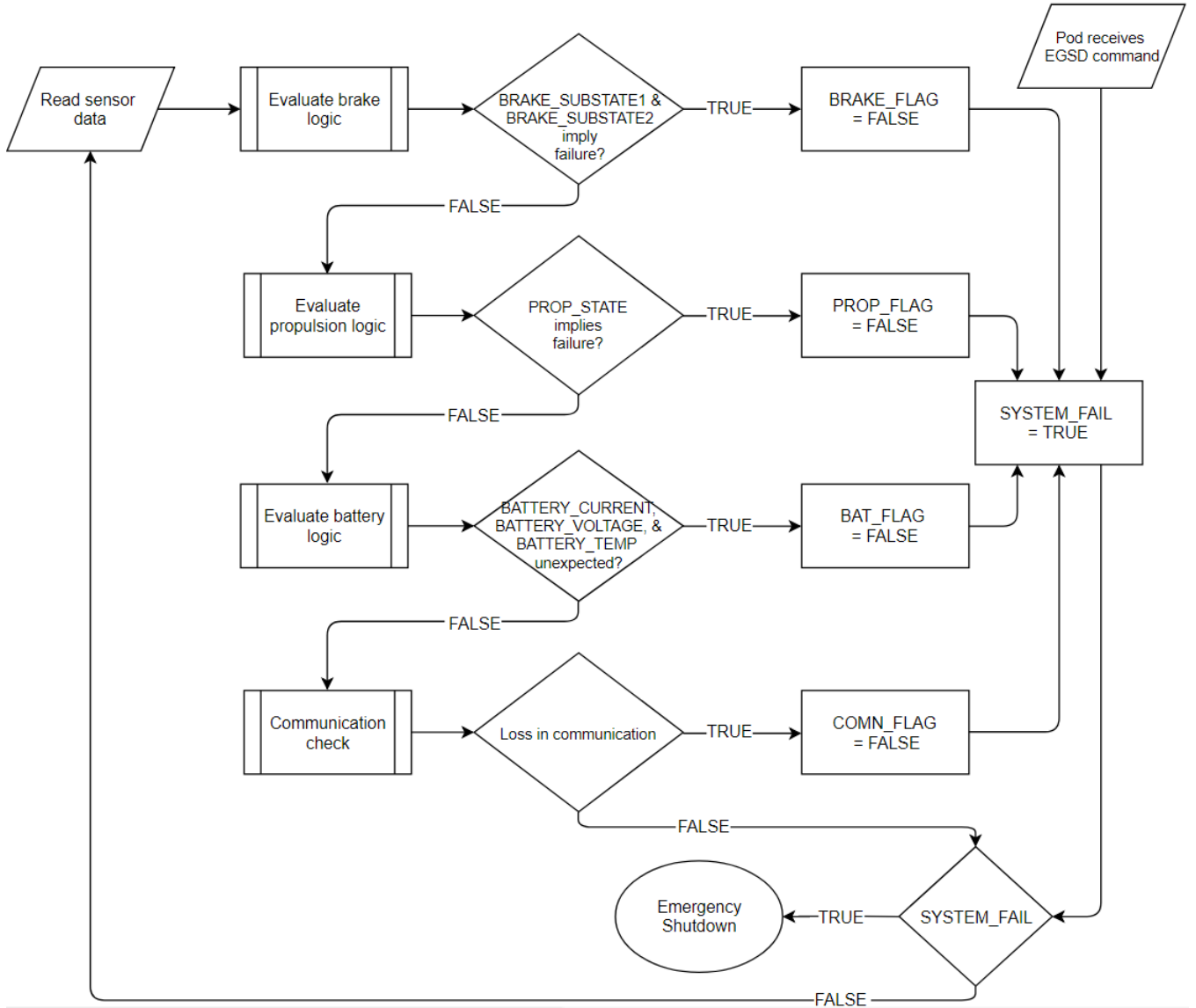


Figure 68: Safety Monitor Loop (expanded)

Table 38: List of all commands the pod can receive

Command	Description
BEGIN	Pod goes from Idle to System check
IDLE	Pod goes from System check to Idle
ARM	Pod goes from System check to Armed
LAUNCH	Pod goes from Armed to Acceleration
STOP	Pod goes from either Coast to Crawl to Brake
CRAWL	Pod goes from Stop to Crawl
END	Pod goes from Stop to End
EGSD	Pod goes from any state to Emergency shutdown

Table 39: List of state variables. They determine state changes during the run.

State variable	Type	Description	Dependency
STRIPE_COUNT	INT32	Number of stripes encountered by pod	C_Las0, C_Las1
POD_DISTANCE	INT32	Distance traveled by the pod from the start point, measured in centimeters (cm)	STRIPE_COUNT
POD_VELOCITY	INT32	Pod velocity, measured in centimeters per second (cm/s)	POD_DISTANCE
POD_ACCELERATION	INT32	Pod acceleration, measured in centimeters per second squared (cm/s ²)	POD_VELOCITY
COAST_TIMER	INT32	Starts counting up from zero once pod goes into Coast (seconds)	-
BATTERY_VOLTAGE	INT32	Voltage level of battery module, measured in millivolts (mV)	Main BMS, Secondary BMS
BATTERY_TEMP	INT32	Temperature of battery module, measured in tenths of a degree Celsius (°C/10)	Main BMS, Secondary BMS
BATTERY_CURRENT	INT32	Current drawn from battery module, measured in millamps (mA)	Main BMS, Secondary BMS
PROP_TNK_PRES	INT32	Minimum pressure among tanks (TA-1, TA-2, and TA-3, TA-4) in the propulsion system	P_Pres4/5
PROP_STATE	INT32	Condition of entire propulsion system. Can be either ‘nominal’, or ‘failure’.	P_Pres0/1/2/3/4/5/6, P_Tem0/1/2/3/4/5/6/7, & P_Tem8
BRAKE_SUBSTATE1	INT32	Condition of individual brake systems; can be either ‘nominal’, ‘sick’ or ‘failure’	B_Pres0/1/2/3/4 & B_Tem0
BRAKE_SUBSTATE2	INT32	Condition of individual brake systems; can be either ‘nominal’, ‘sick’ or ‘failure’	B_Pres5/6/7/8/9 & B_Tem1
PROP_FLAG	BOOL	FALSE if propulsion system fails; TRUE if system is nominal	PROP_STATE
BRAKE_FLAG	BOOL	FALSE if both brake systems report failure; TRUE if at least one brake system is nominal	BRAKE_SUBSTATE1/2
COMN_FLAG	BOOL	TRUE if communication between pod and monitoring station is active; FALSE if no communication is detectable	EtherNet I/O Adapter Module (interfaced with PLC)
BAT_FLAG	BOOL	FALSE if there is overheating, overcurrent, or undervoltage; TRUE otherwise	BATTERY_VOLTAGE, BATTERY_CURRENT, BATTERY_TEMP
SYSTEM_FAIL	BOOL	TRUE if pod is nonoperational; FALSE if pod is functioning	PROP_FLAG, BRAKE_FLAG, BAT_FLAG, COMN_FLAG

3.9.7 Implementation of Pod-Stop Command

There are multiple ways the pod comes to a stop:

1. After Brake, when the pod's state is Stop
 - Happens twice during ideal run
 - First time after Coast (Transition 6)
 - Second time after Crawl (Transition 9)
 - Two triggers for each transition: (i) Automated subroutine, (ii) STOP command from monitoring station
2. If Emergency shutdown transition occurs
 - In the unlikely case of system failure (SYSTEM_FAIL is TRUE), brakes are engaged. Any state can transition to Emergency shutdown. See Transition 11 in Section [3.9.6 State Transitions](#).

3.9.8 Pod Subroutines

These are the subroutines which will be programmed into the pod.

1. *Slow crawl:* A PWM control signal is sent to the motor controller; motors will make the pod crawl.
2. *End crawl:* PWM control signal to motor controller is stopped; motors are deactivated.
3. *Activate propulsion system:* Four 24VDC output pins connected to solenoids S-1, S-2, S-3, and S-4 are toggled to 24V. This will open air-operated valves A-1, A-2, A-3, and A-4. These valves open the system, propelling the pod forward.
4. *Close propulsion valves:* Four 24VDC output pins connected to solenoids S-1, S-2, S-3, and S-4 are toggled to 0V. This will close air-operated valves A-1, A-2, A-3, and A-4.
5. *Release tank pressure:* One 24VDC output pin connected to solenoid S-5 is toggled to 0V. This will open air-operated valve A-5 through which the tanks TA-1, TA-2, TA-3, and TA-4 will release remaining pressure.
6. *Activate brakes:* Six 24VDC output pins connected to solenoid valves NOV-1, NOV-2, NOV-3, NOV-4, NCV-1, and NCV-2 are set to 0V, causing the brakes to engage.
7. *Disengage brakes:* Six 24VDC output pins connected to solenoid valves NOV-1, NOV-2, NOV-3, NOV-4, NCV-1, and NCV-2 are set to 24V, causing the brakes to disengage.
8. *Evaluate brake logic:* Checks if all Braking sensors report expected values (for more info See Table [37](#) Expected Pressure Transducer Values in Section [3.8.3 Analysis](#)).
9. *Evaluate propulsion logic:* Checks if Propulsion system is operating nominally (for more info see Table [42](#) in Section [6.1.2 Propulsion Safety](#)).
10. *Evaluate battery logic:* Checks for undervoltage, overcurrent and overheating.
11. *Communication check:* The EtherNet I/O Adapter Module (1734-AENTR) which is interfaced with the PLC (5069-L3100ERS2) detects if communication is ongoing or failed.

3.9.9 Electronic System Overview

Sensor List

Sensors are categorized by the systems that they monitor. Systems are divided into controls, power, propulsion, and braking. The power system does not have individual sensors as all the sensors are on the battery management system (BMS).

Table 40: List of sensors

Sensor	Measurement	System	Qty	Label
Rockwell 42CM 18 mm LaserSight Photoelectric Laser Sensors	Distance	Controls	2	C_Las0, C_Las1
TFmini Lidar Range Finder Module	Distance	Controls	2	SX_Las0, SX_Las1
Super OMEGACLAD™ Thermocouple Probes	Temperature	Propulsion	9	P_Tem0/1/2/3/4/5/6/7/8
Rockwell 836P Solid-State Pressure Sensors	Pressure	Propulsion	7	P_Pres0/1/2/3/4/5/6
Rockwell 836P Solid-State Pressure Sensors	Pressure	Braking	10	B_Pres0/1/2/3/4/5/6/7/8/9
Super OMEGACLAD™ Thermocouple Probes	Temperature	Braking	2	B_Tem0, B_Tem1

Sensor Map

Sensor map shows where individual sensors are located within the subsystems.

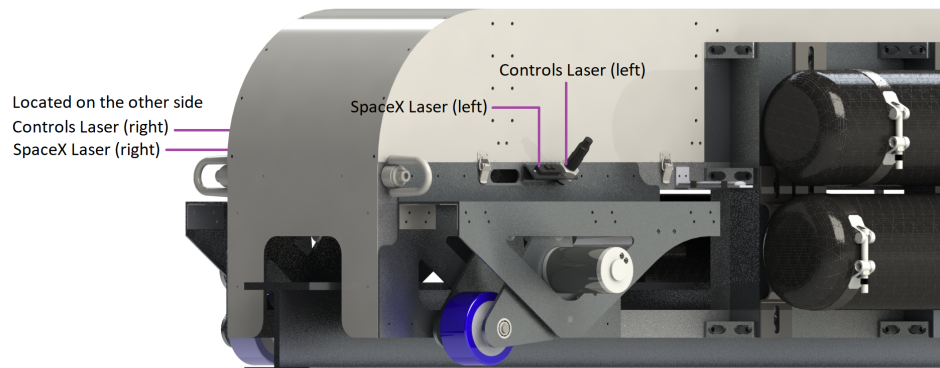


Figure 69: Controls & SpaceX sensors

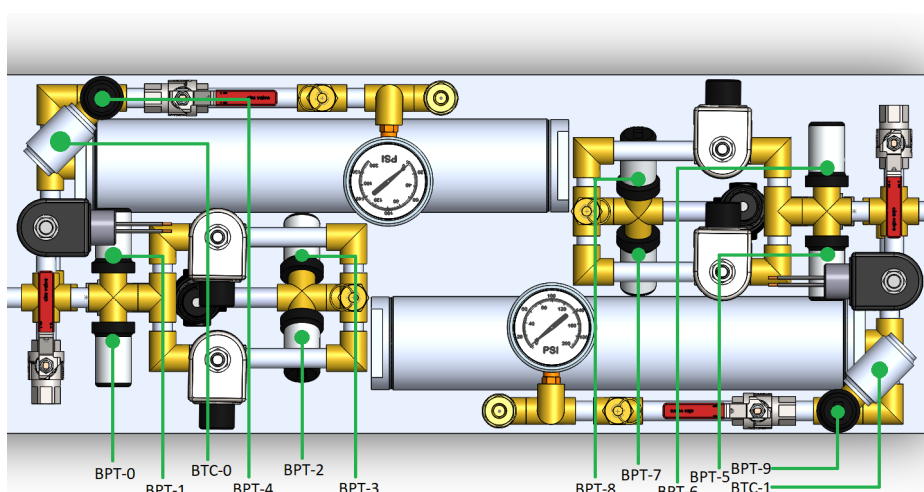


Figure 70: Braking sensors

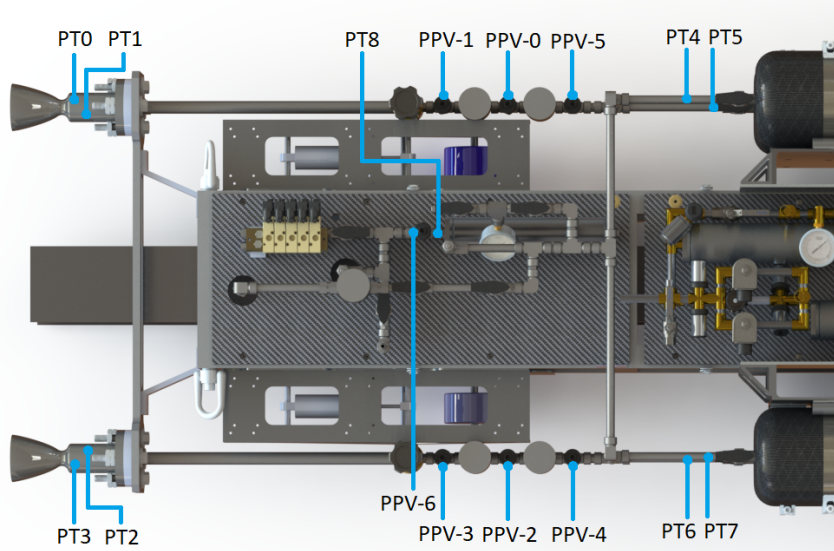


Figure 71: Propulsion sensors

Control Units

- *Main Control Unit:*
 - Rockwell Compact GuardLogix 5380 Safety Controller
 - The control unit is a Programmable Logic Controller (PLC). It controls all procedures of the Pod and runs the main program. The PLC also communicates with our monitoring station with the Ubiquiti Rocket M900 for telemetry and reception of commands.
 - The PLC is interfaced with a 5000 Series High-Speed Counter Module that counts pulses from sensors at rates of up to 1MHz. The HS counter module is interfaced with the laser sensors to give us an accurate count of the retro-reflective stripes when the pod is travelling at a high velocity.
 - The PLC interfaces with all the sensors using analog input pins and controls the pneumatic valves of braking and propulsion systems using digital 24V output pins. Communication with the SpaceX network is performed with User Datagram Protocol (UDP).
 - Rockwell Compact GuardLogix 5380 Safety Controller comes with the 1oo1 architecture that puts it at SIL 2 safety standard. This architecture will allow the Safety Monitor Loop run parallel to the Main Program Loop.
 - MTBF for this PLC is over 105,000 hours, so it is highly unlikely for it to fail during the run.
 - The PLC has the following certifications: ATEX, CE, c-UL-us, EtherNet/IP, IECEx, KC, RCM, TUV Rheinland, and UL Listed.



- *Speed sensing unit (as required by SpaceX):*
 - Arduino Uno REV3
 - This controller is connected to secondary laser sensors that are used to calculate the pod's position for SpaceX.
 - It is connected to the Ubiquiti Rocket M900 using a SainSmart Ethernet shield to transmit the recorded data.
- *Motor controllers:*

- DROK DC Motor Speed Control PWM Controller
- The PLC communicates with the motor controllers using PWM control signals.
- The motor controllers power the motors with PWM control signals as well.

- *Main BMS:*

- Battery Space BMS with SMBus, I2C, RS485, RS232 Communication
- The main BMS monitors the temperature, voltage and current of the main battery module.
- RS485 communication standard is used for communication between PLC and BMS.

- *Secondary BMS:*

- Battery Space BMS with SMBus, RS485, RS232 Communication
- The secondary BMS monitors the temperature, voltage and current of the secondary battery module.
- RS485 communication standard is used for communication between PLC and BMS.

Control Schematic

A simple diagram showing the data-flow in the pod.

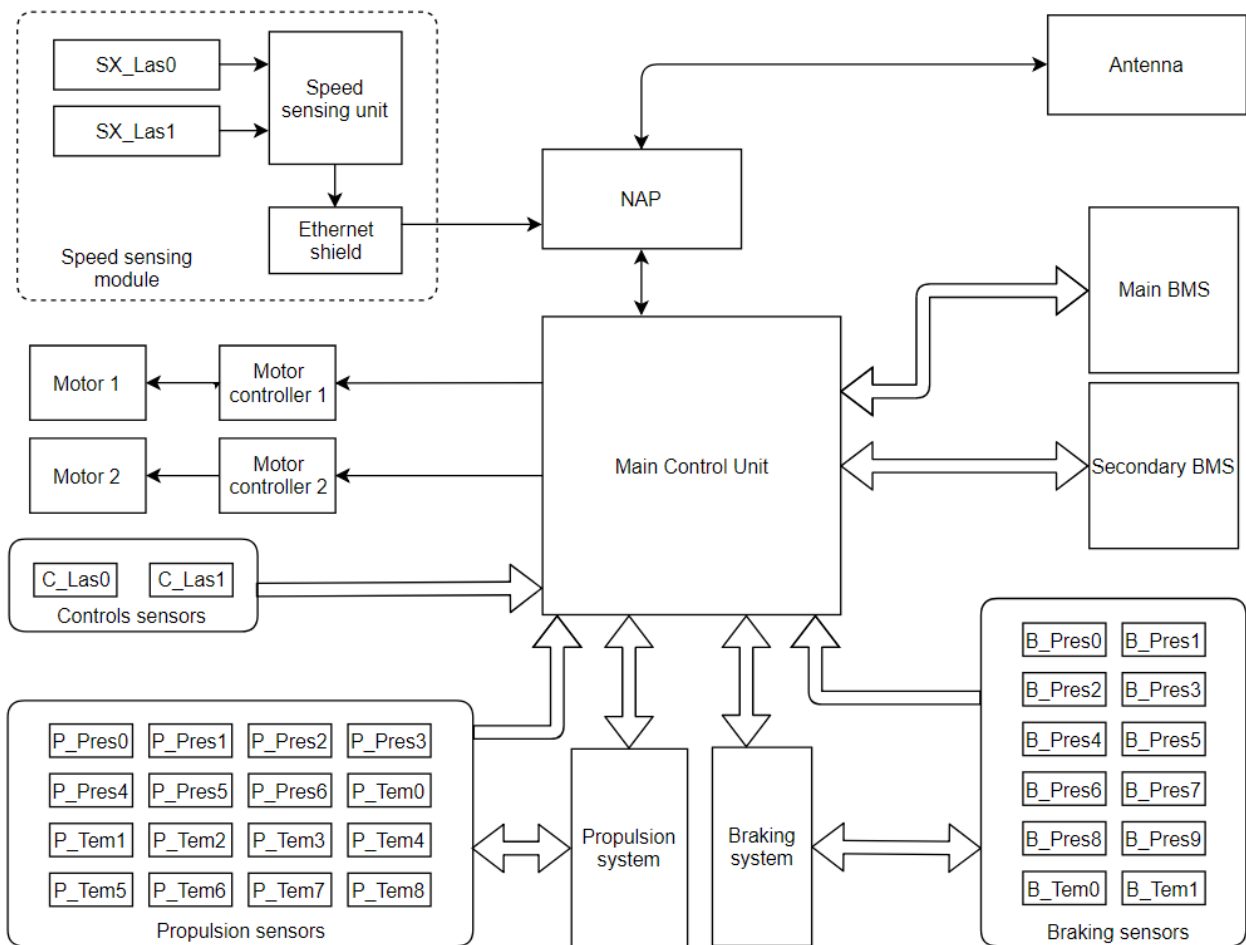


Figure 72: Schematic

Label	Component	Description
Main Control Unit	Rockwell Compact GuardLogix 5380 Safety Controller	Runs main program and interfaces with all other subsystems

Label	Component	Description
NAP	Ubiquiti Rocket M900	Establishes connection between pod and monitoring station
Antenna	900MHz to 2.5GHz Multi-Band 2dBi 1/4 Wave Blade	Used for transmission and reception of signals to and from monitoring station
SpaceX speed sensing unit	Arduino Uno REV3	Control unit for speed sensing as required by SpaceX
Ethernet Shield	SainSmart Ethernet Shield for Arduino Uno Mega, W5100	Establishes connection between NAP and SpaceX speed sensing unit
SX_Las0	TFmini Lidar Range Finder Module	Detects retro-reflections (right side of pod)
SX_Las1	TFmini Lidar Range Finder Module	Detects retro-reflections (right side of pod)
C_Las0	Rockwell 42CM 18mm LaserSight Photoelectric Laser Sensors	Detects retro-reflections (left side of pod)
C_Las1	Rockwell 42CM 18mm LaserSight Photoelectric Laser Sensors	Detects retro-reflections (left side of pod)
P_Pres0	Rockwell 836P Solid-State Pressure Sensors	Pressure of PPV-0 measured at valve A-1, in PSIG
P_Pres1	Rockwell 836P Solid-State Pressure Sensors	Pressure of PPV-1 measured at valve A-2, in PSIG
P_Pres2	Rockwell 836P Solid-State Pressure Sensors	Pressure of PPV-2 measured at valve A-3, in PSIG
P_Pres3	Rockwell 836P Solid-State Pressure Sensors	Pressure of PPV-3 measured at valve A-4, in PSIG
P_Pres4	Rockwell 836P Solid-State Pressure Sensors	Pressure of PPV-4 measured at tanks TA-3 and TA-4, in PSIG
P_Pres5	Rockwell 836P Solid-State Pressure Sensors	Pressure of PPV-5 measured at tanks TA-1 and TA-2, in PSIG
P_Pres6	Rockwell 836P Solid-State Pressure Sensors	Pressure of PPV-6 measured at tank TA-5, in PSIG
P_Tem0	Super OMEGACLAD™ Thermocouple Probes	Temperature of PT0 measured at Nozzle 1, in tenths of a degree Celsius (°C/10)
P_Tem1	Super OMEGACLAD™ Thermocouple Probes	Temperature of PT1 measured at Nozzle 1, in tenths of a degree Celsius (°C/10)
P_Tem2	Super OMEGACLAD™ Thermocouple Probes	Temperature of PT2 measured at Nozzle 2, in tenths of a degree Celsius (°C/10)
P_Tem3	Super OMEGACLAD™ Thermocouple Probes	Temperature of PT3 measured at Nozzle 2, in tenths of a degree Celsius (°C/10)
P_Tem4	Super OMEGACLAD™ Thermocouple Probes	Temperature of PT4 measured at tanks TA-1 and TA-2, in tenths of a degree Celsius (°C/10)
P_Tem5	Super OMEGACLAD™ Thermocouple Probes	Temperature of PT5 measured at tanks TA-1 and TA-2, in tenths of a degree Celsius (°C/10)
P_Tem6	Super OMEGACLAD™ Thermocouple Probes	Temperature of PT6 measured at tanks TA-3 and TA-4, in tenths of a degree Celsius (°C/10)

Label	Component	Description
P_Tem7	Super OMEGACLAD™ Thermocouple Probes	Temperature of PT7 measured at tanks TA-3 and TA-4, in tenths of a degree Celsius (°C/10)
P_Tem8	Super OMEGACLAD™ Thermocouple Probes	Temperature of PT8 measured at tank TA-5, in tenths of a degree Celsius (°C/10)
B_Pres0	Rockwell 836P Solid-State Pressure Sensors	Pressure of BPT-0 measured after regulator 1, in PSIA
B_Pres1	Rockwell 836P Solid-State Pressure Sensors	Pressure of BPT-1 measured after regulator 1, in PSIA
B_Pres2	Rockwell 836P Solid-State Pressure Sensors	Pressure of BPT-2 measured at calipers of system 1, in PSIA
B_Pres3	Rockwell 836P Solid-State Pressure Sensors	Pressure of BPT-3 measured at calipers of system 1, in PSIA
B_Pres4	Rockwell 836P Solid-State Pressure Sensors	Pressure of BPT-4 measured at tank 1, in PSIA
B_Pres5	Rockwell 836P Solid-State Pressure Sensors	Pressure of BPT-5 measured after regulator 2, in PSIA
B_Pres6	Rockwell 836P Solid-State Pressure Sensors	Pressure of BPT-6 measured after regulator 2, in PSIA
B_Pres7	Rockwell 836P Solid-State Pressure Sensors	Pressure of BPT-7 measured at calipers of system 2, in PSIA
B_Pres8	Rockwell 836P Solid-State Pressure Sensors	Pressure of BPT-8 measured at calipers of system 2, in PSIA
B_Pres9	Rockwell 836P Solid-State Pressure Sensors	Pressure of BPT-9 measured at tank 2, in PSIA
B_Tem0	Super OMEGACLAD™ Thermocouple Probes	Temperature of BTC-0 measured at tank 1, in tenths of a degree Celsius (°C/10)
B_Tem1	Super OMEGACLAD™ Thermocouple Probes	Temperature of BTC-1 measured at tank 2, in tenths of a degree Celsius (°C/10)
Main BMS	Battery Space BMS with SMBus, I2C, RS485, RS232 Communication	Monitors temperature, voltage level and current flow of main battery module
Secondary BMS	Battery Space BMS with SMBus, RS485, RS232 Communication	Monitors temperature, voltage level and current flow of secondary battery module
Motor controller 1	DROK DC Motor Speed Control PWM Controller	Controls the speed of motor 1
Motor controller 2	DROK DC Motor Speed Control PWM Controller	Controls the speed of motor 2
Motor 1	AndyMark 2.5" CIM Motor	Onboard motor to make the pod crawl
Motor 2	AndyMark 2.5" CIM Motor	Onboard motor to make the pod crawl

3.9.10 Sensor States

- *Nominal*

Sensor reports a value $\leq 2\sigma$ away from the mean of the latest 10 samples.

- *Sick*

Sensor reports a value $>2\sigma$ and $\leq 3\sigma$ away from the mean of the latest 10 samples. This happens in the case of a sensor having an offset error. For quantities that depend on two sensors, if one of the two sensors is sick, only the nominal sensor will be used.

- *Failure*

Sensor reports no value (0), or a value completely out of the reasonable set of possibilities ($>3\sigma$ away from the mean of the latest 10 samples or negative values).

Note: σ is the standard deviation of the latest 10 samples recorded by the sensor.

3.9.11 GUI

The Graphical User Interface will be built using Rockwell Studio 5000 and FactoryTalk. In the GUI, the current state of the pod, state variables and sensor data will be displayed. There will also be buttons to input manual commands. Sensor readings will be color coded based on whether they receive a nominal reading (GREEN), sick reading (YELLOW), or failure reading (RED). Alongside the readings of the sensors, we also note when they were last updated.

Commands		
BEGIN	IDLE	ARM
LAUNCH	STOP	CRAWL
END	EGSD	

State variables	
Name	Value
STRIPE_COUNT	10
POD_DISTANCE	30480
...	...

Current state			
Acceleration			

Subsystem	Sensor Name	Value	Last updated
Brakes	Sensor X	Nominal	
Propulsion	Sensor Y	Failure	
Controls	Sensor Z	Sick	

Figure 73: Example of GUI (tentative)

4 Pod Thermal Profile

4.1 Introduction

In this section we will be covering the considerations taken into account concerning the heat transfer imposed by the several pod systems onto their surroundings during the length of pod operation. Specifically we will be focusing on the temperature changes across the back wall of the test track during pod start up and in the wheels and stability system during a run. This is to determine the Pod's ideal initial spacing from the wall as well as not to exceed material temperature limits for the propulsion and wheel. For the propulsion systems, this scenario is being considered the worst case scenario for heat transfer between the track and the pod, as the limited thrust duration and high speed of the cart would enable far less heat transfer between exhaust gasses and the test track once the pod has reached its maximum

speed. For the wheels, this means proving that the wheel temperature does not exceed the critical value even with a conservative estimate.

4.2 Heat Transfer Due to Propulsion Systems

4.2.1 Model & Analysis

In order to accurately assess the transient temperature variance of the back wall, we had to first adopt a model for the heat transfer occurring due to the impinging jets of the pod on the back wall of the test track. For this, we adopted Bergman's model for an in-line array of impinging jets as seen in Equation 25, and Figure 74. The gas composition of the exhaust from each jet comprised of 92% N^2 , so for model simplicity we adopted Pr , ν , & k as listed in Bergmans text for N^2 at the exhaust temperature from each nozzle.

$$\frac{\overline{Nu}}{Pr^{0.42}} = 0.5 * K * G * Re^{\frac{2}{3}} \quad (25)$$

Where: $\overline{Nu} = \frac{\bar{h}D}{k}$, $Re = \frac{V_e D}{\nu}$

$$K = \left[1 + \left(\frac{H/D}{0.6/A_r^{\frac{1}{2}}} \right)^6 \right]^{-0.05}, \quad G = 2A_r^{\frac{1}{2}} * \frac{1 - 2.2A_r^{\frac{1}{2}}}{1 + 0.2(H/D - 6)A_r^{\frac{1}{2}}}$$

$$A_r = \frac{\pi D^2}{4S^2}$$

The use of Bergman's model would allow us to calculate the average convection coefficient (\bar{h}) due to the array of jets, from which we could calculate the transient heat transfer of the back wall. with the formulation for \bar{h} , we then had to adopt a model for the time dependent transience of our system. For this we adopted the general lumped capacitance method, seen in Equation 26 [4] ignoring heat transfer from radiation, heat generation and conduction. The LCM, aka. the Lumped Capacitance Method, assumes that the change in temperature with time is spatially independent throughout the solid. This assumption is only valid when the Biot number of the system, a quantity measuring the ratio of convective to conductive heat transfer in the solid, is relatively low (< 0.1). So, before adopting the LCM method to model the transience of the back wall, we calculated a worst case Biot number to validate the use of the LCM method, that being with an initial separation distance of 0.5m at $t = 0$ s, which produced a value of $Bi = 0.135$. this would mean that for most of our test cases, where $t > 0$ & $H_o > 0.5m$ the lumped capacitance model would be reasonably accurate. We also took into account the changing separation from the wall due to the acceleration of the pod, this was factored into Bergman's Impinging jet model which results in a changing convection coefficient with time.

$$-\bar{h}(T_s - T_\infty)A_{s,(c,r)} = \rho V C_p \frac{dT_s}{dt} \quad (26)$$

In order to model the back wall, we assumed an infinite flat plate made of the same material and thickness as the walls of the test track. Limiting our conduction purely through the thickness of the wall itself. Compressing all our models into one equation, we are left with a first order non-linear ODE, which we subsequently solved using a first order backwards finite difference approximation with the initial condition being an initial wall temperature of 25°C, at room temperature.

4.2.2 Results

In Figure 75 you can see the results of our model, with the surface temperature of the back wall as a function of both initial pod separation and time. From the surface, we may see that as the initial separation is increased, the overall steady state temperature of the wall increases as expected. Furthermore, the temperature of the back wall seems to reach steady state value at around 4-5 seconds after the initial firing of the engines, regardless of initial separation distance.

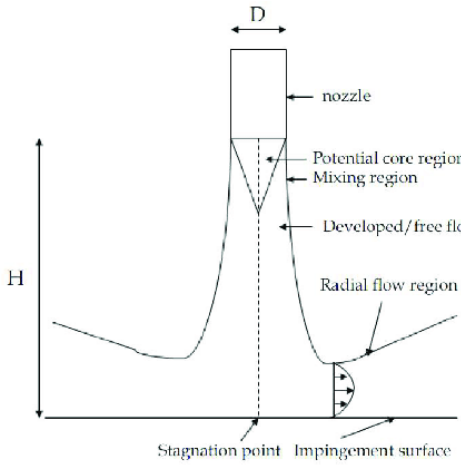


Figure 74: Impinging jet on a flat plate [4]

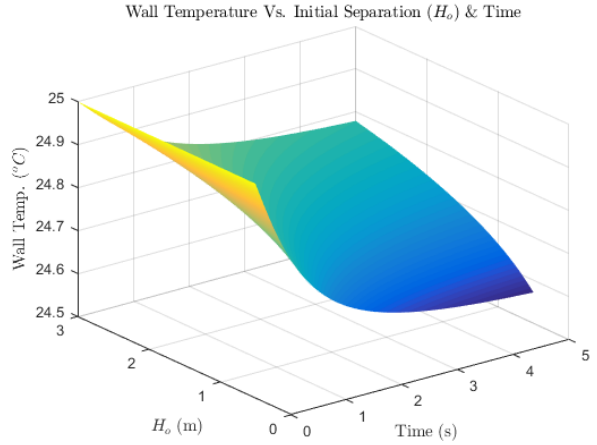


Figure 75: Variation in Wall Temperature W. Respect to Time and Initial Separation (H_o)

4.2.3 Discussion

Referring to Figure 75, we can see that across all initial separation distances from the wall, the impinging jets actually cool the surface rather than heating it. This is because the exit temperature for the gasses leaving each nozzle was calculated to be around 70K. Due to this fact, the temperature gradient at the surface of the back wall between the exit gasses and the wall itself will always be positive, thereby removing heat from the wall itself.

4.3 Heat Transfer Due to Wheel Friction

4.3.1 Model and Analysis

To address the heat generation in the wheels during a typical run, a model was developed involving stick slip zones shown in Figure 76 [20] created from the load on a single wheel. The deformation in the wheel resulting in a slip plane is assumed to only occur elastically in the radial direction while the frictional heating is assumed that it only occurs over this slip area. Additionally, this model assumes constant loading on wheels and uniform pod velocity for geometry and frictional calculations. The slip area was derived through the geometry and load, with a relationship between the wheel radial strain and slip area provided in Equation 27.

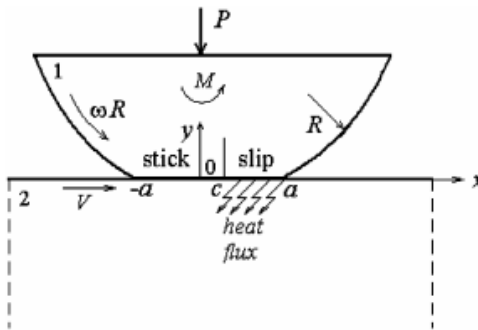


Figure 76: Heat Generation Due to Rolling [20]

$$A_{\text{slip}} = wr \sqrt{\epsilon(2 - \epsilon)} \quad (27)$$

where strain is defined by the weight applied to each wheel and the polyurethane elastic modulus, solving Equation 28 for ϵ .

$$\epsilon^4 - 2\epsilon + \left(\frac{F}{2wrE}\right)^2 = 0 \quad (28)$$

The problem is then solved as a transient thermal 1D conduction problem through nodal analysis. In order to assume worst case heating, it is assumed that no convective cooling occurs between wheel and the gasses within the track. The track is modeled as a surface of uniform temperature since a new portion of track at ambient temperature is assumed to be constantly in contact with the wheel. The heat generation is due to the friction in the slip zone of the wheel where it is assumed that the wheel is being uniformly heated at the wheel surface. Therefore, finite difference methods are used to solve for the temperature at each point spatially at each time interval. Six node types were modeled to represent the temperatures of: the test track wall, the wheel surface, the polyurethane rim, the aluminum wheel core, and two special node types being the node bridging the polyurethane and aluminum and the center node of the wheel. Appropriate heat equations were written for each node type balancing heat transfer within the node as a function of temperature gradient and thermal conductivity of used materials. Due to a lack of information on the thermal properties of the specific blend of polyurethane in the wheels, properties taken from similar hard rubbers are used to approximate the temperature profile within the wheel. Estimations for heat transfer into the track due to friction are uncertain, as a solid value for thermal contact resistance between the polyurethane wheels and the track was difficult to estimate. This, coupled with the fact that the overall temperature increase of the wheels is highly sensitive to the heat flux into the track makes temperature profiles highly volatile. To account for this, extreme cases where no heat transfer and no contact resistance were performed as well as a more realistic 10% conductivity coefficient for the aluminum track, the results of which can be seen in Figure 77. The total heat transfer simulation was set over a time period of 36 seconds, equivalent to the full pod's estimated run duration.

4.3.2 Results

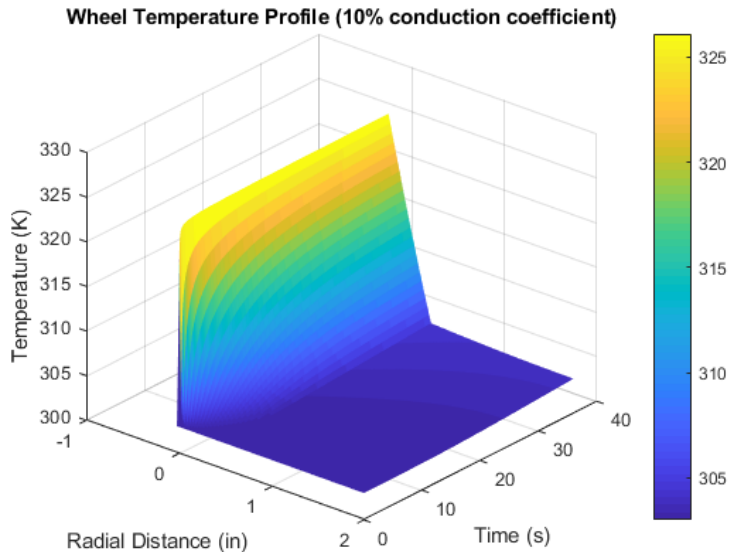


Figure 77: Temperature Vs. Time of Wheel Surface with 10% Wall Conduction

From the surface plot for 10% aluminum conductivity coefficient shown in Figure 77, it is evident that the maximum temperature reached at the wheel surface at the end of the run is 326.1K. As expected, the temperature increases vs time and decreases vs distance away from the contact.

4.3.3 Discussion

The maximum temperature of 326.1K reached during the pod run is lower than the 355K normal operating temperature specified by the manufacturer but still represents a higher estimate due to conservative

assumptions. In reality, there is nonzero heat transfer away due to convection and radiation which serve to lower the maximum operating temperature. The pod velocity used is also an upper estimate and reflects a higher heat generation than if lower speeds are reached. Finally, a conservative estimate for the conduction into the track results in a larger temperature increase throughout the polyurethane.

4.4 Conclusions

Through both analyses, thermal considerations are met for the propulsion and wheel systems. The propulsion impinging jet analysis proved that cooling would occur due to the exit gas temperature, avoiding critical material temperatures while the wheel thermal analysis demonstrated that maximum temperatures were not exceeded despite conservative estimates.

5 Predicted Vibration Environment

The primary sources of vibration are identified as the propulsion nozzle, vertical suspension, and brakes. To give initial insight into the expected pod vibration frequencies, each of the these subsystems will be thoroughly tested. Note that other sources will be investigated as well, but we predict that these three locations will see the highest vibrational loads.

The propulsion assembly will be tested for vibration as per system tests S2, S3, and S4 using accelerometers as stated in Section 7.1.5. The suspension systems will be fastened to the chassis along with weights to simulate the rest of the components on the pod. A shaker table will then be used to simulate the track bumps in the vertical direction. The frequency imparted into the chassis from the vertical suspension will be measured using accelerometers. See Section 7.1.4 for more detail. As for the brakes, a flywheel attached to a motor will be used to test the braking force in nominal and off-nominal cases (see Section 7.1.6 for more detail). During these tests accelerometers will be attached to the braking system to measure the frequencies produced.

Once all of the vibration data from the major frequency contributors are collected, their respective waveforms will be superimposed to create a single frequency. The shaker table will then be set to this superimposed frequency test the entirety of the pod. Proper safety measures will be taken to ensure no damage to others or the pod during all testing.

6 Safety

6.1 Subsystem Safety

6.1.1 Power Safety

In order to ensure a safe power system, several considerations in battery selection and connections are made. Notably, all the cells used in building the battery packs will be brand new with no salvaged or recycled cells being used. Normally, this eliminates the need for fuses, but for extra protection and redundancy fuses will be added. Cell level fuses have the ability to keep the pack working with less capacity if a fuse wire melts, maintaining the pod's operation. Cell level fusing has proven to work well for reducing the risk of total battery pack failure. So, Tesla style cell fusing will be used.

Contingency Plans for Failures

-*Main pack failure:* The main battery pack and the backup pack will operate at the same time. The PLC will draw power from whichever module has the most capacity. This prevents the PLC from losing power in case the main pack fails.

-*Battery fire at staging area:* In the event that any of the batteries catch fire, a class B fire extinguisher will be applied. If the switches can be safely flipped then they should be. If the Aeroshell is attached, then it should be removed using the four latches, two on the left and right of the pod, if safe

to do so, to access and extinguish the batteries. If the fire is too dangerous to approach, all personnel should evacuate to a safe distance until the fire is out and wait for emergency response.

-Primary pack fire on track during run: The backup pack and secondary pack will be stored with shielding between them and the main pack. In the event of a fire, the pod can still operate and the wheel motors are still powered if the main pack fails. If it is still on fire, proceed with the plan outlined above for a fire at the staging area

-Fuse blown: In the event that a fuse is blown (fuse bar melts), the backup battery module can still provide power for braking.

6.1.2 Propulsion Safety

In analyzing the safety of the propulsion system, a systematic three-way approach is taken. Safety analysis is broken up in the following categories:

Table 42: Safety Categories

Aspect	Scope
Pod and System Safety	State monitoring of propulsion system. Corrective actions taken to prevent damage to pod, tube or track. Design considerations selected to make this propulsion system safe
Operational Safety	Dangers and associated risks that occur with operation of this system. Sequence of filling operation. Actions in place to reduce the safety risks present to human operators and spectators
Hazardous Materials	Identification and description of hazardous materials pertinent to this propulsion system.

Pod Safety

To prevent damage to the tube, track, and pod, several problems will trigger the sick, or failure state of the system:

Table 43: Pod Safety Conditions

Problem	Condition	Action
Significant pressure difference between the two thrusters.	Given PPV-0 or PPV-1 and PPV-2 or PPV-3 are in nominal state, the PLC will perform the calculation with the sensors that are nominal and check the given condition: $(PPV_0,PPV_1) - (PPV_2,PPV_3) > 30 \text{ PSIG}$	1. Propulsion system is transitioned to “FAILURE” state
Significant temperature difference between the two thrusters.	Given PT0 or PT1 and PT2 or PT3 are in the nominal state, the PLC will perform the calculation with the sensors that are nominal and check the given condition: $(PT0,PT1) - (PT2,PT3) > 40 ^\circ\text{F}$	1. Propulsion system is transitioned to “FAILURE” state

Table 43: Pod Safety Conditions

Problem	Condition	Action
Air operated valves (A-1, A-2, A-3, A-4, A-5) do not open	No output exists for PPV-0 and PPV-0 is not labeled as “sick,” A-1 can be considered as “not open” The same condition is true for PPV-1 and A-2, PPV-2 and A-3, PPV-3 and A-4	1. Propulsion system is transitioned to “FAILURE” state 2. A-1 or respective sensor is labeled as “not open”
Solenoid valves (S-1, S-2, S-3, S-4, S-5) do not open	Respective voltage sensors to S-1, S-2, S-3 or S-4 read less than 24V. S-5 has no voltage input since it is normally open	1. Propulsion system is transitioned to “FAILURE” state 2. Respective solenoid valve is labeled as “not open”
A detectable failure is present in any single pressure transducer (PPV-0, PPV-1, PPV-2, PPV-3, PPV-4, PPV-5, PPV-6)	Refer to Section 3.8 on the controls system for a description of conditions for sensor failure	1. Faulty sensor transitions system to “SICK” state 2. Any other failure transitions pod to “FAILURE” state
A detectable failure is present in any single thermocouple (PT0, PT1, PT2, PT3, PT4, PT5, PT6, PT7, PT8)	Refer to Section 3.8 on the controls system for a description of conditions for sensor failure	1. Faulty sensor transitions system to “SICK” state 2. Any other failure transitions pod to “FAILURE” state
Pressure irregularity in tanks TA-1, TA-2	PPV-5 > 4550 PSIG	1. System transitioned to “FAILURE” state
Pressure irregularity in tanks TA-3, TA-4	PPV-4 > 4550 PSIG	1. System transitioned to “FAILURE” state
Pressure irregularity in tank TA-5	PPV-6 > 250 PSIG	1. System transitioned to “FAILURE” state
Temperature irregularity in tanks TA-1, TA-2	If both PT4 and PT5 are nominal, check TBD < ((PT4+PT5)/2) > TBD If either PT4 or PT5 are sick, use the nominal sensor and check TBD < (PT4, PT5) > TBD	1. System transitioned to “FAILURE” state
Temperature irregularity in tanks TA-3, TA-4	If both PT6 and PT7 are nominal, check TBD < ((PT6+PT7)/2) > TBD If either PT6 or PT7 are sick, use the nominal sensor and check TBD < (PT6, PT7) > TBD	1. System transitioned to “FAILURE” state
Temperature irregularity in tank TA-5	If PT8 is nominal, check TBD < PT8 > TBD	1. System transitioned to “FAILURE” state

System Safety

In designing this system, four different standards were followed. These standards are:

- ASME B31.3
- ASME BPVC
- ISO 4414
- NASA Safety Standard for Hydrogen and Hydrogen Systems

In addition, this design complies with the pressurized system safety guidelines outlined on page 9 of the “2019 SpaceX Hyperloop Pod Competition Rules and Requirements November 30, 2018” document.

Operational Safety

There are three different dangers with this propulsion design that pose a health and safety risk to operators or spectators. An overview of these dangers and their corresponding risks are below:

Table 44: Health Risks

Potential energy from gas compression	Temperature/Heat	Noise
Serious bodily injury	Thermal contact burns	Noise induced hearing loss
Embolism	Death	Tinnitus
Death		

Noise

One large concern is the high sound level that will occur when the gas exits the nozzles. The expected maximum sound level from one nozzle, given by the maximum fluid outlet velocity (1206 m/s) and the exit area ($4.06 \times 10^{-3} \text{ m}^2$) of one nozzle, is 140 dB [8]. By treating both nozzles as sound sources and considering their sound waves to be incoherent, the total sound level of both thrusters can be calculated using sound level addition. This equation is shown below:

$$L_A \text{ and } L_B = 10 \log_{10}(10^{L_A/10} + 10^{L_B/10}) \text{ dB} \quad (29)$$

From this equation, the total sound level from both equations is calculated to be 143 dB OSHA 1910.95 - Occupational noise exposure states that one should have a maximum of 15 minutes of exposure to a 100 dB noise per day. Considering that the threshold for pain is 140 dB, the noise seen from nozzles should be treated as a safety risk. Because of this, several corrective actions are planned to reduce or deter exposure- these actions are listed below in terms of their effect

1. As originally planned, the door of the test track will be closed.
2. All individuals involved in filling of the tanks shall wear noise protection which has a NRR of 32dB or more
3. A caution sign which indicates the potential for high noise will be placed next to the filling station and will comply with OSHA 1910.145-Specifications for accident prevention signs and tags

High Temperature Zones

Two areas, each nozzle's respective catalyst bed, will reach high maximum temperatures (745 K) due to the rapid temperature increase of the gas along with the preheating that will occur. Dangers stem from individuals accidentally touching these areas. Several deterrents that will be used to minimize the chance of this danger occurring are:

1. Caution tape will be placed around the pod during the preheating and filling process as to deter individuals from walking near the pod

2. Areas that will become hot will have appropriate tape, or signs indicating the dangers from touching this area. The utilized tape and caution signs will comply with OSHA 1910.145-Specifications for accident prevention signs and tags
3. Two class C fire extinguishers will be kept near the pod as it is loaded into the tube

Potential Energy from Gas Compression

The third and most lethal safety risk predicted is the potential energy of the stored gas in the tanks. This stored energy safety risk becomes even more present and dangerous during the filling process prior to the pod launch. This team is actively designing a remote filling system for these tanks. To be extra safe, a standard operating procedure for filling of both tanks is established and outlined below.

SOP Title: Cold gas thruster fill procedure

- *Section 1 Process:* This SOP outlines a safe procedure for filling of four COPV tanks to 4500 PSIG of a Oxygen, Hydrogen, and Nitrogen gas mix from two external storage tanks. This process must be completed before pod operation occurs.
- *Section 2 Hazardous Chemicals:* A 92% Nitrogen, 2.67% Oxygen, 5.33% Hydrogen gas mix pressurized to 6000 PSIG in fill tanks, 4500 PSI in pod tanks.
- *Section 3 Potential Hazards:* Pressure and explosions
- *Section 4 Approvals Required:* Two lockout tags which lock operation of the fill procedure must be unlocked by Daniel Nasr-Church
- *Section 5 Designated Area:* This procedure will take place in a 10 square foot area at the Hyperloop Pod Competition pod entrance. This procedure will also take place either in the Chevron Lab at UC Davis (this teams workspace) or an outside area determined by EFL shop safety staff.
- *Section 6 Process Steps:*

Preparation:

1. Be familiar with hazards associated with operation of high pressure systems
2. Ask valve and tank vendor for assistance with questions related to operation and pressure relief devices (Done)
3. Examine tanks and pressure relief valves for signs of defect. Do not proceed if defects are found
4. Verify that lockout tags are removed from manual valves
5. Verify that the external storage tanks are fixed to the ground
6. Verify that the four tanks being filled are fixed to the pod
7. Verify that the flexible high pressure hose connecting the external storage tank to the propulsion system is connected properly
8. Verify that operator 1 and operator 2 both have safety glasses and ear protection equipped

Use:

1. Operator 1: Open the fill regulator (40 scfh) on the external storage tanks
2. Operator 2: Open manual valves M-1 and M-2
3. Operator 1: Proceed to watch for any dangers that appear during the filling process. If these dangers are present, stop filling and empty both tanks by opening M-3,A-5
4. Operator 2: Proceed with filling while watching the pressure on pressure gauge G-1
5. Operator 2: As the pressure reaches 4500 PSIG, begin closing M-1 to decrease the flow rate from the external storage tank

6. Operator 2: Close flow control valve M-1 when the necessary pressure is achieved (4500 PSIG)
7. Operator 2: Close manual valve M-2
8. Operator 1: Verify that both manual valve M-1 and flow control valve M-2 are closed. If this is not the case, proceed to close these valves
9. Operator 1: Close the flow from the external flow tanks
10. Operator 1: Disconnect the high pressure hose from the propulsion system

Hazardous Materials

Please refer to Section 6.4 Hazardous Materials of this report which details all hazardous materials this propulsion system contains.

6.1.3 Braking Safety

The following figure is the state diagram for fault cases in the Braking system. Any detectable failure in a sensor causes the system to go into a Sick state (for more info see Section 3.8.10 Sensor States). Once in the Sick state, any additional failure (including another sensor going into Sick state) will cause the entire system to fail and brake immediately. If either the primary or secondary braking systems are in the failure state, the pod will begin braking immediately after stopping propulsion (for more info see Transition 11 in Section 3.8.6 State Transitions). Braking is also induced if both the brake systems are in the Sick state. These states are constantly monitored by the Controls system during the run.

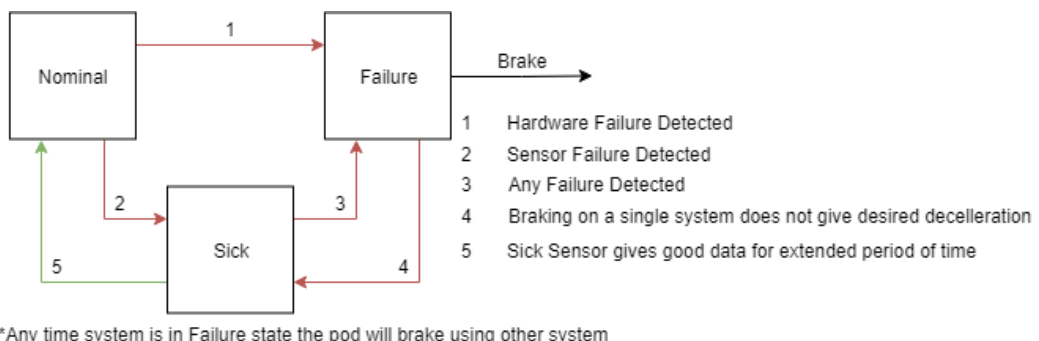


Figure 78: Fault Case State Diagram for Friction Brake System

From a Controls standpoint, there are multiple cases where the brakes will be engaged (See Section 3.9.7 Implementation of Pod-Stop Command).

6.2 Additional Safety Features

6.2.1 Inhibits on Braking During Acceleration

Due to the necessity to brake even if the pod loses power, there are no hardware inhibits for the braking system during the acceleration phase. There are, however, software inhibits that are built into the state diagram. Even in an emergency shutdown case, the transition from the ‘Acceleration’ state to the “Emergency Shutdown” requires that valves A-1 through A-4 are closed before braking begins. These valves are normally closed, so in the event of pod power loss they will still close as the brakes engage.

6.2.2 Mechanisms to Mitigate Complete Loss of Power

Main Pack Failure

In the event of the main pack power loss, the secondary pack will allow for normal pod function. It consists of a lower cell count 24v battery back located in a physically different location such that a failure in one pack due to localized deformation or fire as detailed within the power section. The parallel connection.

Brakes

If absolute complete loss of power occurs, the normally open valves will be able to stop the pod in the

allotted stopping distance. Braking will occur in the event of any subsystem or power failure as the valves will open and engage the brake pads.

6.2.3 Single Points of Failure and Pod Failure Analysis

Controls

The controls system consists of the main control unit, the PLC, and all of the connections to the necessary sensors, switches, and valves.

The PLC will be purchased by Rockwell, ensuring that it has been thoroughly tested. It will be further tested by our team during our system testing phase as well as the complete pod testing phase. A majority of the monitors are part of redundant set which means that a single detectable monitor failure would cause the control system to lose visibility into that measurement. This is critical for measurements such as pressure in the brake lines, or propulsion tank pressure which must be known in order to operate nominally.

(See Section [3.9.7 Implementation of Pod-Stop Command](#))

Brakes

To assess the fault tolerance of the braking subsystem, a FMECA analysis was done. The FMECA was used to create a single points of failure (SPF) list as well as assess weak points in the design that have been fixed with post-PDR design updates.

The FMECA was also used to detect issues with our system that could be resolved with redundant parts, some of which are the pressure sensors and normally-open valves. See Figure [56](#). As seen in our pneumatic diagram, our system has two pressure transducers upstream and downstream of the control valves, which has redundancy to detect the pressure before the valves and the pressure of the caliper brakes. There are also redundant valves which means one stuck closed valve will have no effect on the system performance.

Propulsion

See Figure [41](#) for reference to propulsion subsystem diagram.

To ensure that a single failure will not inadvertently cause one thruster to activate, there are redundant air-operated normally-closed valves in series. To identify a failure in one of these valves, pressure sensors are located between and after them.

If one air-operated valve fails, then its corresponding thruster will not activate, producing an unequal thrust which results in a torque on the system. As a result, these valves have been added to the SPF list below. Controls will be able to locate this failure by monitoring pressure sensors P-2 and P-4, and can enter the ‘Emergency Shutdown’ state to close all valves, relieve the stored gas, and begin braking. Testing will be done to determine the time between the failure, failure detection, and failure mitigation.

Single Points of Failure List

Table 45: SPF List

Subsystem	Component	Failure Description	Effect	Mission Critical	Compensating Provisions
Braking	Caliper Brakes	Pneumatic piston fails retracted	Loss of symmetric braking to one system	Yes	Redundant braking system, part bought from WC Branham (very well tested)

Table 45: SPF List

Subsystem	Component	Failure Description	Effect	Mission Critical	Compensating Provisions
Braking	Normally-Closed Valve (NCV-1)	Stuck Closed	Pod unable to be removed from Hyperloop remotely	No	Testing, Manual Ball valve can be used if this failure occurs
Braking and Propulsion	Piping	Burst	Loss of pressure in system. Total system failure.	Yes	Purchasing tubing with excess pressure rating. Pressure test system to 1.5 times working pressure.
Braking and Propulsion	Piping Connections	Leak	Slow pressure loss. Decrease in system performance.	Yes	Perform full system leak and pressure test after final assembly.
Propulsion	Pressure Regulator (Q-1,Q-2)	Fails to Regulate	Unequal Thrust	Yes	Reliability Testing
Propulsion	Air-Operated Valves (A-1,A-2,A-3,A-4)	Fails Closed during acceleration initiation	Unequal Thrust	Yes	Valves rated For 5000 PSI and operating at 4500 PSI, Reliability Testing
Propulsion	Pneumatic Valves (S-1,S-2,S-3,S-4)	Fails Closed during acceleration initiation	Unequal Thrust	Yes	Valves rated For 150 PSI and operating at 110 PSI, Reliability Testing

6.2.4 Recovery Plan if Pod Becomes Immovable within Tube

There are only two scenarios that could result in the pod becoming immovable: a failure in Normally-Closed Valve 1 (NCV-1) or a complete loss of both primary and backup pod power. NCV-1 is used to release the brakes by exhausting the air from the calipers. If one of these conditions occurs, then the only way to unlock the calipers would be to manually open BV-2 to exhaust the air. If this occurs, team members would need to enter the Hyperloop tube. Prior to entering the tube, the controls system will confirm that the pod is in the ‘End’ state. If all power is lost, these members would also need to manually push the pod to the end of the track.

6.3 Stored Energy

A description of stored energy on the pod is detailed below:

All stored energy through compressed gas was calculated using the AB-532 document established by ABSA. The equation in this document to compute stored energy is shown below:

$$E = (2.5)x(P_{at})x(V) * [1 - (P_a/P_{at})^{0.286}]dB \quad (30)$$

This document provides an accurate estimate for Nitrogen and air, and a extremely conservative estimate for lighter gases, such as the one shown below being Helium

This pod, unlike the previous year’s design, does not incorporate any strong magnets.

Table 46: Pod Stored Energy List

Stored Energy Source	Subsystem	Equivalent Stored Energy
Tri Gas mixture(92% N_2 , 2.67% O_2 , 5.33% H_2 at 4500 PSI	Propulsion	427 kJ
Tri Gas mixture(92% N_2 , 2.67% O_2 , 5.33% H_2 at 4500 PSI	Propulsion	427 kJ
Tri Gas mixture(92% N_2 , 2.67% O_2 , 5.33% H_2 at 4500 PSI	Propulsion	427 kJ
Tri Gas mixture(92% N_2 , 2.67% O_2 , 5.33% H_2 at 4500 PSI	Propulsion	427 kJ
0.81L of 140 PSIG compressed air for front friction brake assembly	Friction Brakes	1.06 kJ
0.81L of 140 PSIG compressed air for front friction brake assembly	Friction Brakes	1.06 kJ
0.81L of 110 PSIG compressed air for propulsion actuated valve actuation (TA-3)	Propulsion	0.80 kJ
Main battery system (49 Li-ion cells in a 7s6p)	Power	0.378 kW-hr
Backup battery system (21 Li-ion cells in a 7s3p configuration)	Power	0.189 kW-hr
Secondary battery system (24 Li-ion cells in a 4s6p configuration)	Power	0.216 kW-hr

6.4 Hazardous Materials

Several hazardous materials are used in the construction, testing, and operation of this pod. Safety data sheets which comply with OSHA's Hazard Communication 1910.1200 standards can be found in a folder called "Safety Reference Information," which has been submitted along with this final design report.

Storage of hazardous materials occurs in four distinct areas. Pictures of these areas are shown below to demonstrate compliance with OSHA standards:

Table 47: Hazardous Materials

Material	Subsystem	Storage Location
Palladium Catalyst	Propulsion	Hazardous Material
Tri Gas mixture(92% N_2 , 2.67% O_2 , 5.33% H_2 at 4500 PSI	Propulsion	Gas cylinder cage
Compressed air at 110 PSI	Propulsion	Gas cylinder cage (if not empty)
Compressed air at 140 PSI	Friction Brakes	Gas cylinder cage (if not empty)
LG chem Li-Ion 2.5 Ah cells	Power	Battery storage cabinet
Tin/Lead solder	Controls	General storage Cabinet



Figure 79: Gas Storage Area

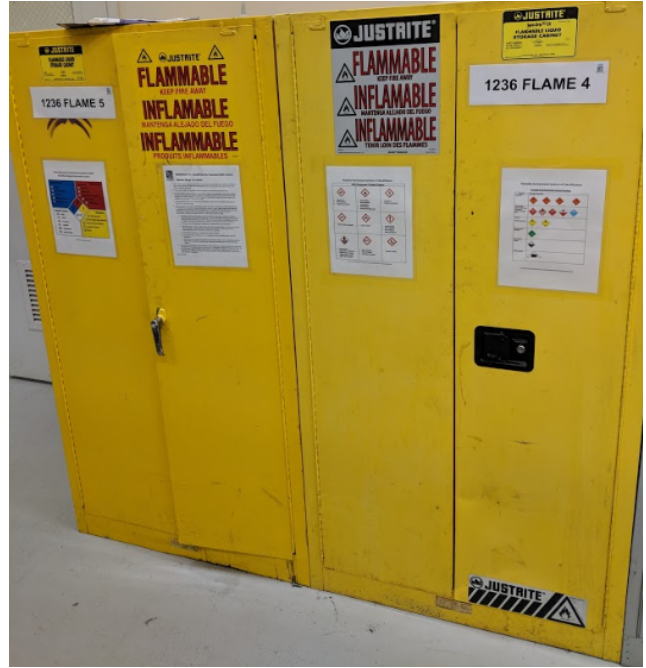


Figure 80: Hazardous Materials Cabinet



Figure 81: Battery Storage Cabinet



Figure 82: General Materials Cabinet

Flammability of Propellant and Gas Cylinder Standards

For the tri-gas mixture in use, OSHA Comparison of Hazard Communication Requirements [13], Section 2.4.2 defines “artificial air” as containing up to 23.5% vol Oxygen. Although Oxygen and Hydrogen are both flammable, our tri-gas mixture contains less than 23.5% vol Oxygen, and as such the combination of oxygen and nitrogen can be treated as air. Despite the low oxygen volume, however, the mixture contains greater than 1% Hydrogen. Therefore, the mixture is considered to be an organic peroxide, and has the potential to be flammable. To investigate the flammability of the propellant, the following sections of NASA’s Safety Standards for Hydrogen and Hydrogen Systems are relevant [15].

(a) Hydrogen-Air Mixture.

1 The LFL for hydrogen-air mixtures rises to about 9 percent by volume hydrogen above 10.3 MPa (1500 psia), and the UFL rises to about 75 percent by volume above 8.3 MPa (1200 psia). Data indicate that the lowest pressure for which a low-energy ignition source produces ignition is approximately 6.9 kPa (1 psia), at a hydrogen concentration of between 20 and 30 percent by volume (Hertzberg and Litton 1981).

202a

2-11

2 Various hydrogen-air mixtures were subjected to a 45 mJ (4.27×10^{-5} Btu) spark ignition source in a 311 K (100 °F) temperature environment (Mills, Linley, and Pippen. 1977 and Benz and Boucher 1981). The tests indicate that the LFL was 4.5 percent by volume over the pressure range 34.5 to 101.3 kPa (5 to 14.7 psia). An increasingly richer hydrogen mixture was required to obtain combustion below 34.5 kPa (5 psia). The lowest pressure for which a low-energy ignition source produced ignition was 6.2 kPa (0.9 psia) at a GH₂-air mixture of between 20 percent and 30 percent by volume GH₂ (Thompson and Enloe 1966).

3 Using a strong ignition source, the lowest pressure for which ignition occurs is 0.117 kPa (0.02 psia).

4 Raising the temperature from 290 to 673 K (62 to 752 °F) decreases the LFL of hydrogen-air (downward propagation) from 9.0 to 6.3 percent by volume hydrogen and increases the UFL from 75 percent to 81.5 percent by volume hydrogen. Data are for a pressure of 101.3 kPa (14.7 psia).

Figure 83: Air Mixture Literature

Figure 84: Air Mixture Literature

As the above sections show, our Hydrogen percentage of 5.33% is below the lower flammability limit of 9% for high pressure systems. Therefore, the propellant in our tanks is non-flammable. Furthermore, when the propellant leaves the system, it will equilibrate to a pressure of 0.125 PSI, which is lower than the lowest pressure recorded for ignition of 0.9 PSI, which occurred for a much higher Hydrogen percentage than our system uses. Another source of comfort that our system will not be flammable is the image shown below, which indicates that the water vapor produced by the catalytic reaction is even more adept at reducing flammability limits than the inert gas. Therefore, our propellant is not flammable within the tanks (and no ignition source is present to ignite it if it were), will not be flammable upon reacting, and will remain non-flammable when relieved to the tube.

Some more information about gas cylinder safety is mentioned below:

All gas cylinders, per OSHA's Hazard Communication Standard (HCS)[13], are labeled to alert the user of the contained gas and its hazardous properties.

Following OSHA 1910.116[13], Inspection and Maintenance Requirements for Compressed Natural Gas Storage Cylinders, gas cylinders that are property of UC Davis Hyperloop are inspected for indications of deterioration, bulging, or leaking by Daniel Nasr-Church and Austin Gonzalez one time per week. If abnormal conditions of any gas cylinder are found, the gas cylinder will be decommissioned. Furthermore, this finding will be documented and communicated promptly to the department safety coordinator, Loan-Anh Nguyen.

Gas cylinders being transported will have a valve protection cap. Transportation will occur in a safe manner and will be no further than 20 meters from the cage to the work area. During competition, a separate tri-gas mixture cylinder of sufficient volume will be rented at a location close to the competition to minimize the necessary transportation distance.

Battery Storage Batteries are currently being stored and charged in accordance with OSHA 1926.441,

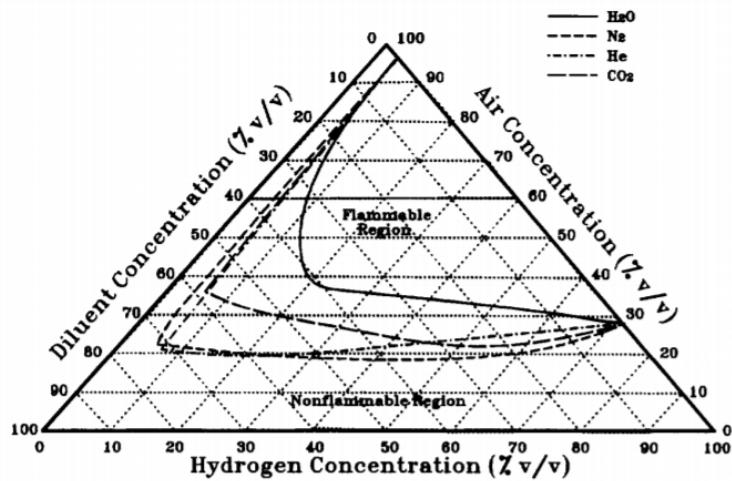


Figure A2.2
Effects of N₂, He, CO₂, and H₂O Diluents on Flammability Limits of Hydrogen in Air at 101.3 kPa (14.7 psia) (The effects of N₂, He, and CO₂ are at 298 K (77 °F) and H₂O is at 422 K (300 °F))

Batteries and Battery Charging. Some major requirements from this OSHA standard are:

- An eye and body drenching station is located within 25 feet of the battery storage/handling area
- The floor of the workspace is acid resistant
- Face shields, aprons, and rubber gloves are used when handling batteries or battery acid
- Ventilation is provided in the workspace and storage area to ensure diffusion of gases from batteries
- Battery charging instructions are located in the battery storage cabinet
- Storage racks and trays are resistant to the battery electrolyte

Daniel Nasr-Church (Propulsion Lead) will be responsible for the handling and storage of all hazardous materials. Daniel's relevant safety certifications are listed below:

- OSHA 10-Hour (License 34-006030448)
- UC Davis Lockout/Tagout Training (completed 01/07/2018)
- UC Davis Hazardous Material Handling and Storage Training (completed 01/07/2018)
- UC Davis Lab Safety Fundamentals Training (completed 05/24/2018)
- OSHA Control of Hazardous Energy Training (In progress)
- OSHA Hazardous Communication for Supervisors and Managers Training (In progress)

6.5 Vacuum Compatibility Analysis

Based on research from last year's competition, vacuum compatibility problems are most likely to occur within the Power subsystem. However, our low-power team mindset and commitment to thorough testing prior to competition should be able to mitigate any potential failures within the power system. For more information on how the power (and controls) system will be vacuum tested, see Section 7.1.7 and Section 7.1.1 of this report.

The structures, stability, and suspension systems involve only mechanical connections, with exception to the motors used to power the wheels on the suspension system, which will also be vacuum tested, and

are therefore not at risk of vacuum complications.

The braking and propulsion subsystems will be affected by vacuum environment conditions, since they involve pneumatic systems. However, this difference can be quantified by simply adding 14.7 PSI to all differential pressure calculations, which will not affect the performance of the pneumatic systems. More specifically, this change in differential pressure only affects propulsion, since all pneumatic systems for opening and closing valves are isolated from the ambient pressure. With regard to propulsion, an additional 14.7 PSI is negligible compared to the much higher pressures seen in the tanks and thrust chamber.

7 Testing

7.1 Subsystem Testing

7.1.1 Power Testing

System Tests

- *Thermal Test*

Goal: Find the maximum current each individual cell can safely discharge, maximum temperature each cell can safely operate at before internal shorting happens, and the average temperature the battery will operate in under a normal pod run.

Method: The modules will be discharged at 2C continuously for a prolonged period of time (1 hour, assuming that is the maximum runtime). After the temperature is spread evenly within the modules and the terminals of the cells are cooling down, the temperature “hotspots” will be captured by thermal imaging. The temperature at the time will be the nominal operating temperature. Thermal hotspots will be ideal locations for temperature sensors.

Expected Results: Enough data from multiple tests to come up with a safety threshold, temperature threshold to set as a condition to shut off battery pack, and a temperature value to set as a nominal. Additional comments: Alternatively can ask manufacturer for max peak current and max temperature.

- *Vacuum Testing*

Goal: Determine whether the packs will function nominally under nominal, and max load situations. Observing the temperature of the cells to see if they stay within safe levels is the main concern of this test.

Method: The packs will one by one be placed inside a vacuum chamber connected to a mock-up pod that will use the actual electricity demanding controls components to simulate either nominal or max loads. Temperature will be measured by contact sensors and IR sensors, if available. Each test will last an hour or until the packs run out of charge.

Expected Results: Battery packs will perform normally, and stay within safe temperature ranges in the vacuum environment. Additional comments: Additional Comments: It may also be of interest to see if the cells behavior will change at all after discharging in a vacuum, such as being able to hold less charge.

7.1.2 Structures Testing

To validate the structures analyses in Section 3.2.4, tests will be performed on critical structural components. Depending on the component and its loading conditions, the test will vary in destructiveness, load application, and measurement type. Table 48 lists the specific tests that will be performed for various component and loading configurations.

Table 48: Specific Structural Tests to be Performed

Test Number	Component(s)	Loading Condition	Load Application	Measurement Type	Type of Test
1	Nozzle Mount	Crashing	Pneumatic Actuator	Strain Gauge	Nondestructive Load
2	Nozzle Mount	Crashing	Pneumatic Actuator	Camera	Destructive Load
3	Chassis + Nozzle Mount	Crashing	Pneumatic Actuator	Strain Gauge	Nondestructive Load
4	Chassis + Nozzle Mount	Crashing	Pneumatic Actuator	Camera	Destructive Load
5	Chassis	Weight	Weights	Camera	Nondestructive Load
6	Hoisting Hook + Chassis	Hoisting	Weight	Camera	Nondestructive Load
7	Nozzle Mount	Vibration	Shaker Table	Accelerometer	Vibration

Note that only critical, custom machined components under loads that could feasibly cause failure will be tested. As such, structural testing for the aerodynamic shell was deemed unnecessary since it is a non-critical component and its loading capability was calculated to be very high (minimum factor of safety of 10) in Section 3.3.4. Aerodynamic testing for the shell was also deemed unnecessary since drag force is very low (1.2lbs). Vibration testing for the chassis was deemed unfeasible due to access to only small (24x24") shaker tables.

As always, the safety of students and staff will be prioritized during all tests. We are already in close communication with the safety managers for our lab and will work to ensure safety protocol is met.

- *Test 1: Nozzle Mount, Nondestructive Load Tested Under Crashing Loads*

Goal: To validate the crashing case FEA analysis for the nozzle mount's loading conditions.

Method: The test schematic is shown below in figure 85 for the nozzle mount's crashing load case. The nondestructive load test is set up as follows:

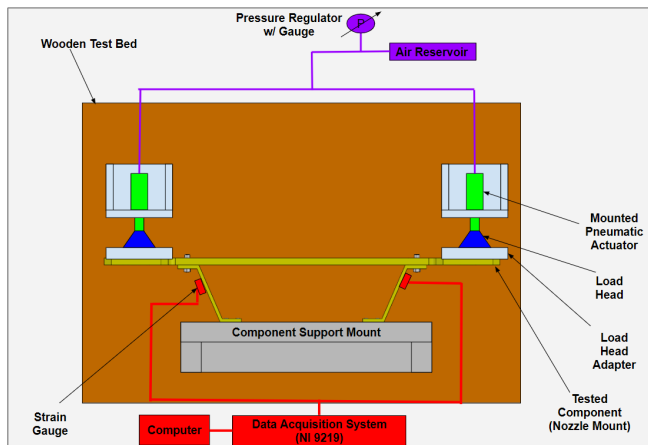


Figure 85: Nondestructive load test applied to nozzle mount (top view)

- Test Bed. A wooden test bed will be built and used for mounting all test components.
- Boundary Conditions. Boundary conditions will be set by mounting the nozzle mount to a custom test fixture as it would be on the pod. Note that removable rivets will be used instead of pop rivets to avoid the need for drilling to remove them.

- Load Application. Loads will be applied using a double acting pneumatic actuator, where actuator load output is the product of pressure and bore area $F = P * \frac{\pi*D^2}{4}$. The actuator will be supported by a custom support structure, and will be set to extend to accurately model load conditions. An air cylinder load head adapter is used to bolt directly to the nozzle mount. Using a pressure regulator and air reservoir system, actuator pressure will be increased until experimentally applied load is equal to that of the ANSYS model. Note that 3% human error is acceptable when modulating pressure.
- Data Measurement. To monitor strain during the test, an axial and transverse strain gage are placed in a half-wheatstone bridge configuration at the component's strain concentration regions as identified by ANSYS analysis. Note that strain gauges are placed at large regions of uniform strain, as opposed to singularities, such that average strain can be accurately measured (see figure 86 for demonstration) [3]. In addition, multiple wheatstone bridges can be used to measure strain at various strain concentration regions. Data acquisition will be coordinated using an NI9219 data acquisition system and LabVIEW code. Note that to reduce costs, pressure will be adjusted and recorded by hand as opposed to by pressure transducer. Thus to reduce human error, at least 3 trials will be performed for each test and the mean taken for experimental strain.

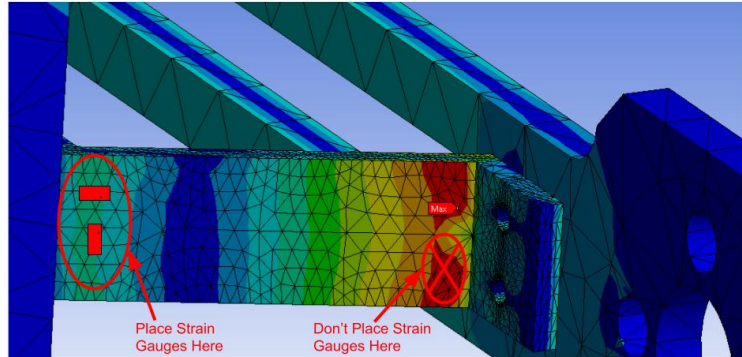


Figure 86: Proposed placement of strain gauges on nozzle mount

Expected Results: The expected results will be a mean strain value for each measured region on the nozzle mount. This experimental value will be compared with that of the corresponding FEA simulation. If measured strain is significantly larger/smaller (25%) than expected, the analysis will be promptly investigated for its accuracy. If necessary, a redesign may be warranted for a stronger version of the nozzle mount.

Additional Comments: This test simulates expected static loads and boundary conditions on the nozzle mount to validate the accuracy of the crashing case FEA analysis. The physical setup involves mounting the nozzle mount to a test fixture and applying a load using a pneumatic cylinder. Measurement will be achieved using strain gauges. The test is based on methods described in [9] for testing large aerospace structures under high dynamic flight loads. The following section provides more details.

- *Test 2: Nozzle Mount, Destructive Load Tested Under Crashing Loads*

Goal: To determine the actual load and location in which the nozzle mount fails.

Method: The setup used for the destructive test is nearly identical to that of the nondestructive test, and only vary in data measurement methods. The destructive test schematic is shown in figure 87.

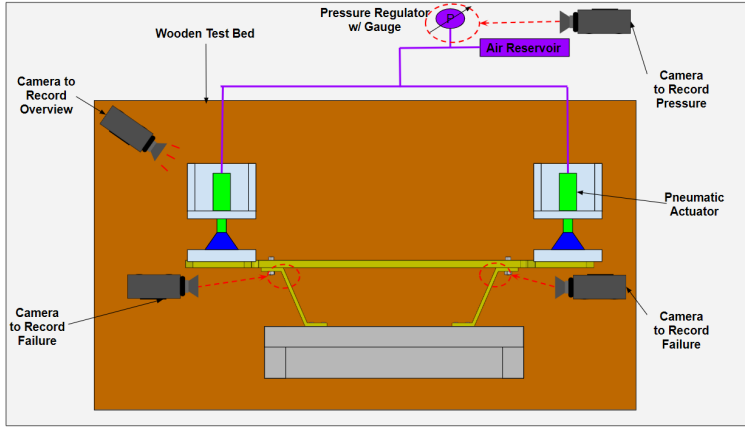


Figure 87: Destructive static load test applied to nozzle mount (top view). Note that some details of components are omitted for clarity.

The destructive test set up as follows:

- Test Bed/Boundary Conditions/Load Application. The test bed, boundary conditions, and method of load application are identical to that of the nondestructive test. Instead of only increasing loads to 100%, however, loads will be continuously increased until failure is observed.
- Data Measurement. To monitor failure during the test, high-speed cameras will be pointed at expected failure points (determined from FEA analysis), as well as the overall setup in case failure occurs at an unexpected location. In addition, a camera will be used to measure pressure of the pressure regulator gauge. Only 1 trial will be performed since the test is destructive and the part cannot be reused. Note that pressure transducers are not used to save on cost and complexity. Strain gauges are also not used to save on complexity, since the nondestructive test is already sufficient for validating ANSYS analysis.
- Load Application. Loads will be applied using a double acting pneumatic actuator, where actuator load output is the product of pressure and bore area ($F=P(D_2/4)$). The actuator will be supported by a custom support structure, and will be set to extend to accurately model load conditions. An air cylinder load head adapter is used to bolt directly to the nozzle mount. Using a pressure regulator and air reservoir system, actuator pressure will be increased until experimentally applied load is equal to that of the ANSYS model. Note that 3% human error is acceptable when modulating pressure.

Expected Results: The expected results will include video footage of nozzle clamp failure for a given actuator pressure. Specifically, failure will likely occur at the stress concentration regions of the Z-shaped bracket, as predicted by ANSYS results. Since the structure have been designed to be within SpaceX's factor of safety requirements, ultimate failure will occur no earlier than 300% the expected load. Failure will be observed as any visual signs of cracking, buckling, permanent deformation, etc. Note that it is unlikely that video footage will include yielding, as the deformation is very subtle.

Additional Comments: Having validated the FEA analysis of the nozzle mount using a non-destructive static load test, destructive testing will be used to determine the point at which it actually fails. See below for more details.

- *Test 3 and Test 4: Chassis + Nozzle Mount Load Tested For Crashing*

Goal: For test 3 and 4, tests 1 and 2 will be repeated but at the system-level. As such both the chassis the attached nozzle mount will be included for test 3 and 4. To validate the crashing case FEA analysis for the chassis-nozzle mount assembly under crashing loading conditions. Note that this test assumes that tank clamps have failed and all loading is absorbed by the nozzle mount.

Method: Note that the test setup is very similar to that of tests 1 and 2. However, a different chassis test fixture will be designed and riveted to the front face of the chassis to simulate crashing boundary conditions. Strain gauges and cameras will be adjusted to capture failure of the chassis,

as well as the strain gauge. See figure 88 for the test schematic.

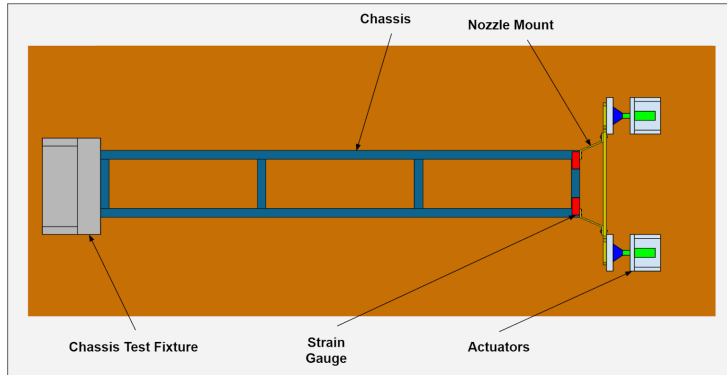


Figure 88: Chassis + Nozzle Mount Load Test Schematic (top view). For more details, see test 1 and 2.

Expected Results: Strain gauge measurements intend to validate strain predictions as observed in from Section 3.2.4. As predicted in FEA analysis, the nozzle mount is expected to fail before the chassis does. However, signs of bad welds may cause the chassis to break instead.

- *Test 5: Chassis, Proof Tested for Weight*

Goal: To prove the chassis is capable of carrying the weight of all subsystems on the pod.

Method: The chassis will be loaded with weights to observe deformation as shown in figure 89. The magnitude of weight will start at 350lb, but will increase until 1050lb is reached to achieve a demonstrated factor of safety of 3.

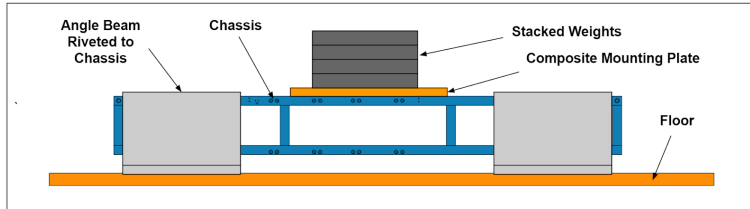


Figure 89: Chassis Proof Test for Weight Schematic

Expected Results: Photographs will be taken of the chassis' deformed structure. Note that this is a non-destructive test. However, careful investigation will still be useful in ensuring the chassis' integrity.

- *Test 6: Chassis and Hoisting Hooks, Proof Tested for Hoisting*

Goal: To prove the hoisting system used for loading/unloading via forklift is structurally sound.

Method: Per SpaceX's rule requirements, the hoisting system (spreader bar / ratchet / hoisting hooks) will be proof tested to 1.5 times the maximum expected weight load. As such, the chassis will be loaded up with weights (1.5x the weight of the pod) and hung from the second floor of the OneLoop lab using its hoisting components. See figure 90 for a visualization.

Expected Results: Photographs will be taken of the hoisted chassis. This will also serve as practice for members prior to loading/unloading at SpaceX. Special attention will be paid to potential damage to rivet nuts and holes associated with the hoisting hooks.

- *Test 7: Nozzle Mount, Vibration Testing*

Goal: To determine whether the nozzle mount's natural frequencies are reached during vibration.

Method: The nozzle mount will be mounted to a shaker table and vibrated to determine whether its resonant frequencies are excited. Vibration is increased from 0Hz to the maximum vibration frequency, as determined from testing of the propulsion system. Accelerometers are attached to

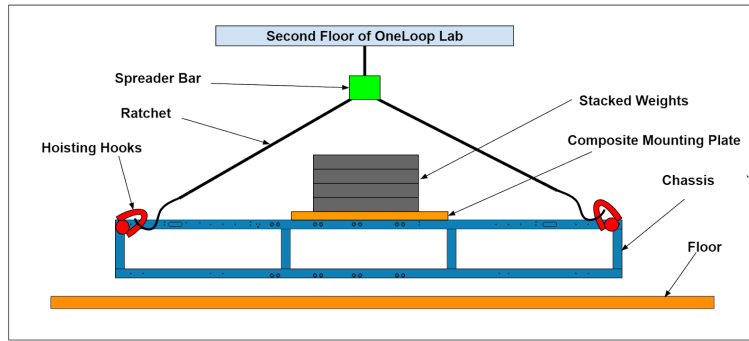


Figure 90: Hoisting Proof Test Schematic

predicted nodes of maximum vibration as determined from preliminary ANSYS analysis. Data acquisition will be coordinated by an NI 9219. The shaker table is 24x24" and is provided by the UC Davis Civil Engineering Department.

Expected Results: An accelerometer amplitude versus frequency plot will be generated using LabVIEW. Resonance, characterized by local maxima in amplitude, will be examined. If resonant frequencies are excited, the addition of vibration isolating dampeners may be required.

7.1.3 Stability Testing

System Tests

- *Clearance Test*

Goal: Confirm the clearance between the calipers and the I-beam is within specifications.

Method: The test will involve loading the stability system and attached braking system onto a pre-built I-beam. Measurements will be taken of the clearance from the brake pad to the flange of the I-beam.

Expected Results: The system will be able move freely without impacting the I-beam.

- *Static Load Testing*

Goal: Confirm the stability system maintains position when under braking and acceleration loads.

Method: A pneumatic cylinder will be used to apply a simulated braking load to the stability system, which will be fixed in place. A strain gauge will be used to ensure that the structure meets a safety factor of 2.0.

Expected Results: Based on ANSYS simulations, the stability system is expected to have a factor of safety much higher than 2.0 and will remain completely undamaged during the testing procedure.

7.1.4 Suspension Testing

This section discusses the various tests that will be performed on the completed system so as to validate results found in the structural analysis section.

Component Tests

- *Wheel Speed Test*

Goal: Confirm that the wheel can handle the 100 mph (worst case) speed required of it without failure.

Method: The wheel and its shaft will be fixed to a structure with friction fit ball bearings. A drive wheel will be placed in contact with the wheel, and spun up to the speed required to get the wheel to 100 mph, or 140 rev/s.

Expected Results: The wheel will maintain its structural integrity at high speeds.

Additional Comments: This test will be replicated in the system test for wheel speed.

- *Wheel Rolling Friction Test*

Goal: Experimentally measure the coefficient of rolling friction between the wheel and aluminum.

Method: A load will be applied to the wheel through its shaft hole. An increasing horizontal load will then be applied to the wheel until the wheel begins to move. Using the load applied and the load at which the wheel began to roll, the coefficient of rolling friction can be determined. The test will be repeated with varying applied loads to validate the calculated rolling friction value.

Expected Results: The resulting rolling friction value will lower than the calculated maximum rolling friction coefficient (Estimated in suspension design section).

- *Bearing Test*

Goal: Confirm the strength of the bearings to support the maximum expected load of 196.22 lb.

Method: The bearing will be fit with a steel shaft, and placed in a half circle cut out of aluminum. This will allow for half the bearing face to be in contact with the aluminum. A load of 196.22 lb will then be applied to each end of the steel shaft. The bearing will be observed to see if the bearing deforms.

Expected Results: The bearings will maintain their structural integrity and continue to operate normally.

- *Coilover Test*

Goal: Confirm the spring rate and find the dampening rate range for the coilover.

Method: To confirm the spring rate of the coilover, it will be suspended, with varying weights hung from the coilover. The extension of the coilover from its rest length will be used to find the spring rate. To find the dampening rate range, the coilover will again be hung, with weights attached to the other end. As the dampening rate is controlled by a dial on the coilover, for each case, the dial will be set to a minimum and maximum, allowing for measurement of the two extreme values. When the weights are released, the oscillations of the weight will be recorded, allowing for derivation of the damping rate range.

Expected Results: The spring rate of the coilover will be confirmed as being its predefined value. The dampening rate test will yield upper and lower bounds for the dampening rates of the coilover.

System Tests

- *Weight Test*

Goal: Confirm that the system can carry the expected load of 87.5 lb, as well as twice the expected load, 175 lb.

Method: The test will be done two ways; one, the testing of each individual system, and two, all four systems attached to the chassis. For the first test, one system will be fixed to the chassis with rivets, then flipped upside down. Then, the expected load and twice the expected load will be applied to the wheel. The loads will be held for an extended period of time, so as to demonstrate that the system can maintain its structural integrity. The second test will be with all four system fixed to the chassis with rivets. The chassis will then be loaded with weight to mimic the 350 lb weight that is expected, as well as 700 lb, twice the expected load. The loads will be held for an extended period of time, so as to demonstrate that the systems can maintain their structural integrity.

Expected Results: The system will be able to carry the expected and twice the expected load without deformation that interferes with the system's operations.

- *Bump Test*

Goal: Model the dynamics of the system encountering a bump at the expected 125 mph speed.

Method: As it isn't possible to propel the system to the expected pod speed, the system will be run over the expected bump at a lower speed. To compensate for the lower speed, the chassis

will be loaded with a greater weight than the 350 lb the pod is expected to weigh. By creating a dynamic model of the bump at the low speed using ANSYS, and manipulating that model to match what is observed in the physical test, the model can be scaled up to the expected 125 mph speed and decrease the weight to the expected pod weight of 350 lb.

Expected Results: The resulting model will allow for a prediction as to how the system interacts with the bump at the expected speed.

- *Motor Test*

Goal: Display that the system's motor can overcome the static friction exerted by the track on the pod, and propel the pod the remaining distance down the track after the run has completed.

Method: The chassis will be loaded with the expected weight of 350 lb, and the motor will be run at various torques. Should the system overcome the static friction, the weight applied to the chassis will increase incrementally, until the motors can no longer propel the pod. The pod will be placed on an aluminum surface, so as to emulate the track environment.

Expected Results: The motor's will be able to overcome the static friction, and will yield an upper limit to the weight the motor's can propel.

- *Thermal Test*

Goal: Observe the propagation of heat from the motor in a vacuum environment, and if the heat compromises the system's structural integrity.

Method: Temperature sensors will be placed at multiple points throughout the system, such as the motor, the triangular pivot the motor is attached too, the wheel, the wheel shaft, and the side plate. The system will then be placed in a vacuum chamber on the UC Davis campus, so as to simulate the near vacuum the motors will be run within. Based off of the results from the Motor Test and the remain distance the motor will act to remove the pod from the tube, the motors will be run for the required length of time. Should the system not show sign of compromised structural integrity, the test will be repeated, for twice the length of the previous test. The temperature sensors will record the change in temperature at various points due to the motor, which allows for an assessment of the structural integrity of the various parts at the elevated temperature.

Expected Results: The heat generated by the motor will not affect the structural integrity or operations of the system.

- *Wheel Speed Test*

Goal: Confirm that the wheel will maintain its structural integrity whilst rotating at 175 rev/s.

Method: The system's wheel will be placed in contact with another wheel that will be spun to have a tangential velocity of 100 mph. The spinning wheel will be powered by a motor. With the system's wheel spun up to 175 rev/s, the wheel will be observed to see if any structural failures occur; that the wheel will remain one cohesive object, and the wheel's deformation does not impact the system's operations.

Expected Results: The wheel will maintain its structural integrity, with minimal deformation that will not interfere with the system's operations.

Additional Comments: This test is nearly identical to the component wheel speed test, except this test is for the entire system, rather than just the wheel.

- *Vibration Test*

Goal: Find the frequency of oscillation the suspension system will impart on the pod during the run.

Method: The four suspension systems will be mounted to the chassis, and the chassis will be load with enough weight to simulate its total 350 lb. The Mechanical and Aerospace Engineering Department has a shaker table available for testing. The pod will be shaken vertically with various frequencies.

Expected Results: The various shaking cases will provide us with estimations as to potentially dangerous frequencies. Should the dangerous frequencies match with projected frequencies experi-

enced during the run, the suspension system's dampening and spring rates will be modified.

7.1.5 Propulsion Testing

Table 49: Propulsion Testing Overview

Component Testing	Systems Testing
C1. Air-Operated Valve(s)	S1. Hydrostatic 1.5X Proof and Leak Test
A. Functionality	Outsource full system hydrostatic testing to Consolidated Labs
B. Pressure drop	Certify all components are safe at 1.5x MAWP
C. Response time	
C2. Pressure Regulator(s)	S2. Single Thruster Cold-Gas
A. Configure outlet pressure	A. Thrust
B. Measure and record pressure drop	B. Vibration
C. Validate/improve thermodynamic mode	C. Configure optimal set pressure
C3. Relief Valve(s)	S3. Single Thruster Tri-Gas
A. Configure set pressure	A. Thrust
B. Functionality	B. Vibration
	C. Burn analysis
	D. Establish expected operating conditions
C4. Catalyst Bed Insert (N2 Test)	S4. Double Thruster Tri-Gas
A. Structural Test	A. Thrust
B. Pressure drop	B. Vibration
C. Mass Flow Rate	C. Alignment
	D. Configure regulators to match thrust

Notes on Testing Safety and Testing Practice

The following is an excerpt from *Advanced NSTS Propulsion System Verification Study Final Report*, published by Rockwell International and found in NASA archives [21].

by using actual data from a modern day, current operational vehicle. Maturity is a prerequisite for a successful flight program, thus any new development/verification program may be expected to encounter similar experiences. Conclusions to assist in subsequent program developments are:

- Propulsion system complexity precludes total dependency on analytical methods for establishing flight worthiness.
- Propulsion system maturity results from rigorous system testing.
- Rigorous testing involves significant numbers of system tests and long duration tests.
- High risk to test vehicle/facility are associated with the testing.
- Flight schedules established for programs without adequate propulsion system testing may be relatively meaningless.
- Delay of propulsion system testing until vehicle/engine hardware achieve some minimal maturity may be beneficial for reducing risk, cost, and test time. Launch site hardware and software requirements must be properly considered.
- Propulsion system testing should be considered exceptionally high risk without inclusion of safety enhancement features.

Figure 91: Propulsion system development conclusions

This source has been very useful in guiding our team on propulsion system design. From these conclusions, two main takeaways are extracted:

1. Safety comes first.

Due to the risks associated with propulsion system testing, similar safety practices to those described above will be utilized during testing. For system testing in particular, the evacuation area is useful in gauging how far away an individual must stand from the static fire test stand while in operation. Furthermore, all system tests will be designed and executed with guidance from experienced University faculty such as Professor and astronaut Stephen K. Robinson and Professor Case Van Dam. The total stored energy considering all tanks in use is equivalent to 0.29 lb of TNT. 5 lbs of TNT is equivalent to a 850 ft standing distance so an appropriate standing distance for 0.29 lb of TNT is 204 ft [14].

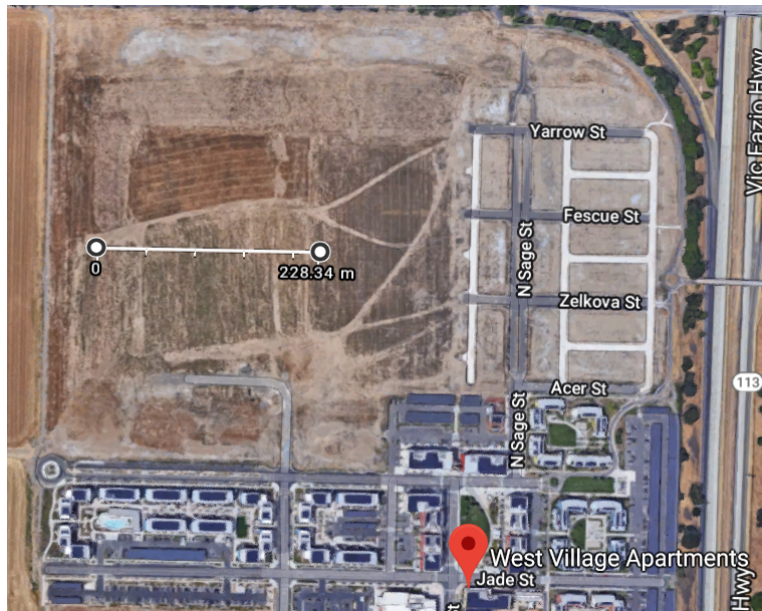


Figure 92: Proposed testing area with 748 feet radius clearance

This largest open area in UC Davis for this test to occur is proposed above. It meets the requirements standing distance calculated above. For smaller component tests, shielding from the observer and the system will occur with Acrylic (7.54 MPa tensile strength) sheets.

2. Iterations will be necessary, and efficiency is key.

Technology and analytical methods have come a long way since this report was published. However, there is still a lot to be learned from the first bullet point listed. Anticipating the need for multiple iterations and rigorous testing in order to establish our system's flight readiness, our team will take extra measures to ensure efficiency during the testing process. Namely, extensive testing journals that document setups, sensors, response times, component settings, and results will be kept for all propulsion tests, similar to the "Test Program" documents listed in the Rockwell report [21].

Component Tests

- *C1: Air Operated Valve(s) A-1, A-2, A-3, A-4, A-5*

Goal:

- (A) Test functionality of air-operated valves and their low-pressure control
- (B) Record pressure drop across a single air-operated valve
- (C) Record response time of air-operated valve under race conditions

Method: The test setup above will be assembled and each air-operated valve will be tested in place of A-X. A single COPV tank containing N2 gas pressurized to 4500 PSI will be used. Tri-gas propellant is not necessary since no catalyst is used and Nitrogen is cheaper. Also, M-4 will be opened prior to test start so the test can be conducted from a safe distance by remotely opening S-1.

At the start of the test, M-3 will be opened to see if A-X can hold a differential pressure of 4500

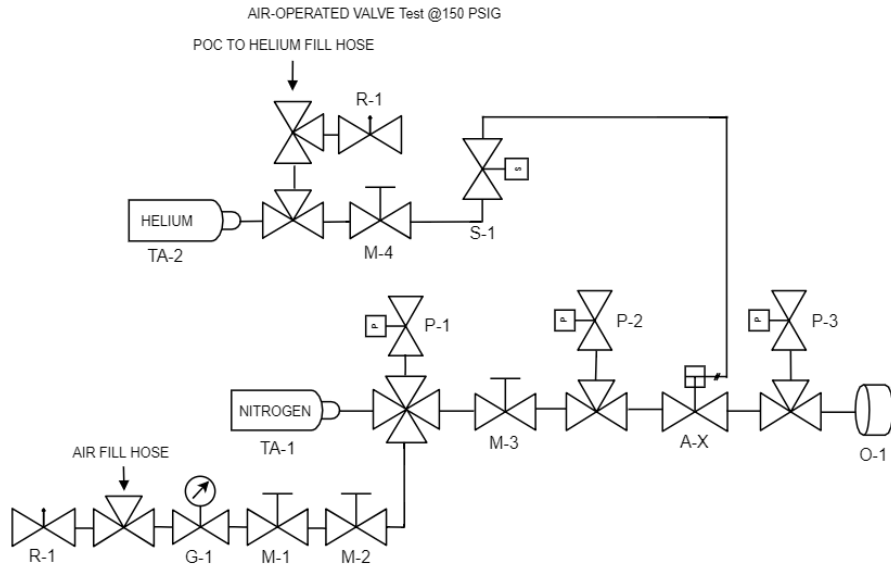


Figure 93: Test Setup for Air-Operated Valve

PSIG. Then, S-1 will be opened to test the functionality of the low pressure control system, accomplishing Goal A. If P-2 and P-3 confirm that A-X has successfully opened, then the difference between their readings will be recorded along with how long it took A-X to open, accomplishing Goals B and C.

Expected Results: The air-operated valve opens when the solenoid valve is activated. There will be minimal pressure drop across the valve. The response time will be less than 5 seconds.

Safety Comments In the event that A-X cannot hold the differential pressure, gas would pass through O-1, restricting the flow with a Cv of 0.03. Even with this precaution, all test personnel will stand at least 10 feet away from the test setup during the test.

- *C2: Pressure Regulator(s) Q-1, Q-2*

Goal:

- Configure the outlet pressure of Q-1 and Q-2
- Measure and record pressure drop
- Validate/improve thermodynamic model to assist in nozzle design

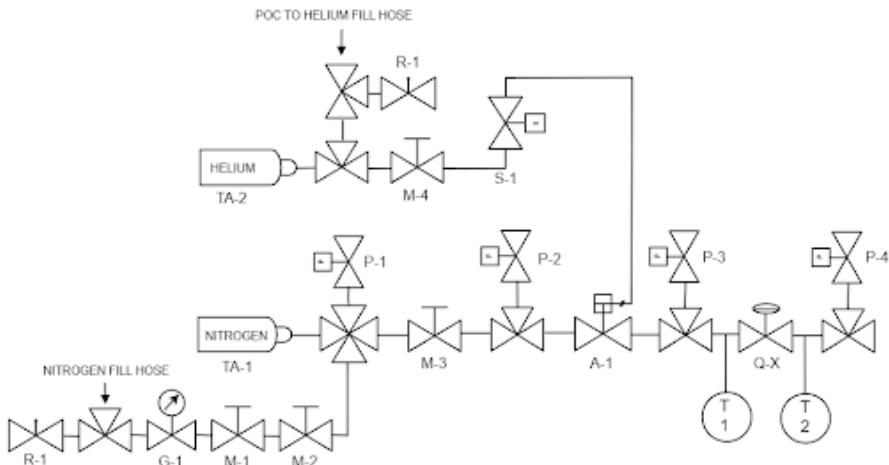


Figure 94: Test Setup for Pressure Regulator

Method: The test setup above will be assembled and each flow regulator will be tested in place of Q-X. As before, tri-gas propellant is not necessary for this test since no catalyst is used. M-4 will

be opened prior to test start so the test can be conducted from a safe distance by opening S-1. Q-X will be set to 550 PSI. In order, M-3 and A-1 will be opened. Flow pressure will be recorded before and after Q-X using P-3 and P-4, accomplishing Goal B. If P-4 reads an off-nominal value, Q-X will be manually adjusted until P-4 reads 500 PSI (10% drop). This will accomplish Goal A. Furthermore, P-3 and P4 as well as T-1 and T-2 will record change in temperature and pressure across Q-X accomplishing Goal C. The results of these tests will allow for empirical data to replace the curves seen in Figure 44, after which the same nozzle design process can be used to optimize the nozzle.

Expected Results: The pressure regulator will output 500 PSI and the gas temperature and pressure curves will behave similarly to Figure 44.

- *C3: Relief Valve(s) R-1,R-2*

Goal:

- Configure the outlet pressure of relief valves
- Test functionality of relief valves.

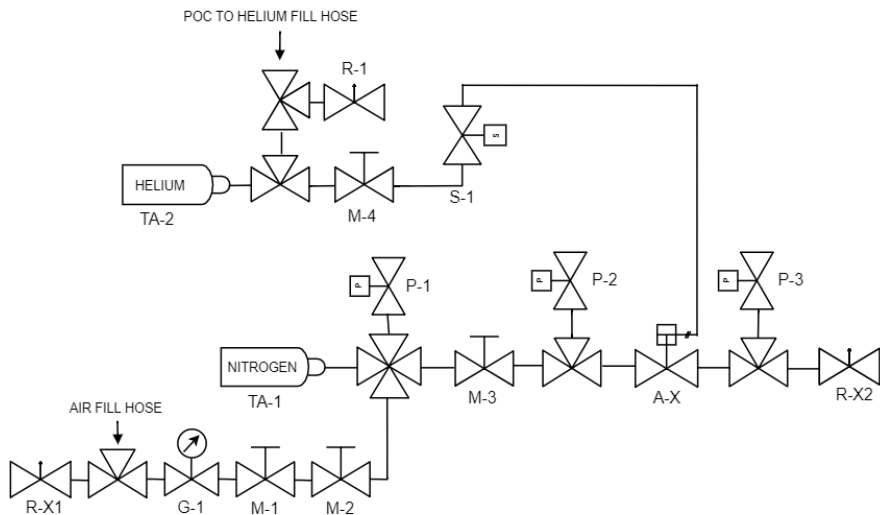


Figure 95: Test Setup for Relief Valve Configuration and Functionality

Method: The test setup above will be assembled and the same relief valve will be tested first at R-1X during filing and then at R-X2 during testing. The same tank specifications as the last test will be implemented. Tri-gas is again unnecessary given no catalyst is involved.

First, filling will proceed using the fill station previously designed. Once the tank has been filled, pressure will be slowly increased until R-X1 is activated, accomplishing Goal A. After enough gas has been relieved that the system is back to 4500 PSI, M-1 and M-2 will be closed. Then, the relief valve being tested will be removed from the R-X1 location and placed at the R-X2 location. Lastly, M-4 will be opened prior to test start so the test can be conducted from a safe distance by opening S-1.

A-1 will be activated opened, allowing R-X2 to prove that it can withstand 4500 PSI without relieving, accomplishing goal B.

Expected Results: Relief valves will be configured to their appropriate set pressures and be able to handle MADP/MAWP.

- *C4: Catalyst Bed Insert*

Goal:

- Test structural integrity of the catalyst bed insert at race conditions (550 PSI, 745 K)
- Record pressure drop

(C) Record temperature drop

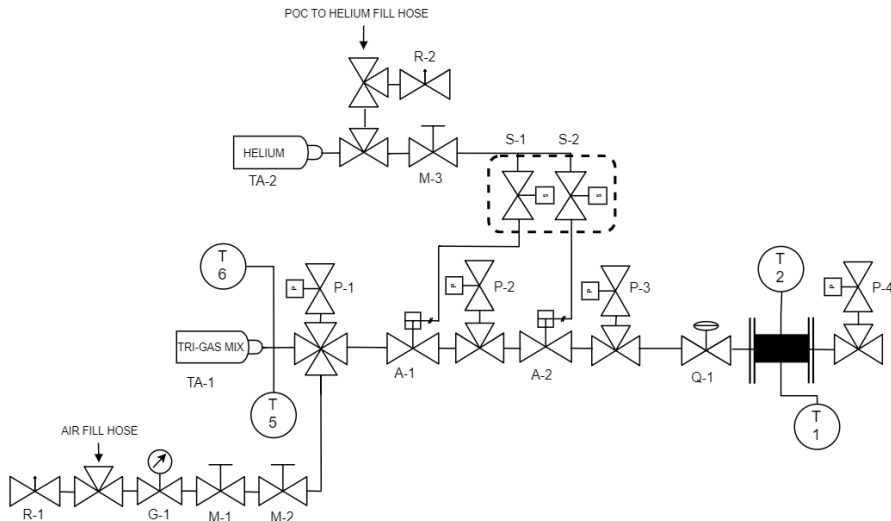


Figure 96: Test Setup for Catalyst Bed

Method: The test setup above will be assembled and each catalyst bed insert will be tested. The catalyst bed insert will be inserted into a flange mount and heated to 900 °F using the auxiliary heating station. No catalysts will be inside the bed for this test. S-1 and S-2 will be activated, allowing A-1 and A-2 to open. For this first test, Nitrogen regulated to 550 PSI using Q-1 will be used. The system will be monitored to make sure the insert does not structurally fail at that temperature, accomplishing Goal A.

Following the structural test, the insert will be filled with catalyst material and tri-gas will be used in place of Nitrogen, using the same setup. P-1 through P-4 will measure temperature characteristics while T-1, T-2, T-5, and T-6 collect temperature data, all of which will help inform a better thermodynamic model and accomplish goals B and C.

Expected Results: The catalyst bed insert will not structurally fail. Some plastic deformation may be seen on the stainless steel mesh, but the overall structure should be unaffected.

System Tests

System testing will occur in the order shown below. Each experiment will either test additional factors or serve as proof of concept to build up to the full double tri-gas thruster system test.

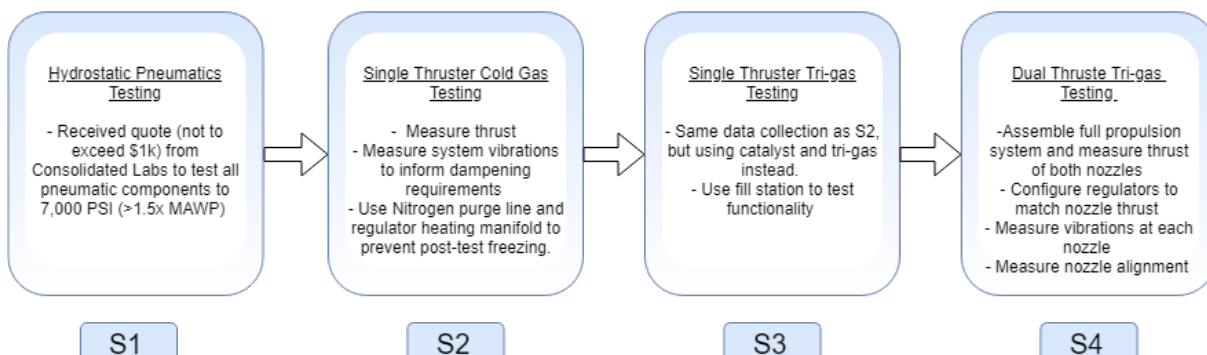


Figure 97: System Test Sequence and Objectives

- **S1: Hydrostatic Testing**

Leak and 1.5x MAWP proof tests will be conducted on system level prior to testing. Consolidated Labs has quoted us for this service, and we will be working with them to certify our system as high-pressure safe. All pneumatic components and piping upstream of the pressure regulators will

be tested at a pressure of 7,000 PSI to satisfy the 1.5x MAWP requirement. For components downstream of the regulator, which include pipe and the nozzle, this 1.5x proof testing will need to occur using pressurized gas at 800 PSI, since the open ended nozzle cannot be hydrostatically tested. This test will be completed by the end of May, as detailed in Section 2.7.

- *S2: Single Thruster Cold-Gas*

Goal:

- (A) Record thrust produced by system
- (B) Monitor system vibrations
- (C) Monitor thermodynamic state of system
- (D) Prevent post-experiment freezing damage

Method: One thruster with an aluminum nozzle designed for expansion to atmospheric pressure will be tested. The test setup in Figures /refPropSysTest1 and /refPropSysTest2 will be assembled in order to collect thrust data and ensure safe operation (see polycarbonate enclosure), accomplishing Goal A.

For this test, two COPV tanks containing Nitrogen gas will be pressurized at 4500 PSI and the test nozzle will be attached to the end of the fully-assembled system as seen in the P&ID. Accelerometers will be placed at the nozzle, accomplishing Goal B. Goal B is critical, as system vibrations could result in structural failures when traveling high speeds. This test will help us diagnose any potential system vibrations and mitigate them before problems can occur.

Pressure transducers and thermocouples will be placed before and after every major component in the system, accomplishing Goal C. The flow regulator will be set to 550 PSI, and the test will take place once the necessary valves are opened.

This will be a long duration test that exhausts all stored gas in the tank. As such, we anticipate that the system will get very cold. Therefore, once experimentation has finished, a smaller compressed cylinder containing Nitrogen Gas will purge the system, accomplishing Goal D. This will maintain a positive pressure differential preventing gas from flowing back into the Nozzle and freezing components. To prevent freezing of the high-pressure regulators, warm water will be fed through their body heating manifolds. This will prevent the regulators from sustaining temperature-related damage during testing.

Expected Results: The system will produce less than 200N, since it is a purely cold gas thruster. Vibrations will be minimal and manageable with dampeners.

- *S3: Single Thruster Tri-Gas*

Goals:

- (A) Record thrust produced by system
- (B) Monitor system vibrations
- (C) Monitor thermodynamic state of system
- (D) Prevent post-experiment freezing damage

Method: The test setup will be identical to test S2, but with a stainless steel tri-gas nozzle designed for atmospheric pressure and the packed catalyst bed insert as opposed to the cold gas nozzle.

The same Nitrogen purge method as before will be used to prevent freezing.

Expected Results: The system will produce a thrust force of around 270 N. Vibrations will be minimal and manageable with dampeners.

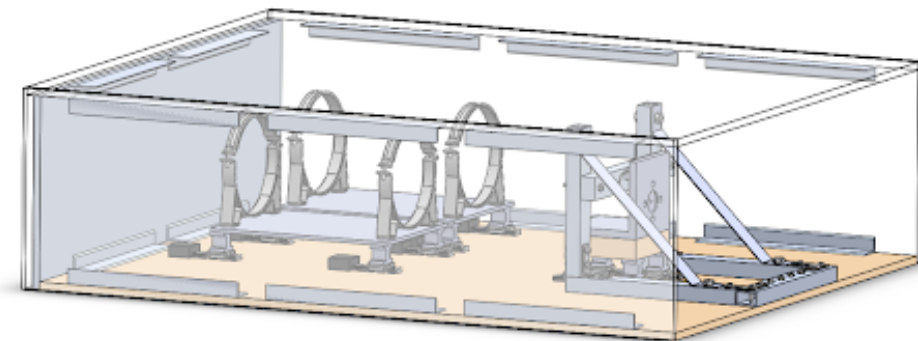


Figure 98: Test Stand for System Testing

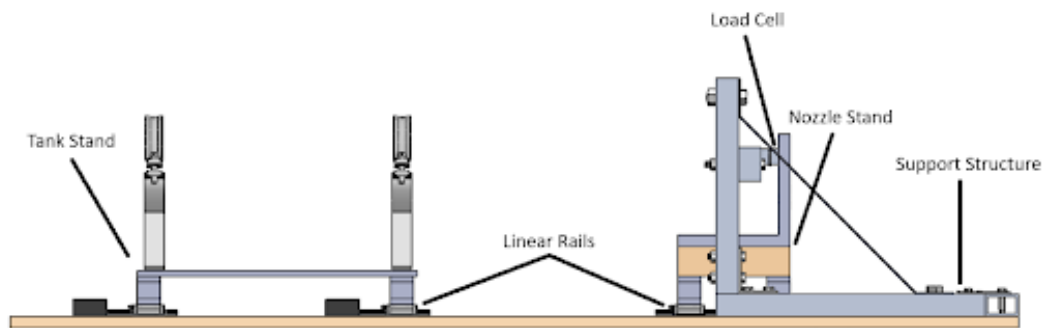


Figure 99: Test Stand for System Testing

S4: Dual Thruster Tri-Gas

Goal:

- (A) Configure nozzles to produce equal thrust
- (B) Monitor system vibrations
- (C) Measure relative alignment of nozzles

Method: The test setup will consist of two of the test stands previously pictured. The full propulsion system will be assembled for this test, allowing the team to test the fill station capabilities, preheating station capabilities, and relief capabilities if necessary.

The same Nitrogen purge method as before will be used to prevent freezing after the test is completed. Vibrations will be monitored using the same methods and for the same purposes as tests S2 and S3, satisfying Goal B.

The test will begin after the tanks have been filled using the fill station, M-5 and M-6 have been closed, and M-7 and M-8 have been opened. At this point, A-1 through A-4 will be opened via S-1 through S-4 from a safe distance to start the thrusters. If the nozzles produce unequal thrust, the test will stop immediately, the regulators will be adjusted to bring the thrust numbers closer together, and the thrusters will be activated again. This process will repeat until both nozzles produce equal thrust, accomplishing Goal A.

Prior to these tests, the nozzles' alignments relative to each other and a designated flat surface will be measured using angle cubes. If the nozzles are misaligned, the mounting structures will be modified to align them. No thrust testing will occur until the thrusters are aligned.

Expected Results: The system will produce a thrust force of 270 N per nozzle when both regulators are set to an outlet pressure of 550 PSI. Vibrations will be minimal and manageable with dampeners. The nozzles will be aligned with each other as determined by the angle cube, ensuring no large moments act on the pod.

7.1.6 Braking Testing

For all braking tests, the response time of the system will be measured to collect data and determine the distance the pod would travel between sending the brake command and a full stop.

Dynamic testing of many of the components as well as the full braking system will be performed with a custom brake dynamometer pictured below in Figure 100. In this setup, the axle will rotate freely on multiple sets of high weight-capacity bearings. One of the calipers from the brake subsystem will be positioned around the brake disk and rigidly enforced with steel struts. After the rotary motor brings the axle up to speed, it will disengage as the brake caliper is activated. Using an array of sensors, the bench will allow testers to determine the total amount of kinetic energy dissipated by the brakes, the temperature increase with time of the brake disk, and the total torque supplied. This test system will be used for a variety of tests as detailed below.

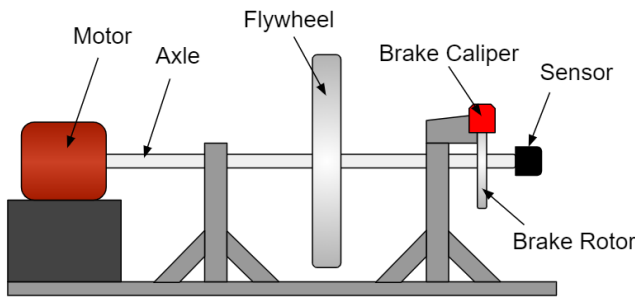


Figure 100: Brake Dynamometer

Component Tests

- *Calipers:* The Calipers will be tested individually to ensure they actuate properly. This will be accomplished using a simplified pneumatic circuit and low-pressure airflow. We expect all calipers to actuate properly, proving they are in working condition. We will also test the calipers to determine the minimum PSI required to actuate.
- *Brake Pads:* Two tests will be performed on the brake pads. The first is to ensure the hardness of the pads is less than that of the track. To accomplish this test we will use a Brinell's Hardness Testing Machine and compare the tested value to that of 6061-Aluminum. We expect this test to conclusively prove the brake pads will not cause damage to the I-Beam. The second test we will perform is to ensure the brake pads wear away rather than slide when actuating on aluminum. To test this we will utilize the dynamometer setup detailed earlier within this section. This test should also prove that no damage will be caused when the brake pads contact the I-Beam.
- *Valves:* All valves will be tested to ensure they open and close properly whether they are manual or computer controlled. This will be accomplished by utilizing a simplified pneumatic circuit and low PSI airflow.
- *Pressure Sensors:* All pressure sensors will be tested to ensure they provide consistent and accurate results for a known pressure source. This test will be accomplished using a simple pneumatic circuit with constant pressure. This test will show that our sensors are working properly and providing accurate results when used for overall system testing.
- *Pipe:* All pipe which is cut to length and threaded by our team will be tested at 1.5 times its working pressure for 5 minutes as detailed within the official competition rules. This will ensure that the tubing we use was properly manufactured and installed.

System Tests

The following tests will be performed on the entire system.

- *Test 1: Leak Testing*

Goal: Prove system has no leaks after system is completely assembly.

Method: Utilize hydrostatic test pump to pressurize system to 60% of working pressure and visually inspect it for leaks at all joints and connections.

Expected Results: We expect all systems to be connected properly and if a leak is detected we will replace or repair the connection or part and then repeat the test.

- *Test 2: Nominal System Test*

Goal: Test system operation under nominal conditions.

Method: Connect a single system to the dynamometer setup detailed above. Run test with 100 PSI input pressure and monitor results.

Expected Results: Our first expected result is the amount of time it takes from a signal being sent to braking initiation. We will test this parameter several times and then work this into our expected braking time and distance. Our next testing parameter is the force exerted by the caliper on the dynamometer. We expect this force to match the specifications detailed by the manufacturer of 6.4N/PSI. Using this information we can further refine our braking distance and time based off of our experimental data. The third parameter we will be testing is the heat generated on both the dynamometer and the caliper during braking operation. We expect to be able to use this information to better establish a temperature profile for our caliper system.

- *Test 3: Off-Nominal System Test - Power Loss*

Goal: Ensure brakes perform as expected in case of power loss.

Method: Connect a single caliper to the dynamometer setup detailed above. Run test with 100 PSI input pressure, turn off power to normally open valves, and monitor results.

Expected Results: We expect to see identical results to that of the test for a nominal system with the caliper actuating immediately upon power loss because of the normally open valves.

- *Test 4: Controls Failure Detection and Response*

Goal: Test controller responses to controlled inputs with both systems connected.

Method: We will manually control the inputs to the sensors connected to our PLC in order to test its responses and ensure it is acting as expected for all scenarios. We will pull these scenarios directly from the FMECA analysis we performed.

Expected Results: We expect the controller to perform as detailed by our state diagram. In addition we should be able to compare the controller state to our FMECA analysis and receive the correct state for the given input.

The second failure case is a loss of a monitor. This test requires collaboration with the controls team and will be set up by having two of the monitors connected to a different system but being seen by controls as being part of the original system. Varying the pressure in the second system will determine if the monitor responses have been accurately included into the code and will only trigger braking when a loss of a monitor affects reliable visibility into the necessary data (Pressure, Temperature).

- *Test 5: System Vacuum Test*

Goal: Ensure brakes perform as expected in vacuum conditions.

Method: Place system into vacuum chamber and depressurize. Monitor system and then actuate brakes.

Expected Results: We expect to see performance identical to that at atmospheric pressure.

7.1.7 Controls Testing

- *Pod state machine test*

Goal: To test the behavior of state machine before building the system.

Method: The state machine will be simulated using Rockwell Studio 5000®. This software allows us to simulate a PLC and observe its behavior. Three types of runs will be simulated:

1. Nominal run - all systems will be fully functional
2. Sick run - some systems will be given ‘sick’ status
3. Shutdown run - system failure will be anticipated

In the simulation, sensor data will be manipulated such that all transitions occur, including transitions which will abort the run. This step is crucial as every sensor plays a part in the control logic. We will also ensure that each state action occurs in the right order and that the state variables generate expected values.

Expected Results: The designed state machine will act in accordance to the intended design once simulated. All undesired events are evaluated to prevent their occurrence during the actual run.

- *Vacuum test*

Goal: To test the sensors and the control unit in a vacuum environment to verify that they operate correctly in such conditions.

Method: First, the sensors and control unit will be operated in an air-based environment and then be operated in a vacuum environment. The data collected from both the environments will be compared to check if the behavior is similar or not. The control unit will run a sample state machine and log the events which will then be analyzed to see if it functioned as expected.

Expected Results: The sensors and control unit will work in a vacuum environment as they would in an air-based environment.

Comments: The UC Davis Department of Geology gave us permission to use their vacuum chamber for conducting this test.

- *Vibration test for Mounted Power and Controls Assembly*

Goal: To determine whether the mounted powers and controls assembly will continue to function under vibration.

Method: Similar to test 7 in Section 7.1.2, the power and controls assembly attached to its mounting plate will be attached to a shaker table and vibrated at maximum expected frequency.

Expected Results: A mechanical check will be performed on all fittings. In addition, all controls and powers units will be tested for functionality to ensure that soldered connections have not been severed.

7.2 Full Pod Testing

In addition to subsystem testing, five full pod tests are currently scheduled, as seen in the production schedule section of this report. We have allotted four weeks for these tests, allowing extra time to implement any changes deemed to be necessary during these tests. At this time, these tests have not been thoroughly designed, but their overall structure has been determined.

Test 1: Full Pod Static Thruster Test

In this test, the fully assembled pod will be held fixed to a strong mounting surface. The ready to launch procedure detailed in Section 8 will be practiced and performed prior to this test. After the checklist has been completed, the controls system will be used to manually run the pod through the states it would go through during the competition. This will include firing the thrusters and ensuring that they behave nominally throughout the test.

Test 2: Full Braking Functionality Check

In order to ensure that the braking systems are correctly integrated with the rest of the pod, the pod will be aligned with a 10-foot I-beam that our team manufactured last year (this I-beam has the same dimensions as the one on the track). After properly aligning the entire pod over the I-beam, the brakes will be rapidly actuated and then checked to ensure that they interface with the I-beam in a manner

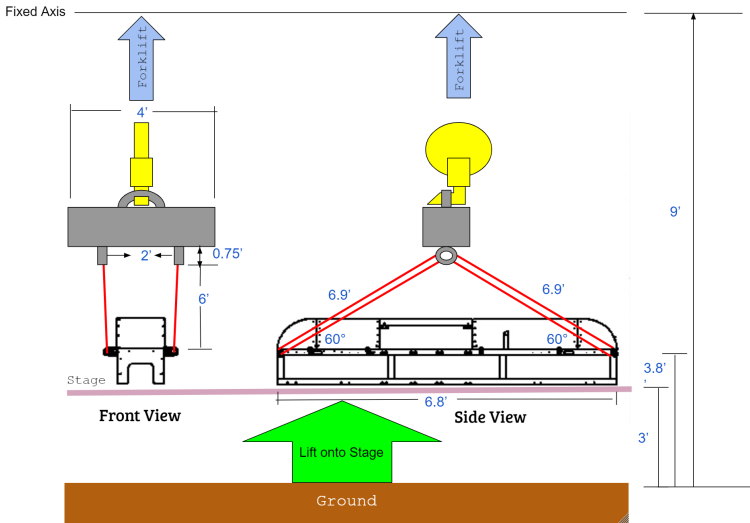


Figure 101: Loading and Unloading Schematic

that is consistent with the keep-out zones designated by SpaceX.

Test 3: Full Pod Alignment Check

In a method similar to full pod test 2, the fully assembled pod will be placed on the I-beam using the stability system to guide it. The pod will then be pushed forward and backward to determine if there are any alignment issues that would result in significant friction resistance to the sliding motion.

Test 4: Full Pod Controls Functionality test

Much like the state machine test detailed in Section 7.1.7, the controls system will be fed a dataset meant to test its response to different run scenarios. However, this test will be run on the actual pod, meaning that the controls system will respond by opening and closing valves, performing sensor data calculations, and diagnosing the state of the entire system.

Test 5: Full Pod Thermo-Vacuum Test at NTS

With the help of NTS, a test plan will be developed to test the functionality of the entire pod at vacuum. This will include checking that sensors respond accurately to thermal environment changes, ensuring valves open and close with quick enough response times, and that the power and controls systems do not fail under this pressure. Furthermore, a post-test report will be written by NTS Test Engineers to certify that our system operates safely at 0.125 PSI.

8 Loading and Unloading Plan

Moving the Pod

To lift the pod onto the staging area, SpaceX' forklift will be utilized. Note that a spreader bar will be attached to the forklift and used in conjunction with ratchets and hoisting hooks. See figure 101 for visualization. Once on the stage, the pod must be loaded into the tube. Since the only systems that require tight tolerances with the I-beam are the stability and braking systems, the pod can be easily loaded. Once the pod is in front of the Hyperloop, the the stability system, which has the braking system bolted to it, will be fed around the I-beam by lifting it up by hand. The chassis is designed to provide easy access to both the front and rear stability system to allow for manual lifting.

For removing the pod, it will be moved to the edge of the I-beam by the wheels and then manually pulled out while holding the front stability system to ensure there is not excess torque on the front and rear stability system mount.

Pre-launch and Functional Checks

Once the pod has been moved to the staging area, but before the power and control subsystems have been activated, both the pneumatic tanks and the propulsion tanks will be filled.

After pressure vessels have been filled, controls and power subsystems must be powered on in order to allow the braking subsystem to be operational. During filling of pressure vessels a ball valve in the braking pneumatic system will be closed in order to inhibit the air pressure from causing the brakes to actuate. Since normally-open valves require power to close, the power subsystem must be active in order to open the ball valve. The propulsion subsystem does not require power before entering the Hyperloop because their valve are normally-closed.

During the loading stage, both mechanical switches for the main battery pack and backup pack will be turned on while the secondary pack's connector wires must be connected, and the relay is OFF by default. Through the PLC and microcontroller, a system check will be performed for all three modules. This makes sure the modules are balanced and under normal operating temperature with an expected power inrush of 850mA for 125ms.

In the event of current draw that is too little, indicated by PLC not powering on, first use a multimeter to check the battery pack voltages. If the batteries are nominal, then recheck the connections to the various devices to insure they are secure.

In the event of current draw that is too high, the BMSs will automatically shut off the current to prevent or halt damage to components. If the BMS fails or the overcurrent is within the packs, fuses will blow, protecting the cells from damage.

The pod will then be moved into the Hyperloop and depressurized. Pre-launch checks will be performed for necessary monitors in each subsystem to ensure each system is performing nominally.

Expected Pre-Launch Monitor Reading

The table below details the values that monitors will be to pass through pre-launch checks. These values will be refined in the testing phase and some will be determined in testing and are marked TBD. The PLC will monitor these values and send them through telemetry.

Table 50: Pre-Launch Monitor Checks

Monitor	Description	Subsystem	Expected Value	Expected Deviation
BPT-4,BPT-9	Tank Pressure Transducer (Before Test)	Braking	200 PSI	+/- 5%
BTC-0,BTC-1	Tank Temperature Sensor (Before Test)	Braking	TBD	
BPT-0 and BPT-1, BPT-5 and BPT-6	Post-Regulation Pressure Sensors	Braking	100 PSI	- 5%
BPT-2 and BPT-3, BPT-7 and BPT-8	Caliper Pressure Sensor (Before Test)	Braking	14.7 PSI	+/- 5%
	Main Battery Voltage	Power	26.7V	+/- 10.1%
	Secondary Battery Voltage	Power	15.3V	+/- 3.6%
	Secondary Battery Current	Power	<6A	

Table 50: Pre-Launch Monitor Checks

Monitor	Description	Subsystem	Expected Value	Expected Deviation
PPV-0	Pressure Sensor Post Valve A-1	Propulsion	0.125 PSI	+/- 5%
PPV-1	Pressure Sensor Post Valve A-2	Propulsion	0.125 PSI	+/- 5%
PPV-2	Pressure Sensor Post Valve A-3	Propulsion	0.125 PSI	+/- 5%
PPV-3	Pressure Sensor Post Valve A-4	Propulsion	0.125 PSI	+/- 5%
PPV-4	Tanks TA-3,TA-4 Pressure Sensor	Propulsion	4500 PSI	+/- 5%
PPV-5	Tanks TA-1,TA-2 Pressure Sensor	Propulsion	4500 PSI	+/- 5%
PPV-6	Tank TA-5 Pressure Sensor	Propulsion	110 PSI	+/- 5%
PT0	Temperature of Catalyst Bed # 1 Sensor	Propulsion	TBD	
PT1	Temperature of Catalyst Bed # 1 Redundant Sensor	Propulsion	TBD	
PT2	Temperature of Catalyst Bed # 2 Sensor	Propulsion	TBD	
PT3	Temperature of Catalyst Bed # 2 Redundant Sensor	Propulsion	TBD	
PT4	Temperature of TA-1,TA-2 Sensor	Propulsion	TBD	
PT5	Temperature of TA-1,TA-2 Redundant Sensor	Propulsion	TBD	
PT6	Temperature of TA-3,TA-4 Sensor	Propulsion	TBD	
PT7	Temperature of TA-3,TA-4 Redundant Sensor	Propulsion	TBD	
PT8	Temperature of TA-5	Propulsion	TBD	

Pre-Launch Test

In addition to checking monitors, a full cycle of the brakes will be preformed to ensure all the valves and calipers are working properly before launch. Other systems will not run tests during pre-launch checks, since those test would cause the pod to accelerate. Table ?? shows the steps that will be taken for the brakes test.

Table 51: Brakes Pre-launch Test

Steps	Part	Action	Desired Response	Reason
1)	BPT-0	N/A	BPT-0 == BPT-1, 100 < BPT-0	Check Tank Pressure and ensure NCV-1 will not vent air to inhibit braking
	BPT-1	N/A	BPT-1 == BPT-0, 100 < BPT-1	
	BPT-4	N/A	PT-5 == 200	
	NCV-1	Close	Closed	
2)	NOV-1	Open	Opened	Open valves to begin braking
	NOV-2	Open	Opened	
3)	BPT-2	N/A	BPT-3 == BPT-4, 100 == BPT-3	Check that pressure value is in correct range for calipers
	BPT-3	N/A	BPT-4 == BPT-3, 100 == BPT-4	
4)	NOV-1	Close	Closed	Close Valves to isolate brakes
	NOV-2	Close	Closed	
5)	NCV-1	Open	Opened	Vent air in calipers to stop braking
6)	NCV-1	Close	Closed	Close valve to reset braking system
7)	BPT-2	BPT-3	BPT-2 == BPT-3, BPT-2 < Min	Check pressure to ensure brakes are not actuated
	BPT-3	BPT-3	BPT-3 == BPT-2, BPT-3 < Min	
8)			Brakes Ready	

After the braking test is performed the new reading for the braking system will be as follows in Table 52:

Table 52: Brake Monitor Checks Post-Test

Monitor	Description	Expected Value	Expected Deviation
BPT-4,BPT-9	Tank Pressure Transducer (After Test)	<200 PSI	
BTC-0,BTC-1	Tank Temperature Sensor (After Test)	TBD	+/- 5%
BPT-0 and BPT-1, BPT-5 and BPT-6	Post-Regulation Pressure Sensors	100 PSI	-5%
BPT-2 and BPT-3, BPT-7 and BPT-8	Caliper Pressure Sensor (After Test)	0.125 PSI	+/- 5%

Ready-To-Remove Checklist

After the pod has come to a complete stop, all three battery packs will remain operational. The Secondary Pack is on until the pod reaches the unloading area. To disconnect power from the pod, the

switches for the primary packs will be flipped and the secondary pack connector must be disconnected.

Once the pod is in the ‘Off’ state then the pod is ready to be removed from the Hyperloop. The ‘Stop’ state has propulsion valves closed, and brakes released, and wheel motors unpowered. Once these states have been confirmed, the pod will be remotely commanded to enter the ‘Off’ state which will power the normally-open valves in braking system and the PLC, but otherwise the pod’s systems do not require power.

9 Comments on Scalability

A “working Hyperloop system” shall be defined as an operational vacuum transport vehicle for greater than 20 passengers with a top speed over 500 mph. The scalability to a working Hyperloop system of each OneLoop subsystem is discussed with respect to system size, cost, mass, and maintenance. The subsystems are organized into categories of “Least Scalable,” “Somewhat Scalable,” and “Most Scalable.”

9.1 Least Scalable

9.1.1 Suspension and Stability

At speeds of over 500 mph, any sort of contact with the subtrack would be problematic. A suspension or stability system with polyurethane or rubber wheels would not be viable at these speeds, since whatever is touching the track would melt, break, or both. This also goes for any type of propulsion system that uses contact with the rail or track to speed up. Similarly severe issues would be encountered with metal wheels; although they may not melt like the polyurethane, they would have much less springiness, resulting in catastrophically large loads at every bump. In the end, our team believes that levitation and contactless propulsion systems are essential to a real hyperloop system, making our suspension and stability systems non-scalable for higher speed systems. This fact precludes the need to discuss potential suspension and stability systems costs, masses, or maintenance needs, since the overall system is completely non-scalable.

9.1.2 Chassis

The chassis system is also not scalable. The OneLoop chassis is designed to optimize space, keep a low center of gravity, and allow for modular mounting. A real system would require an entirely different design in order to account for passengers and the cabin environment while maintaining space for the engineering systems.

Our chassis cost approximately \$400 to manufacture (including materials cost), since an independent TIG welder could do the task efficiently and quickly. A much larger system would most likely require a full team of at least 10 welders and much more material to manufacture over the course of about one week. Assuming those welders charge the same hourly rate as ours, this project would likely have a cost two orders of magnitude above ours, putting the chassis cost in the range of multiple tens of thousands of dollars.

Following the same logic, a much larger, full-scale chassis would also have a mass that is two orders of magnitude higher than ours. If the system is still made of aluminum or even a mix of aluminum composites, this would allow the total mass to be much lighter than that of a train car (typically 20 or more tons), which is essential to achieve levitation as desired.

One benefit of a fixed metal chassis is the low need for maintenance. A structural strength test would most likely need to be concluded on a schedule similar to that for trains or planes, but the chassis should retain its strength as long as no crashes occur.

9.1.3 Power

Similarly, our pod is designed to be very low-power to minimize electrical safety concerns. A more realistic system would require much more power just to accommodate passenger comfort and environment. Furthermore, as previously discussed, levitation would be necessary for a full-scale system, and the only currently viable form of levitation is MagLev, which draws a significant amount of power.

9.2 Somewhat Scalable

9.2.1 Propulsion

The propulsion system is not particularly scalable to full system size. This is mostly due to the inefficiencies of cold gas thrusters inherent to expanding from onboard tanks. As seen in the propulsion section of this report, cold gas systems get very cold over their runtime, reaching the critical temperatures of Nitrogen in as little as 16 seconds. Therefore, in order for a cold gas or tri-gas system to push a much larger pod full of people, all of the necessary thrust would need to come during those first 16 seconds. Furthermore, it is likely that a full-scale system would want to avoid depressurization events as much as possible to minimize system cost. This would most likely be accomplished by sequestering and depressurizing small track segments for loading and unloading of passengers.

With respect to cost, the propulsion system is relatively efficient. Nitrogen is one of the most abundant pressurized gases to acquire, largely due to its predominance in the composition of air. Furthermore, a tri-gas system uses very small amounts of hydrogen and oxygen, keeping the system safe but also lowering the procurement cost of the propellant. Also, as discussed in the catalyst selection portion of the propulsion section, catalysts have been shown to be re-usable if baked in a 500 degree Fahrenheit dry Nitrogen environment for 10 minutes [18]. While this is not particularly useful for our pod, infrastructure to regularly heat treat catalyst beds for reusability would be easy to set up on a large scale, resulting in even more efficiency.

A scaled up propulsion system would not be too massive. In fact, one of the primary reasons our team selected tri-gas over other forms of propulsion is that the lack of power keeps the system lightweight. However, the current technology used in Hyperloop industry is in-track Linear Induction Motors. While their power requirement and therefore mass is extremely large, these LIMs do not contribute to on-pod mass, making them far more ideal than any form of onboard propellant with respect to mass.

System maintenance a tri-gas system would be relatively minimal. Propellant tanks would need to be refilled after each run, and as previously mentioned a regular heat treatment schedule would allow for better catalyst reusability. Other than these considerations, full-scale propulsion maintenance would consist primarily of regular system safety checks to ensure that the performance of valves does not degrade over time.

9.2.2 Braking

Our pod's braking system suffers from similar issues to the stability system, where contact with the I-beam or track results in significant loads that could deteriorate the brake pads. For a full-scale hyperloop system, it is more efficient to use contactless eddy brakes for initial deceleration followed by friction brakes once the pod has slowed down to a more manageable speed.

The cost of pneumatic brakes is low; our system's non-discounted price is approximately \$3500. With higher strength calipers, the performance of our brakes could be scaled up to accommodate deceleration from much higher speeds while maintaining low cost. However, this comes at the expense of long-term performance, due to the deterioration mentioned above. Furthermore, that deterioration would likely necessitate a rigorous maintenance schedule, with brake pads needed replacement after only a few uses.

9.3 Most Scalable

9.3.1 Controls

With respect to system size, the controls system would scale extremely well. Our controls system is extremely safe, with a SIL 2 safety level and a Safety Controller PLC. As this type of controller is typically used to run automated factories, it has the computational capability to monitor and take action on a number of different criteria. Even if the system size were to increase, this controller could handle acceleration, braking, cabin environment, and tube-travel communications, all while keeping emergency procedures on its safety module. Furthermore, other than regular safety checks that the control algorithm is functioning properly, the controls system should require little to no maintenance.

Controls also scales well when considering cost. The full, non-discounted price of our controls system is approximately \$37,000. While a full-scale system would undoubtedly require many more sensors and control valves, the overall cost should be able to stay under \$60,000, which is little compared to the likely total cost of a Hyperloop system.

9.4 Conclusion

While the OneLoop 2019 pod is very cost-effective when investigating scalability, many of the subsystems would not be able to handle the high speed requirements of a real Hyperloop pod. Instead, our team believes a more practical approach is to use an entirely contactless system. Such a system would use magnetic levitation to stay off of the subtrack, in-track linear induction motors for propulsion, and eddy brakes for deceleration to a manageable speed from which friction brakes could take over.

References

- [1] Pressure ratings for tubing and threaded end connections. <https://www.my-ssp-usa.com/resources/pressure-ratings>. Accessed: 2019-1-24.
- [2] Rivet application tables and installation practice per. mil-r-47196.
- [3] Tips tricks for matching fea results to physical data. <https://caeai.com/blog/tips-tricks-matchingfea-results-physical-data>. Accessed: 2019-1-24.
- [4] T. L. Bergman and A. Lavine. *Fundamentals of heat and mass transfer*. John Wiley Sons, Inc., Hoboken, NJ, 2017.
- [5] DF Cox, KL McElhaney, and RH Staunton. Aging and Service Wear of Air-Operated Valves Used in Safety-Related Systems at Nuclear Power Plants. Technical report, Nuclear Regulatory Commission, 1995.
- [6] Vanessa Dorado, Zachary Grunder, Bryce Schaefer, Meagan Sung, and Kevin Pedersen. Nasa Marshall Space Flight Center Tri-gas Thruster Performance Characterization. 2013.
- [7] Oscar Biblarz George P. Sutton. *Rocket Propulsion Elements*. Wiley, 2010.
- [8] A. Golkar. Talaris 1g hopper demonstrator design document. 16.83/89 Class Final Report, Department of Aeronautics and Astronautics, Massachusetts Institute of Technology, Cambridge, MA, 2009 (unpublished; archived in TALARIS SVN file repository).
- [9] Jeffry S. Welsh Gregory E. Sanford, Adam C. Biskner. Failure testing of large composite aerospace structures. Accessed: 2019-1-24.
- [10] Hannu Jaaskelainen. Exhaust system materials. Technical report, DieselNet Technology, 2011.
- [11] McLinden M. O. Lemmon, E. W. and D. G. Friend. *Thermophysical Properties of Fluid Systems, NIST Chemistry WebBook*,. National Institute of Standards and Technology, 2011.
- [12] Sarah Lynn Nothnagel. *Development of a cold gas propulsion system for the talaris hopper*. PhD thesis, Massachusetts Institute of Technology, 2011.
- [13] United States Department of Labour. Comparison of hazard communication requirements osha hazard communication standard 29 cfr 1910.1200(hcs) globally harmonized system(ghs). <https://www.osha.gov/dsg/hazcom/ghoshacomparison.html6>.
- [14] Director of National Intelligence. Bomb threat standoff distances. https://www.dni.gov/files/NCTC/documents/features/documents/2006_calendar_bomb_stand_chart.pdf.
- [15] Paul M. Ordin, William J. Brown, Harold Beeson, Mike Pedley, Dennis Griffin, Coleman J. Bryan, Wayne A. Thomas, and Wayne R. Frazier. Safety Standard For Hydrogen and Hydrogen Systems Guidelines for Hydrogen System Design, Materials Selection, Operation, Storage, and Transportation. 1997.
- [16] Conor D. Johnson Paul S. Wilke and Eugene R. Fosness. Whole-spacecraft passive launch isolation. Technical report, 1998.
- [17] Raul Rojas. Models for dc motors. Technical report, Takustr. 9, 14195 Berlin, Germany.
- [18] M. Ladacki R.W. Roberts, H.L. Burge. Investigation of catalytic ignition of oxygen/hydrogen systems. Technical report, Rocketdyne Research Department, 1965.
- [19] Sunray-inc. Load capacities. <https://www.sunray-inc.com/load-capacities/>.
- [20] B. Zastrau V. Pauk. 2d rolling contact problem involving frictional heating. 2002.
- [21] Jim Yeager. Advanced nsts propulsion system verification study final report. Technical report, Rockwell International, 1989.